

DTIC FILE COPY

AD-A214 602

4

GL-TR-89-0243

**Reactions of Atmospheric Species With Clean
and H, C. and O Implanted Species**

J. W. Rabalais

University of Houston
Department of Chemistry
Houston, TX 77004

27 July 1989

Final Report
1 April 1986-15 July 1989

APPROVED FOR PUBLIC RELEASE; DISTRIBUTION UNLIMITED

GEOPHYSICS LABORATORY
AIR FORCE SYSTEMS COMMAND
UNITED STATES AIR FORCE
HANSCOM AIR FORCE BASE, MASSACHUSETTS 01731-5000

DTIC
ELECTE
NOV 24 1989
S B D
C

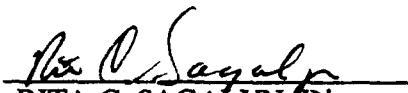
89 11 21 138

"This technical report has been reviewed and is approved for publication"


EDMOND MURAD
Contract Manager


CHARLES P. PIKE, Chief
Spacecraft Interactions Branch

FOR THE COMMANDER


RITA C. SAGALYN, Director
Space Physics Division

This report has been reviewed by the ESD Public Affairs Office (PA) and is releasable to the National Technical Information Service (NTIS)

Qualified requestors may obtain additional copies from the Defense Technical Information Center. All others should apply to the National Technical Information Service.

If your address has changed, or if you wish to be removed from the mailing list, or if the addressee is no longer employed by your organization, please notify AFGL/DAA, Hanscom AFB, MA, 01731. This will assist us in maintaining a current mailing list.

Do not return copies of this report unless contractual obligations or notices on a specific document requires that it be returned.

REPORT DOCUMENTATION PAGE

Form Approved
OMB No. 0704-0188

Public reporting burden for this collection of information is estimated to average 1 hour per response, including the time for reviewing instructions, searching existing data sources, gathering and maintaining the data needed, and completing and reviewing the collection of information. Send comments regarding this burden estimate or any other aspect of this collection of information, including suggestions for reducing this burden, to Washington Headquarters Services, Directorate for Information Operations and Reports, 1215 Jefferson Davis Highway, Suite 1204, Arlington, VA 22202-4302, and to the Office of Management and Budget, Paperwork Reduction Project (0704-0188), Washington, DC 20503

1. AGENCY USE ONLY (Leave blank)		2. REPORT DATE 27 July 1989		3. REPORT TYPE AND DATES COVERED Final (1 April 1986-15 July 1989)	
4. TITLE AND SUBTITLE Reactions of Atmospheric Species With Clean and H, C, and O Implanted Species				5. FUNDING NUMBERS PE: 61102F 2303G2AH	
6. AUTHOR(S) J. W. Rabalais					
7. PERFORMING ORGANIZATION NAME(S) AND ADDRESS(ES) University of Houston Department of Chemistry Houston, TX 77004				8. PERFORMING ORGANIZATION REPORT NUMBER Contract No.: F19628-86-K-0013	
9. SPONSORING/MONITORING AGENCY NAME(S) AND ADDRESS(ES) Geophysics Laboratory Hanscom AFB Massachusetts 01731-5000 Contract Manager: Edmund Kuzel/PHK				10. SPONSORING/MONITORING AGENCY REPORT NUMBER GL-TR-89-0243	
11. SUPPLEMENTARY NOTES					
12a. DISTRIBUTION/AVAILABILITY STATEMENT Approved for public release; distribution unlimited.				12b. DISTRIBUTION CODE	
13. ABSTRACT (Maximum 200 words) The interactions of low energy ions with surfaces have been studied using surface science techniques. The energy range studied is from 1 eV-5 keV, the ions involved are rare gas ions (He ⁺ , Ne ⁺ , Ar ⁺) and reactive ions such as N ₂ ⁺ , N ⁺ , C ⁺ , CO ⁺ , and O ⁺ , and the surfaces included compounds such as K ₂ TiF ₆ , K ₂ NbF ₇ , K ₂ TaF ₇ , and boron nitride (BN) and elemental materials such as graphite, gold, magnesium, nickel, boron, Si(100), and W(211). The phenomena investigated included scattering, recoiling, ion induced surface damage (decomposition, oxidation, nitridation, chemisorption), inelastic collisions with emission of photons and electrons, scattered and recoiled ion fractions, collisional dissociation, and the dynamics of low energy collisions. The results are contained in six scientific publications in refereed journals.					
14. SUBJECT TERMS Ion-surface collisions Scattering Recoiling		Reactive ions Ion induced decomposition Collisional dissociation		15. NUMBER OF PAGES 130	
				16. PRICE CODE	
17. SECURITY CLASSIFICATION OF REPORT UNCLASSIFIED	18. SECURITY CLASSIFICATION OF THIS PAGE UNCLASSIFIED	19. SECURITY CLASSIFICATION OF ABSTRACT UNCLASSIFIED	20. LIMITATION OF ABSTRACT		

I. Summary of Research Results

The research results from this grant are summarized below. The work resulted in six publications in refereed journals. These publications are listed in Sect. II. The work also resulted in six presentations at scientific meetings.

XPS and UPS studies of 4-keV Ar^+ bombarded K_2TiF_6 , K_2NbF_7 , and K_2TaF_7 have revealed the reduction of the central transition-metal atom to lower oxidation states in all cases. The tantalum and niobium in K_2TaF_7 and K_2NbF_7 are reduced to oxidation states of IV, II, and 0, while the titanium in K_2TiF_6 is reduced to oxidation states of III and II. The various oxidation states have been identified through binding energy shifts of the XPS core level spectra. Atomic concentration measurements were used to estimate the surface compositions. These results are discussed in terms of the thermal spike model, and the behavior of the specific compounds is shown to correlate with the relative stability of the possible reaction products.

Scattering of molecular nitrogen ions in the 1.5-4.5 keV range from gold and graphite surfaces has resulted in a small fraction of surviving molecules and molecular ions in addition to atoms and atomic ions resulting from dissociation. The kinetic energy (E_k) distributions of scattered N_2^+ and N^+ ions have been measured directly by means of an electrostatic sector analyzer (ESA) and the velocity distributions of the scattered N_2 and N neutrals plus ions have been measured by time-of-flight (TOF) techniques. Scattered ion fractions were determined from the TOF measurements. The relative E_k distributions of the scattered

For
on
n/
by Codes
and/or
Special

atomic ions indicate that dissociation from excited repulsive electronic states which are populated during the collision dominate the mechanism, rather than purely vibrational or rotational excitation from the $X^2\Sigma_g^+$ ground state of N_2^+ . The excited dissociative $C^2\Sigma_u^+$ and $D^2\Pi_u$ states of N_2^+ are accessible by Franck-Condon transitions from the $X^2\Sigma_g^+$ state. The data are consistent with a mechanism in which these two dissociative states contribute their repulsive energy to the large relative E_k distributions of the scattered N^+ ions. The electronic excitation occurs via electron promotion during the scattering collision through the Fano-Lichten mechanism.

The chemisorption of OCS on polycrystalline Ni foil, in the 77-923 K temperature range, was investigated by XPS, UPS and AES electron spectroscopies. At all temperatures studied, chemisorption was found to be dissociative yielding absorbed S and gas phase CO. The reaction is found to be strongly exothermic with a low activation energy.

Boron nitride formation from bombardment of boron with 0.5-5 keV N_2^+ ions has been studied by in situ XPS and AES measurements. A dynamic process of nitrogen implantation and surface sputtering leads to the formation of a BN layer whose thickness equals the range of the nitrogen ions in the boron. The maximal nitrogen entrapment is determined by the stoichiometry of BN; excess nitrogen is released. No diffusion of nitrogen to the bulk nor expansion of the BN layer is detected at room temperature for prolonged bombardment. The results are in accord with a simple collisional altered layer model that is presented.

The technique of time-of-flight ion scattering and recoiling spectrometry (TOF-SARS) has been developed. TOF-SARS uses a pulsed low keV ion beam and TOF methods for analysis of both scattered and recoiled neutrals and ions simultaneously with continuous scattering angle variation over a flight path of ~ 1 m. The capabilities of the technique are demonstrated by the following examples: (i) TOF spectra versus scattering angle θ for the system Ar^+ on $\text{Si}(100)$; (ii) Comparison of LEED and AES; (iii) Surface and adsorbate structure determination for the systems of clean $\text{W}(211)$ and O_2 and H_2 chemisorbed on $\text{W}(211)$; (iv) Monitoring surface roughness on $\text{W}(211)$; (v) Surface semichanneling along the troughs of the $\text{W}(211)$ surface; (vi) Measurements of scattered ion fractions for Ne^+ on magnesium; and (vii) Ion induced Auger electron emission for Ne^+ on magnesium. A historical prospective of low energy ion scattering has been presented and surface structural determinations for various systems are tabulated.

Studies involving ion-solid interactions in the range of a few eV to a few keV that are intermediate between thermal gas-surface interactions and high energy bulk implantation have been collectively examined. The interactive process has been traced in a phenomenological manner by providing a simple treatment of the different physical and chemical phenomena involved. The kinematics of noble gas ion as well as atomic and molecular reactive ion interactions with surfaces has been treated in terms of classical dynamics and experiments are described that probe the nature of ion-solid interaction potentials by examining the

scattering of ions from surfaces and the charge exchange processes operative during scattering. Molecular ion scattering has been investigated and the behavior interpreted in terms of partial dissociation that results in both atomic and molecular scattering. A neutralization model has been described that considers the interaction domain to be divided into three steps: the incoming trajectory, the close encounter, and the outgoing trajectory. A spectrum of possible results from the interaction process is described; these include reaction and chemical alteration of the target surface, desorption of adsorbate atoms by hyperthermal physical/chemical interaction, and accumulation of a high surface concentration of the projectile species, viz. film deposition. These studies investigate the science basic to a number of technological phenomena and represent an elegant approach to the simulation of a number of these phenomena in the controlled environment of ultra-high vacuum. Qualitative and quantitative arguments are made for a number of the experimental results and cross-examination of data from different laboratories is made in terms of simple kinetic and thermodynamic concepts to illustrate fundamental similarities in the various studies.

II. List of Scientific Publications Resulting From Grant

1. C. S. Sass and J. W. Rabalais, "Ion Beam Induced Decomposition of Transition-Metal Fluoroanions", *J. Phys. Chem.*, 92, 2072 (1988).
2. C. S. Sass and J. W. Rabalais, "Dissociative Scattering of 1.5-4.5 keV N_2^+ and N^+ on Gold and Graphite Surfaces", *J. Chem. Phys.*, 89, 3870 (1988).

3. C. S. Sass and J. W. Rabalais, "Chemisorption of Carbonyl Sulfide (OCS) on Ni Between 77 and 293 K", **Surface Sci.**, 194, L95 (1988).
4. P. Mezentzeff, Y. Lifshitz, and J. W. Rabalais, "BN Formation From Bombardment of Boron With N_2^+ ", **Nucl. Instr. & Meth. in Phys. Res. B**, submitted.
5. O. Grizzi, M. Shi, H. Bu, and J. W. Rabalais, "Time-Of-Flight Scattering and Recoiling Spectrometry (TOF-SARS) for Surface Analysis", Ninth International Summer Institute in Surface Science (ISISS 1989), Aug. 1989, submitted. To be published in **Chemistry and Physics of Solid Surfaces**, Vol. 8.
6. S. R. Kasi, H. Kang, C. S. Sass, and J. W. Rabalais, "Inelastic Processes in Low-Energy Ion-Surface Collisions", **Surface Sci. Rpts.**, 10, 1 (1989).

III. List of Presentations Resulting From Grant

1. "Dissociative Scattering of Diatomic Ions at Surfaces", 42nd Southwest Regional ACS Meeting, Houston, TX, November 1986.
- 2.* "Interactions of Low-Energy Ions With Surfaces", Third International Workshop on Desorption Induced by Electronic Transitions, Shelter Island, NY, May 1987.
- 3.* "Low-Energy Mass-Selected Ion Beams For Film Deposition", Southeastern Regional Meeting of the American Physical Society, Nashville, TN, November 1987.
- 4.* "Exchange of Electronic Energy in Low-Energy Ion Bombardment of Solids", Minnesota Chapter-American Vacuum Society Symposium, Minneapolis, MN, April 1988.
- 5.* "Interactions of Low-Energy Ions With Surfaces", Gordon Conference on Particle/Solid Interactions, Plymouth, NH, July 1988.
- 6.* "Exchange of Electronic Energy in Low-Energy Ion Bombardment of Solids", Amer. Vacuum Society Symposium, Rochester, NY, June 1989.

*Invited Lectures

IV. Personnel Supported

Project Scientist:	J. W. Rabalais
Research Associates:	Oscar Grizzi
	Craig Sass
	H. Kang
Graduate Students	Ming Shi
	S. R. Kasi
	C.-C. Hsu

V. Equipment Purchased

MDC Vacuum Products	-	GV-1500M VHV Stainless Steel 302001 Gate Valve \$803.78
Scientific Instruments	-	MBL-1 Miniblast Sandblaster \$591.33
Varian Vacuum Products	-	Gate Valve \$2,291.79
Micro Science Inc.	-	Electron Gun \$6,685.30
EG & G Ortec	-	MCA Computer Card \$2248.66
Physical Electronics	-	Power Supply \$781.56
Huntington Labs	-	Valve \$644.43
Hipotronics, Inc.	-	Power Supply \$1694.70

surface science reports

Review Journal

**INELASTIC PROCESSES IN LOW-ENERGY ION-SURFACE
COLLISIONS**

S.R. KASI, H. KANG, C.S. SASS and J.W. RABALAIS

Volume 10, Nos. 1/2, 1989

Published January 1989



North-Holland Amsterdam

SSREDI 10(1/2) 1-104 (1989)

SURFACE SCIENCE REPORTS

A review journal

Editors

L. Dobrzynski, *Lyonne d'Ascq*
C.B. Duke, *Riverside, B.C.*
G. Ertl, *Berlin*
I.C. Feldman, *Murray Hill, N.J.*
I. Kay, *San Jose, C.A.*
D.A. King, *Cambridge*
W. Moch, *Pharburg*
O. Nishikawa, *Yokohama*
W.F. Spicer, *Stanford, C.A.*
A. van Oostrom, *General Editor, Linderoed*
W.H. Weinberg, *Pasadena, C.A.*
H.H. Wieder, *La Jolla, C.A.*

VOLUME 10 (1989)

NORTH-HOLLAND — AMSTERDAM

INELASTIC PROCESSES IN LOW-ENERGY ION-SURFACE COLLISIONS

S.R. KASI, H. KANG *, C.S. SASS ** and J.W. RABALAIS

Department of Chemistry, University of Houston, Houston, TX 77204, USA

Manuscript received in final form 13 October 1988

Studies involving ion-solid interactions in the range of a few eV to a few keV that are intermediate between thermal gas-surface interactions and high energy bulk implantation are collectively examined in this review. The interactive process is traced in a phenomenological manner by providing a simple treatment of the different physical and chemical phenomena involved. The kinematics of noble gas ion as well as atomic and molecular reactive ion interactions with surfaces are treated in terms of classical dynamics and experiments are described that probe the nature of ion-solid interaction potentials by examining the scattering of ions from surfaces and the charge exchange processes operative during scattering. Molecular ion scattering is investigated and the behavior interpreted in terms of partial dissociation that results in both atomic and molecular scattering. A neutralization model is described that considers the interaction domain to be divided into three steps: the incoming trajectory, the close encounter, and the outgoing trajectory. A spectrum of possible results from the interaction process is described; these include reaction and chemical alteration of the target surface, desorption of adsorbate atoms by hyperthermal physical/chemical interaction, and accumulation of a high surface concentration of the projectile species, viz. film deposition. These studies investigate the science basic to a number of technological phenomena and represent an elegant approach to the simulation of a number of these phenomena in the controlled environment of ultra-high vacuum. Qualitative and quantitative arguments are made for a number of the experimental results and cross-examination of data from different laboratories is made in terms of simple kinetic and thermodynamic concepts to illustrate fundamental similarities in the various studies.

* Present address: Department of Chemistry, Pohang Institute of Science and Technology, Pohang, 680 Korea

** Present address: Eastman-Kodak Co., Kingsport, Tennessee, USA

Contents

List of symbols	4
1 Introduction	6
2 General low energy reactive ion beam-surface interactions	7
2.1 Role of kinetic energy	7
2.2 Sequence of events in reactive ion-surface encounters	8
2.3 Elastic and inelastic collisions	9
2.4 Physical versus chemical sputtering	10
2.5 Dynamical aspects of the collisions	12
2.5.1 Neutralization distance	12
2.5.2 Time scale for neutralization	12
2.5.3 Surface response time	13
2.5.4 Energy level shifts and broadening	13
3 Experimental methods	15
4 Kinematics and dynamics of ion-surface collisions	19
4.1 Binary collision model	19
4.1.1 Quasi-single scattering (SS)	20
4.1.2 Quasi-multiple scattering (MS)	20
4.2 Extension to low energy reactive ions	21
4.3 Scattering of polyvalent ions	27
4.3.1 General features of diatomic scattering in the keV range	28
4.3.2 Classical effects	29
4.3.3 Electronic effects	30
4.3.4 Extension to large molecules	35
5 Charge transfer process in ion-surface collisions	35
5.1 Experimental considerations	36
5.2 Model for scattered ion fractions (Y_s)	37
5.2.1 Incoming and outgoing trajectories	38
5.2.2 The close encounter	38
5.2.3 Final Y_s expressions	38
5.2.4 Transition probabilities	40
5.3 Extension of model to directly recorded (DR) ion fractions	43
5.4 Examples of DR and scattered ion fractions	47
5.5 Applications of the models of scattered and DR ion fractions	47
5.5.1 Scattered ion fractions	47
5.5.2 Positive DR ion fractions	50
5.5.3 Negative DR ion fractions	50
5.5.4 General trends in DR ion fractions	51
5.6 Effects of chemical environment on DR ion fractions	52
5.6.1 Influence of H on O and C DR ion fractions	52
5.7 Scattered alkali ion fractions	53
5.8 Charge exchange in low energy atomic and molecular ions	56
6 Reactions of energetic ions with clean surfaces	57
6.1 Atomic ion beam interactions with surfaces	57
6.1.1 Reactions of low energy C^+ , N^+ , O^+ , and F^+ ions	57
6.1.2 Reactions of low energy alkali atoms	59
6.1.3 Factors affecting reaction probabilities	61

6.2. Molecular ion beam interactions with surfaces	62
6.2.1. Reactions of low energy homonuclear diatomic ions	63
6.2.2. Chemical effects in low energy ion beam studies	65
6.2.3. Low energy molecular ion reaction dynamics	67
7. Beam-surface reaction kinetics	68
7.1. Kinetics model	68
7.2. Reaction of N_2^+ and N^+ with molybdenum	71
7.3. Application of kinetics model to N_2^+ and N^+ reactions with Mo	75
8. Desorption induced by energetic particle bombardment	73
8.1. Physical sputtering effects in ion-surface interactions	73
8.2. Electronic effects and model calculations	77
8.3. Chemical sputtering effects in reactive ion-surface interactions	79
8.3.1. Atomic ion induced desorption	79
8.3.2. Molecular ion induced desorption	83
8.3.3. Ion-assisted desorption in a reactive gas environment	83
8.4. Mechanisms for energetic reactive particle induced desorption	84
9. Thin film deposition by low energy reactive ion bombardment	89
9.1. Homonucleation studies by mass-selected ion beam deposition (MSIBD)	89
9.2. Heteronucleation studies by MSIBD	90
9.3. Ion-assisted deposition (IAD) of thin films	95
9.4. Theoretical formulation of energetic particle deposition	96
10. Perspective	98
Acknowledgments	99
References	99

List of symbols

A	Pre-exponential constant
a	Factor determining ion-surface interaction range
$ a\rangle$	Discrete atomic level
$d\sigma, d\Omega$	Differential scattering cross section
E	Projectile kinetic energy
E_b	Bond energy in a diatomic molecule
E^b	Bulk binding energy
E_B	Bottom of surface valence band
E_c	Conduction band limit
E^d	Bulk displacement energy
E^f	Energy limit for particle trapping in a solid
E_f	Fermi level
E_{rel}	Relative kinetic energy of atoms after scattering of a diatomic molecule
E_s	Scattering energy
E^s	Surface binding energy
E_t	Top of surface valence band
E_v^s	Lowest vacant energy level of an ion
E_z	Perpendicular energy component
e	Electron charge
F_c	Source filament
$f(s)$	Mixing function
IP	Ionization potential
J_i	Ion flux
J_v	Vapor flux
k	Spectrometer constant
k^{-1}	Parameter reflecting finite screening length of metal
$ k\rangle$	Metal states
M	Projectile mass
m	Ion charge state
N	Neutral scattered particle flux
N^m	Number of scattered particles in charge state m
N_{max}	Maximum number of surface sites per unit area available for reaction
N_i^s	Incident singly charged particle flux
N_r	Extent of reaction
$N(t)$	Surface concentration of reacted beam atoms
n	Surface atom density
$n(s)$	Equilibrium occupation of alkali valence level
P_r	Reaction probability
P_s	Scattering probability

P_{st}	Sticking probability
P_{1s}, P_{1p}, P_{1d}	Probability factors associated with neutralization model
P_{1s}, P^m, P_{OR}	
P_{CI}, P_s	
Q	Coulombic charge
$R(s)$	Electron transition rate
S	Target surface with x electrons in its valence band
s	Instantaneous atom-surface separation
s_a	Distance for attractive interactions
s_0	Distance of closest approach
s_r	Distance for repulsive interactions
s^*	Freezing distance
s_{MBZ}	Distance of closest approach using MBZ potential
s_{BZ}	Distance of closest approach using BZ potential
t_i	Time for ion to travel from s to surface
t_n	Electron tunneling time
t_r	Surface response time
t_{sn}	Time period between neutralization steps
V	Valence electron-ion core interaction
V_M	Morse potential
V_{BZ}	Biersack-Ziegler potential
V_{MBZ}	Compound Morse-Biersack-Ziegler potential
v_B	Bohr velocity
v_F	Fermi velocity
v_c	Characteristic velocity
v_i	Incoming velocity perpendicular to the surface
v_o	Outgoing velocity perpendicular to the surface
w_F	Work function
x	Number of electrons in target surface valence band
Y_s	Differential ion fraction
z	Atomic number
α	Angle of incidence
β	Rapidity parameter
Δ	Level width
$\Delta\Omega$	Detector acceptance solid angle
ΔE	Energy level shift
Φ	Active ion flux
ϕ	Recoil angle
$\Gamma(s)$	Lorentzian width of broadened alkali valence band
η	Atomic density
θ	Scattering angle
$\rho(E)$	Valence band density of states
σ	Scattering cross section

σ_c	Reaction capture cross section
σ_d	Desorption cross section
τ	Ion neutralization parameter
ω	Surface plasmon frequency

1. Introduction

The interactions of low energy reactive ions with surfaces is a fascinating subject because of the potential of the techniques and the range of phenomena involved. The terms *low energy* and *reactive ions* are used herein to denote ions with kinetic energies (E) in the broad range of one up to several thousand electron volts which are capable of reacting with the target surface atoms to form chemical compounds. In this E range many of the collisions are *inelastic*, that is, ion translational E is converted into electronic excitation and ionization energy and vibrational and rotational motions. When the ion translational E can be channeled into the reaction coordinate of reactions with substantial activation barriers, such barriers can be surmounted at low temperatures. The selectivity and specificity of these beam-surface reactions is high since it is possible to use mass selected ions with well defined E . The reactive ions can be introduced at precise spatial locations in controlled concentrations. These capabilities afford the advantage of altering the chemical nature of the outermost surface layer(s) in localized regions without disturbing the underlying or surrounding crystal structure.

This review treats the fundamental interactions of low energy reactive ions with surfaces. These interactions include electronic processes (ion-surface charge exchange transitions, excited state formation, and photon and electron emission), molecular dynamics (kinematics and collisional dissociation), chemical reactions (kinetic and thermodynamic parameters), and beam particle deposition induced by the collisions. This is an extremely broad range of phenomena to cover. Investigations of these phenomena represent currently active areas of research; as a result, new data, interpretations, models and calculations are constantly emerging. The review selectively focuses on elucidation of the elementary steps describing the electronic, kinematic, thermodynamic, and kinetic aspects of low energy reactive ion-surface interactions with the ultimate goal that such an understanding will allow control of the interactions so that they can be used for specific chemical modifications of surface properties. It is also hoped that this review will kindle interest in the unique panorama of chemical reactions that can be induced by this method. In such an undertaking, it is inevitable that some works will be overlooked; we do not claim to be comprehensive, but only to present our best assessment of the current state of the field. Excellent reviews on beam-surface interactions are already available for the very low energy (below ~ 1 eV) [1-3] and high energy (above a few hundred eV) [4-9] regions.

2. General low energy reactive ion beam-surface interactions

2.1. Role of kinetic energy

The interactions of gaseous ions and neutrals with surfaces are strongly influenced by their kinetic energies E . This E plays a major role in determining whether the impinging particle will scatter from the surface or remained trapped in a potential well at the surface. The probability that a particle becomes trapped and remains on or within the surface is called the *sticking probability* (P_s). The probability that the particle is reflected from the surface is called the *scattering probability* (P_r). Obviously, $P_s + P_r = 1$. The P_s spans many different kinds of trapping mechanisms, such as van der Waals attractions, physisorption, chemisorption, chemical reactions, and implantation.

Fig. 1 shows a generalized diagram of P_s versus E for projectile ions that are lighter than the target atoms. The curve does not correspond to any specific system; it simply illustrates the behavior of P_s as E changes over some ten orders of magnitude. In order to quantitatively represent any specific system, the curve would have to be adjusted both horizontally and vertically to represent the behavior. Beginning at very low E , gaseous species are simply condensed or frozen out on surfaces due to van der Waals attractive potentials which are deeper than the thermal energy kT , where k is the Boltzmann constant. P_s is near unity in this region. As E increases towards ambient conditions ($kT \approx 0.025$ eV near ambient temperatures), P_s begins to decrease. This decrease is due to the necessity for dissipating excess E before the gaseous species can be trapped in a product potential well at the surface. This is the physisorption and chemisorption region. Physisorption occurs when the only attractions between the particle and surface are weak van der Waals forces which provide potential wells that are comparable to the magnitude of

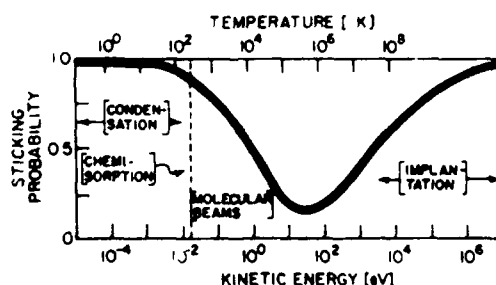


Fig. 1. Generalized plot of particle sticking probability versus particle kinetic energy. The temperatures corresponding to the kinetic energies are shown at the top of the plot. The dashed line represents room temperature

kT . Chemisorption occurs when chemical bonds are formed between the particle and surface atoms; these bond energies are typically larger than kT and in the range 1–10 eV. Hyperthermal molecular beams extend the E range up to several electron volts; this region also exhibits a decreasing P_{st} with E due to the excess E that must be dissipated for sticking to occur. Moving to the very high E region, P_{st} increases with E above $\sim 10^3$ eV because of the ability to force the projectiles into the lattice and implant them below the surface where they are trapped as implanted material. The implantation process becomes very efficient for $E > 10^6$ eV and P_{st} approaches unity. The P_{st} curve goes through a minimum in the intermediate region between one and several hundred electron volts.

This intermediate region is a particularly interesting area where little work has been done. The reason is that this region is not accessible from molecular beam methods which use nozzle expansions. Ion beams must be used to access this region because the ions can be accelerated to any desired energy. However, because it is difficult to transport and focus low E ($< \sim 500$ eV) ion beams, most of the ion beam studies have been conducted at higher energies. The attractive feature of the low E region is that it is in the range of chemical bond energies and activation barriers for chemical reactions. Hence the translational E of the beam particles can be employed for surmounting reaction barriers in order to induce surface chemical reactions that do not occur under ambient conditions, while at the same time avoiding surface lattice damage induced by the more energetic ions, e.g. sputtering. Since the temperature equivalent to a kinetic E of 1 eV is about 1.2×10^4 K, it follows that ion-enhanced reactions and deposition offer access to a region of nonequilibrium processes far beyond the capabilities of thermal reactions. The chemical nature of the adspecies as well as its precise concentration can be controlled by tuning the primary beam E and by using specific doses. Molecular ions can be deposited without dissociation at sufficiently low E . In this energy range the cross sections for "chemical reactions" are much larger than those for "physical processes" such as sputtering or surface modifications induced by momentum transfer processes.

2.2. Sequence of events in reactive ion-surface encounters

In order to treat the reactive ion-surface interaction, it is useful to list specific elementary steps which may be important to the total interaction, although such isolation of individual steps is necessarily artificial. Consider the following events in the approach and collision of an active ion with a surface. (1) Electronic charge exchange transitions between the ion and surface can occur during the approach (or departure) while the pair are separated by several ångströms. Such processes occur by resonant and Auger electron transitions and can produce both ground and excited state neutral projectiles.

- (2) Electronic transitions and electron promotions can occur in the close atomic encounter where the atomic orbitals (AO's) of the colliding atoms merge into molecular orbitals (MO's) of a quasi-diatomic molecule. Such electron promotions can result in neutralization or ionization of the projectile as well as production of highly excited autoionizing and metastable states.
- (3) Dissociation of impinging molecular ions can occur as a result of the charge exchange process or the collision with target atoms.
- (4) The impinging molecules or fragments can be scattered in their original or altered charge state, as daughter fragments of the original molecule, or as some combination with surface atoms.
- (5) Atoms or clusters from the surface itself can be directly recoiled, surface recoiled, or sputtered as a result of charge and/or momentum exchange in the collision.
- (6) The impinging particles can be captured by a potential well at or below the surface where they react to form a compound or remain as implanted species. If the capture probability is higher than the self-sputtering probability, there is net deposition of the particles on the surface and for a sufficient particle fluence a thin film is formed.
- (7) Diffusion of the captured particles, rearrangement of the surface atoms, and selective or preferential sputtering can occur, resulting in alteration of the film stoichiometry expected from the penetration profile alone.
- (8) The electronic excitation induced by the collision can result in emission of both electrons and electromagnetic radiation from the projectile, ejected surface particles, or from the solid surface itself.

2.3. Elastic and inelastic collisions

Elastic collisions are those collisions in which kinetic energy is conserved, i.e. there is no interconversion of kinetic and potential energy. *Inelastic collisions* are those collisions in which ion kinetic energy is converted into potential energy such as electronic excitation, ionization, and formation of new chemical species. Reactions of active ions leading to formation of new chemical species are necessarily inelastic. Since such active ion-surface interactions involve a combination of some or all of the events listed in section 2.2, comprehensive understanding of the processes is best obtained by designing experiments and developing models which elucidate details of these individual events. Experiments of this nature have been designed by various research groups. Some of the most pertinent experiments for revealing information about these inelastic processes are as follows: (i) observations of displacements in the scattering energy from the elastic scattering position [10-13], (ii) detection of electrons emitted during the collision [14-18], (iii) detection of photons emitted during the collision [19-23], (iv) measurements of the types and abundance of specific charge states of scattered, recoiled, and sputtered

species [24–26], (v) measurements of molecular ion excitation and survival probabilities during collision [27–31], (vi) studies of the kinetics and type of compounds formed during active ion surface reactions [32–34], and (vii) measurements of rotational and vibrational excitation and fragmentation patterns of scattered molecules [35–37]. Many studies [38–40] of inelastic processes have been carried out on gas-phase collisions where the number of inelastic channels is limited and tractable. In ion-surface collisions there exists a multitude of inelastic channels; the question of which of these channels is operative and dominant for specific ion-surface collisions is an arduous problem which constitutes the main theme of this article.

2.4. Physical versus chemical sputtering

Sputtering has been defined by Sigmund (ref. [5], chapter 2) as “the erosion at the surface of a solid as a result of energetic particle bombardment that is observable in the limit of small particle currents and fluences”. Roth (ref. [6], chapter 3) has refined this definition and expounded on the aspects of chemical sputtering. In *physical sputtering*, the sputtered particles receive sufficient energy by atomic collisions from the incident particle, as well as secondary particles that are set into motion, in order for them to overcome the surface binding energy. The mechanism of ejection involves collision cascades and/or local energy spikes within the solid. In *chemical sputtering*, chemical reactions between the incident particles and surface atoms produce molecules which have binding energies to the surface that are low enough for them to desorb at the temperature of the substrate. Recombination of projectile and surface atoms to form molecules is often an exothermic process, depositing excess internal energy in the molecular product. In some cases this excess energy can be sufficient to desorb products from the surface, providing the driving force for chemical sputtering or desorption. The terminology *reactive ion induced desorption* rather than chemical sputtering is more appropriate for the low energy ions considered herein because they remove adsorbates from only the outer atomic layer, while sputtering implies erosion of many layers of a material. When the sputtering process or sputtering yield is altered by binding energy changes as a result of implantation of the projectiles, but the dominant ejection mechanism remains that of momentum transfer, the process is called *chemically enhanced or chemically reduced physical sputtering*.

The distinction between chemical and physical sputtering is sometimes not clear. When compound surface layers are formed during bombardment, compounds, clusters, and fragments of these clusters are often observed in the sputtered particles. Whether the ejection is caused by direct momentum transfer from collisions or by the combination of the heat of formation of the compound and the surface temperature which lead to thermal desorption, is not always known. Physical and chemical sputtering can be differentiated by

comparing the sputtering yields obtained from reactive ions with those obtained from rare-gas ions of similar mass. Also, if the primary energy is below the physical sputtering threshold, all ejection must stem from a chemical mechanism. Examples of this are given in section 8.

The dependence of the different sputtering and erosion processes on the primary energy E and the surface temperature T are shown schematically in fig. 2. The divisions between parameter ranges are not sharp. They are determined by the binding energy of surface atoms and molecules formed in chemical reactions. Surface species are ejected if they receive energy either from the bombarding ion or from chemical recombination and thermal energy. In the former case, the threshold energy for physical sputtering has been estimated to be about four times the surface binding energy [41]. In the latter case, a temperature equivalent to about $1/3$ of the binding energy leads to

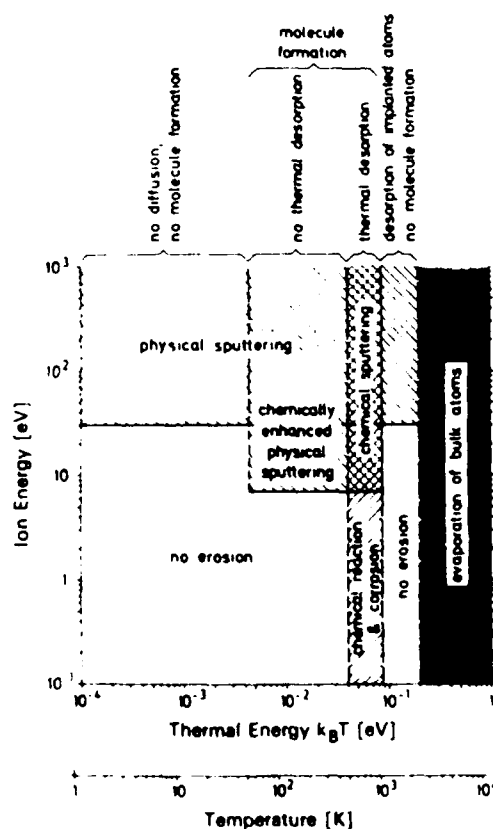


Fig. 2. Ion energy-surface temperature manifold effects in various sputtering phenomena. From ref. [6], with permission.

measurable molecular desorption or bulk atom evaporation. Fig. 2 is specific for the case of hydrogen ions sputtering a carbon surface. Hydrogen bombardment results in the formation of hydrocarbons (methane) which have low surface binding energies. This results in a lowering of the threshold energies, i.e. chemically enhanced physical sputtering. At sufficiently high temperatures it leads to direct chemical sputtering. On the other hand, when oxygen ions are used to sputter aluminium, there is chemically reduced physical sputtering because the aluminum oxide has a higher surface binding energy and is more resistant to sputtering.

2.5. Dynamical aspects of the collisions

Since there is no rigorous theory to deal with this subject, it is informative to consider the dynamical aspects of the collisions in the simplest terms. Here we give simple approximations to the distance and time scales for the interactions as well as the changes in energy level positions and widths in a manner similar to that proposed by Apell [42].

2.5.1. Neutralization distance

Neutralization of slow ions with deep potential wells occurs while the ion is some distance s from the metal surface. An estimate for this distance when an electron tunnels over to the ion can be obtained by equating the work function w_1 of the surface to the energy of the hole in the approaching ion. Electrons with energy ew_1 below the vacuum level, i.e. at the Fermi level, have the smallest barrier to penetrate. The result is

$$s = Qe/w_1, \quad (1)$$

where Qe is the ion charge. This simple expression does not include the image potential shift which will further reduce the tunneling barrier nor the broadening of the ionic energy levels due to interaction with the metal. A conservative estimate using a metallic work function of 5 eV is $s = 2.7Q$ [Å]. This distance is greater than typical atomic sizes and interatomic separations in solids. Such neutralization transitions therefore occur before the close encounter between the projectile and a surface atom.

2.5.2. Time scale for neutralization

The neutralization time can be estimated as the time t_n required for an electron with Fermi velocity v_1 to travel from the surface to the ion while the ion is at s as:

$$t_n = s/v_1 = Qe/w_1 v_1 \quad (2)$$

The electronic transition period is thus $t_e \approx 2 \times 10^{-17} Q$ [s]. For a multiply charged ion, we consider that neutralization takes place in a stepwise manner.

When the ion reaches s for a particular Q , the potential changes to be proportional to $(Q - 1)$ and s decreases accordingly. The time t_{sn} required for the ion with velocity v_0 to travel between successive neutralizations is:

$$t_{sn} = [s(Q) - s(Q - 1)] / v_0 = e / t_0 \omega_1. \quad (3)$$

For multiply charged ions, the filling process can be described by a dimensionless parameter τ as:

$$\tau = t_{sn} / t_0 = v_1 / Qv_0 = (Q_0 E_1 / QE)^{1/2}. \quad (4)$$

Writing the ion mass as $M = QQ_0 m$ defines the parameter Q_0 introduced in eq. (4) ($Q_0 \approx 3700$). For $\tau > 1$, the ion is moving so slowly that we expect neutralization to take place instantly, i.e. slow multiply charged ions are filled by an avalanche of electrons. For $\tau \approx 1$, neutralization takes place in a stepwise fashion electron by electron. For very fast ions there is insufficient time for complete neutralization.

2.5.3. Surface response time

The time scale of the electronic response in the solid is important to the form and strength of the interaction potential. This response time t_r of the solid is of the order of the inverse surface plasmon frequency ω , i.e.

$$t_r \approx 1 / \omega. \quad (5)$$

This must be compared to the time t_s it takes for the ion to travel to the surface from the position s for neutralization:

$$t_s = s / v_0. \quad (6)$$

For a singly charged ion, assuming that $s \approx 2.7$ Å, the time t_s required for an ion of 10–1000 eV to travel from s to the surface and back out to s is of the order of 10^{-13} to 10^{-14} s. This defines a rapidity parameter β as:

$$\beta = t / t_r \approx Qe\omega / \omega_1 v_0. \quad (7)$$

Since ω is of the order of ω_1 , $\beta \approx Qv_B / v_0$, where v_B is the Bohr velocity e^2 / \hbar . Since v_B is of the order of v_1 , β is of the same order as τ for singly charged ions and a factor Q^2 larger than τ for ions with $Q > 1$.

2.5.4. Energy level shifts and broadening

When an ion approaches a surface, its energy levels may shift and broaden due to interactions with the electron bands in the solid. This interaction can be composed of at least three components, i.e. van der Waals attractions, overlap of electronic wave functions, and a Coulombic image force of attraction. Hagstrum [43] has shown that the polarizability of the ion is so small that the van der Waals forces are negligible for the range of ion energies of interest here. The overlap of electronic wave functions results in two effects, an

attraction due to electron exchange resulting in the formation of covalent chemical bonds and a repulsion due to interpenetration of electron clouds and the Pauli exclusion principle. These effects are observed as the formation of bonding and antibonding MO combinations and MO promotion as the AO's of the colliding atoms overlap. Such effects are discussed in more detail in section 5. The Coulombic image force of attraction [44,45] is due to the image potential induced in the metal surface electrons by the approaching ions. To first order the level shift ΔE is determined by the classical image potential

$$\Delta E = -e^2 / [4(\nu + k^{-1})], \quad (8)$$

where ν the atom-surface distance. The parameter k^{-1} takes into account the finite screening length of the metal and determines the shift of the classical image plane with respect to the surface. The levels are broadened by overlap of the atomic and metallic wave functions, making possible resonant electron tunneling through the potential barrier between the atom and the metal. The probability for a resonant transition of a metal electron to an unoccupied level of the ion is determined roughly by the lifetime of the electron near the ion core. This finite lifetime relates via Heisenberg's uncertainty relation to the level width Δ . To first order, this level width is given by Fermi's golden rule

$$\Delta = 2\pi \sum \rho(\epsilon) |U + k^{-1}|^2, \quad (9)$$

where the sum is over all metal states ϵ, k that are degenerate with the atomic level. $\rho(\epsilon)$ is the density of metal states within the valence band. U represents the unperturbed interaction of the valence electron with the ion core. The level width is approximately an exponentially decaying function of the atom-surface distance ν .

Energy levels can be drawn that represent the potential energy of the total system, i.e. ion + surface or neutral + surface, for a rare-gas-like atom that does not form a chemical bond. As the ion approaches the surface, the image force lowers the level of the initial state below the infinite separation level. At short distances, the repulsion between the ion and the surface causes the potential curves to rise sharply in a manner similar to those describing the collision of two atoms. As a neutral atom approaches a surface, the main variation of energy levels with distance is due to the small van der Waals attractions until a distance equivalent to approximately the sum of the atomic radii of the projectile and target atom is reached. At this point, there is an onset of repulsive interactions between collision partners and the potential energy rises rapidly. Since ionic radii are smaller than atomic radii, the distance at which the ionic potential rises due to the repulsion is shorter than that of the atomic potential. Hence, crossings between the ionic ground state and excited states of the neutral can occur as ν decreases and these curves will not tend to cross again in the repulsive region. Franck-Condon transitions can occur at the crossing point of these curves along the incoming trajectory.

resulting in neutralization; reionization can also occur at the crossing along the outgoing trajectory.

3. Experimental methods

An ideal experiment involving the use of low energy reactive ion beams to study projectile-surface reactions and collision dynamics includes the following features: the beam is mass-selected, has a narrow energy spread, and is tunable over a large range (1–1000 eV). Both ions and substrate targets can be chosen from a broad range of materials. The internal state distribution of the reactants in the beam is well-defined. The beam-surface reaction is initiated and allowed to progress in UHV conditions, in order to minimize any role of background gases in the reaction. The reaction products, both on the surface and in the gas phase, as well as their internal states can be monitored by several techniques.

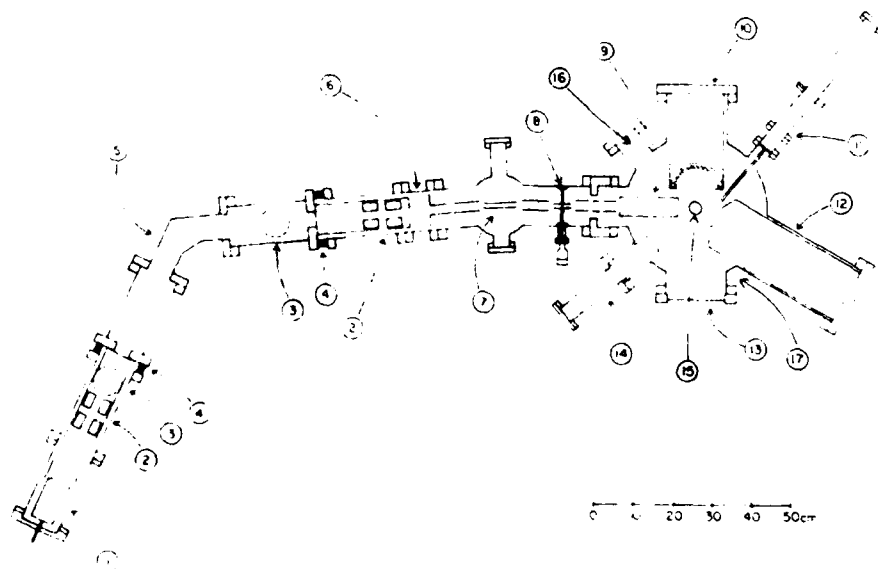


Fig. 3. Schematic drawing of a low energy ion beam assembly and UHV analysis chamber - top view. The components include: (1) ion source and gas inlet, (2) electrostatic quadrupole doublets, (3) vacuum pumping port, (4) ceramic isolator for flight tube, (5) 60° sector electromagnet, (6) gate valve, (7) 6° deflector plates (to eliminate fast neutrals) and turbomolecular pumping stage, (8) rotatable flap serving as a differential pumping baffle and beam aperture, (9) decelerator lens, (10) LEED/AES hemispherical grid analyzer, (11) He I/He II UPS source, (12) CMA analyzer, (13) viewport, (14) RGA mass spectrometer, (15) sample holder, (16) pulsing plate connections, and (17) variable gas admission scheme.

Generation of low energy (1–1000 eV) reactive ion beams is one of the most important aspects of the experiment: this requires the techniques of ion optics established in mass spectrometry. An example of the low energy ion beam line and UHV spectrometer system [46–50] currently operated in the present authors' laboratory is shown in fig. 3. Ions are generated inside a Colutron source by electron impact discharge of introduced gases. Since it is difficult to transport low energy ions over long distances, they are accelerated to several keV after being extracted from the source. The beam transfer optics are floated at the negative potential of the acceleration energy. A 60° electromagnetic sector is used for mass selection in the beam line. Fast neutral species emanating from the mass analyzer are eliminated by a 6° beam deflector. The ions are decelerated to the desired energy just prior to impact with the target. The source ionization region is maintained at 1–500 eV above the grounded target, thus defining the collision energy.

When reactive gases are used for generating the beam, the source region, beam line, and scattering chamber must be efficiently differentially pumped. This allows the reactions to be carried out under ultra-high vacuum conditions, thus minimizing surface contamination and maximizing the detectability of small amounts of surface products as well as desorbed species in real time. In the system shown in fig. 3, four stages of differential pumping by oil diffusion and turbomolecular pumps are used to reduce the gas pressure from a few Torr in the source region down to the 10^{-10} Torr range in the main chamber during ion exposure.

The collision chamber has facilities for cleaning (sputtering and heat annealing) the sample and in situ analytical techniques for characterization of the target surface as well as the scattered and desorbed species. It contains a cylindrical mirror analyzer (CMA) with X-ray and UV source for photoelectron spectroscopy (XPS and UPS) and an electron gun for Auger electron spectroscopy (AES), a 180° hemispherical retarding grid for low energy electron diffraction (LEED), and a quadrupole mass spectrometer for residual gas analysis (RGA). In order to perform time-of-flight ion scattering measurements, a mass spectrometer/TOF drift tube is placed in the position of the LEED optics and a pulsed ion source is placed at the position of the RGA.

The system described above was constructed from a conventional UHV chamber in order to meet the requirements for use with reactive ion beams and surface spectroscopic techniques for product analysis. If nonreactive gases are to be used for generating the beam and the interaction of these gases with the target surface and other components can be ignored, the system design can be simplified in several ways. An example is the system designed by Winters [51,52] in fig. 4 for the use of rare-gas ions in low energy sputtering experiments. Ions are generated in region V by electron impact ionization of rare gases. Electrons are accelerated from the source filament F_e into this region and collected at electrode E. The ions are provided with specific energies when

they are accelerated through the biased grids H toward the target filaments F_{1-3} . Tungsten filaments are used as targets and the amount of gas adsorbed on and/or sputtered from these filament surfaces is determined by flash desorption/mass spectrometric detection.

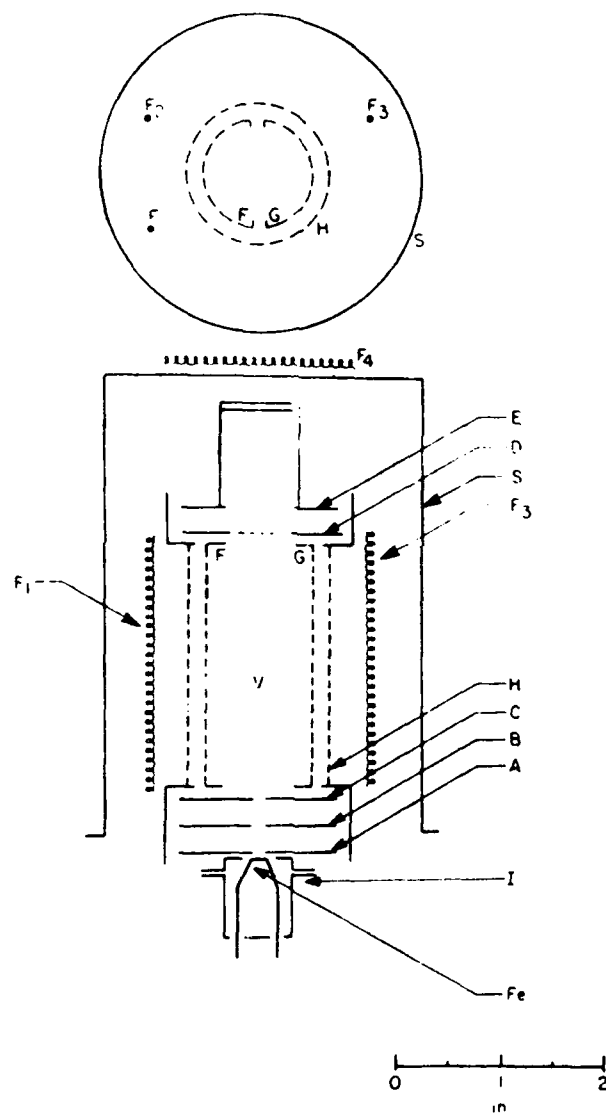


Fig. 4. Simplified set-up for low energy ion/surface studies. F_1 and F_2 are the surfaces studies. With permission from ref. [51].

Scattering experiments can be performed by pulsing the low E beam and using time-of-flight (TOF) and mass spectrometric detection methods. The pulsing and TOF detection scheme [49] are shown in fig. 5. The slow ion beam can be pulsed by using square wave potentials of opposite polarity on a set of parallel electrostatic plates. By adjusting the delay of these square waves, a window of less than $1\ \mu\text{s}$ can be generated in which the sweep voltage goes to zero, thereby gating the ion beam and generating an ion pulse. The scattered particles travel through a quadrupole mass spectrometer that serves as a flight tube (when all elements are grounded) or a mass analyzer for ions. Standard

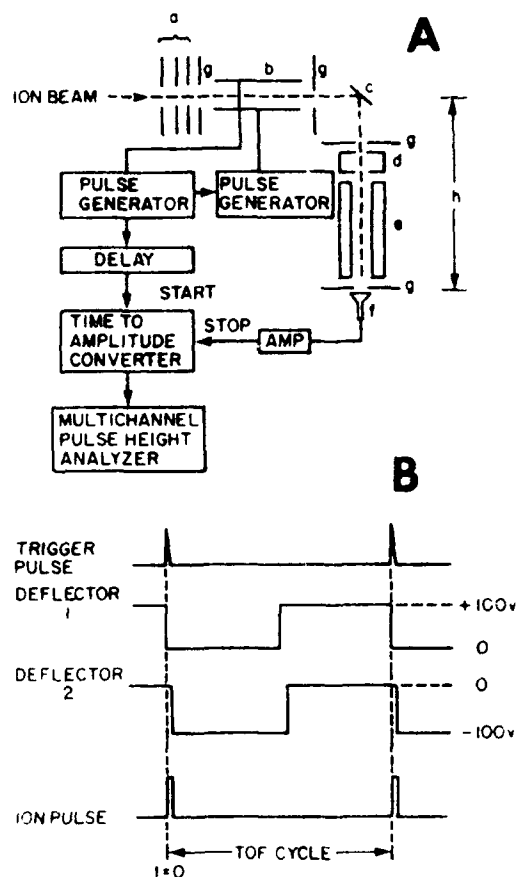


Fig. 5. (A) Schematic diagram of the pulsing and time-of-flight (TOF) detection scheme for 0–300 eV ions: (a) ion beam deceleration lens, (b) deflection plates, (c) sample, (d) ionizer, (e) quadrupole rods, (f) channel electron multiplier, (g) grounded aperture, and (h) flight path. Components (d) and (e) are grounded for TOF scattering. (B) pulsing sequence used to generate a low energy pulsed ion beam. With permission from ref. [49].

[25,53] TOF detection electronics and a channel electron multiplier (CEM) are used for detection. The CEM detects both neutrals and ions, although the detection efficiency [53-55] for neutrals is poor at low energies. This ultimately determines the lowest E at which scattered neutrals can be detected without post-ionization.

Lasers or electron beams must be used for post-ionization of very low E scattered, desorbed, or sputtered neutrals. In order to increase the sensitivity of the mass spectrometer, the quadrupole should be directed towards the sample and as close as possible. The primary beam can be pulsed or chopped and a lock-in amplifier used to process the mass spectrometer signals [56]. The amplitude and the phase shift of the modulated signal allows the determination of reaction probability as well as reaction time constants for the selected reaction products. The technique of matrix isolation has been used successfully [57,58] for analyzing sputtered and desorbed species. In this technique, a cryobaffle partially surrounds the sample and ejected species are condensed on these surfaces. If the surfaces are made of a transparent material, spectroscopic measurements such as absorbance versus frequency can be made through viewports. Los and co-workers [59-61] have studied trapping probabilities of hyperthermal alkali atom beams (0.5-30 eV) on surfaces. The beam is produced by sputtering an alkali target with fast argon ions and energy selection is performed by means of a mechanical slotted disc selector. A cross correlation technique is used to determine the time response of the surface during bombardment by the alkali atoms. The peak in this function corresponds to the fraction of projectiles which have been reflected by the surface and the exponential decay defines the mean residence time of the projectiles which are initially trapped by the surface but will desorb after some adsorption time. In earlier experiments, Lemmon and co-workers [62,63] used radioactive $^{14}\text{C}^+$ beams in the range 5 to 100 eV to react with hydrocarbons that were frozen at -196°C on a cold probe. The products were analyzed by gas-liquid partition chromatography on an instrument that recorded both mass (thermal conductivity cells) and radioactivity (proportional counter) detection.

4. Kinematics and dynamics of ion-surface collisions

4.1. Binary collision model

For ion energies in the keV range, the binary elastic collision model provides a good description of ion/surface collision kinematics and the laws of conservation of energy and momentum can be used to describe scattered trajectories and energies [64]. Classical collision theory treats the scattered particles as rigid spheres, where the repulsive potential between the colliding

pair is zero before contact and infinity when the distance of closest approach reaches the sum of the radii of the two spheres; there is no attractive potential in this model. A detailed treatment of classical dynamics can be found in several texts [65-67]. In general, the collision geometry is defined in terms of a particle of mass M_1 and energy E which strikes a target atom with mass M_2 which is initially at rest. If there were no interaction between the impinging particle and the target atom, the particle would pass at a distance s_0 from the target atom; this distance is called the impact parameter of the collision. As a result of the interaction, the projectile is scattered through an angle θ relative to the direction of the initial motion and the target atom is recoiled through an angle ϕ relative to the initial motion. Although a complete classical dynamics calculation that follows individual trajectories is required for spectral simulation [68,69], the major spectral features of scattered particles can be classified into the two simple categories described below, for the purpose of interpretation and discussion. The prefix "quasi" is used in these categories to denote that the description is greatly oversimplified, i.e. both the scattering and recoiling trajectories are influenced by more than just one collision partner. However, for the purpose of spectral interpretation, it is extremely useful to have such simple classifications for the major features.

4.1.1. Quasi-single scattering (SS)

Quasi-single scattering (SS) represents the case of one large angle deflection that is preceded and followed by a few very small deflections. This typically produces a sharp scattering peak whose energy is near that of the theoretical single-collision energy. This energy E_s of a particle scattered from a single-collision is given as

$$E_s = E \left[(\cos \theta + (A^2 \pm \sin^2 \theta)^{1/2}) / (1 + A) \right]^2, \quad (10)$$

where $A = M_2/M_1$. If the mass of the impinging particle is smaller than or equal to the mass of the target atom, $M_1 \leq M_2$ and $A \geq 1$, then the positive sign in eq. (10) is used. If the mass of the impinging particle is greater than that of the target atom, $M_1 > M_2$ and $A < 1$, both signs are used in the expression. The energy of the scattered particle is then found to be a double valued function of the scattering angle, i.e. there are two E_s for each θ . For the case of $A < 1$, the maximum SS scattering angle is

$$\theta_{\max} = \sin^{-1} A. \quad (11)$$

4.1.2. Quasi-multiple scattering (MS)

Quasi-multiple scattering (MS) represents the case of at least two large angle deflections that are preceded and followed by smaller deflections. This typically produces a scattering peak that is broader and at higher energy than

the SS peak. The high-energy limit is approximated by repeated application of eq. (10) for each large angle deflection. For example, in a double collision, eq. (10) would be applied twice using scattering angles of $\theta/2$ and the E_s from the first collision as the E input for the second collision. The high-energy limit for MS converges rapidly as several small angles are used to approximate the total scattering angle. The breadth of the MS peak arises from the various multiple-angle combinations that can result in deflection into the laboratory scattering angle θ . Besides the higher energy peak, MS sequences also produce a broad, low-intensity structure that can lie beneath and extend to lower energies than the SS peak. This broad structure is a result of MS sequences that produce slower scattered particles, e.g. a double collision sequence with one backscattering ($> 90^\circ$) collision and one forward scattering collision or a sequence in which a projectile penetrates below the outermost surface layer, loses energy in collisions, and then re-emerges.

4.2. Extension to low energy reactive ions

As previously stated, the binary approximation is applicable to ions with $E > 1$ keV. In contrast, for ions with $E < 1$ eV, particle motions are coupled to the surface phonons and the binary collision approximation no longer provides a valid description of the scattering process. In the intermediate region ($E = 1-1000$ eV) there are gradual transitions from the regime of simultaneous many-body interactions, governed by weak long-range potentials, to that of sequences of quasi-independent binary collisions, governed by strong short-range interactions. Likewise at these lower energies, attractive potentials between active ions and the surface become important.

Tongson and Cooper [70] have studied noble gas scattering using a mass spectrometric technique and concluded that the binary approximation model is valid down to 20 eV, whereas Veksler [71] and Arifov [72] reached the opposite conclusion for the scattering of alkali ions in the same energy range. Hulpke [73] has interpreted the scattering of Li^+ from W(110) and Si(111) surfaces at energies between 2 and 20 eV within the framework of the binary collision model by appending an attractive part to the interaction potential between the colliding partners. The extensive theoretical work of Meyer and co-workers [74] suggests that surface rainbows are due to the corrugation of the interaction potential and therefore allow the determination of the potential hypersurface. Recently, the importance of such ion-atom potentials in atom ejection sequences during reactive ion bombardment simulations has been emphasized by Harrison et al. [75]. These authors have found that at low energies, molecular ejection (some species even containing the impinging reactive ion) is favored over sputtering of atomic species. This observation has significant implications with regard to the correlation of reaction probabilities, reactive ion induced desorption or chemical sputtering of adlayers, deposition

of films by reactive ion bombardment, and associated effects.

Due to the relative lack of experimental data in the low energy regime, the detailed description of the dynamics of ion scattering primarily comes from trajectory simulations. One model, developed by Kasi et al. [49], provides a good description of the trajectories of both noble gas and active ions in the 1–200 eV range. This model generates the classical trajectories by solving Hamilton's equations of motion for a system consisting of the projectile and a model surface atom lattice. The interactive potential for each particle is given as a sum of pairwise contributions and the force acting on the particle is obtained by taking the negative of the potential gradient. The pairwise potential employed was the Biersack–Ziegler [76] (BZ) potential for the noble gas ion and a combination of Morse [77] and Biersack–Ziegler potentials (MBZ) for the reactive ions. The MBZ potential is defined as

$$V_{\text{MBZ}}(s) = f(s) V_{\text{BZ}}(s) + [1 - f(s)] V_{\text{M}}(s), \quad (12)$$

where s is an interatomic distance, $V_{\text{BZ}}(s)$ and $V_{\text{M}}(s)$ are the Biersack–Ziegler and Morse potentials, respectively, and $f(s)$ is the mixing function, given by:

$$\begin{aligned} f(s) &= 1, & \text{for } s \leq s_r, \\ f(s) &= \cos^2[(s - s_r)/2(s_a - s_r)], & \text{for } s_r \leq s \leq s_a, \\ f(s) &= 0, & \text{for } s \geq s_a. \end{aligned} \quad (13)$$

The values of s_r and s_a are determined from the conditions

$$V_{\text{M}}(s_a) = 0 \quad (14)$$

and

$$s_r = s_a/10. \quad (15)$$

The MBZ potential incorporates both a short-range repulsive interaction, modeled by V_{BZ} , and a long-range attractive interaction, modeled by V_{M} .

The differences in the scattering trajectories of a noble gas ion, Ne^+ , and an active ion, O^+ , from Ni are shown in fig. 6. Whereas the scattered Ne flux is strongly focused around 90° and 120° , the O^+ flux exhibits a more isotropic angular distribution.

Selected trajectories representing typical SS and DS events for 50, 100, and 200 eV Ne^+ , O^+ , and C^+ scattering from the model of Ni(111) into a detector at $\theta = 90^\circ$ are shown in figs. 7 and 8. The impact parameters for these trajectories lie on the long axis of the surface cell and, consequently, the trajectories are planar. The ordinates on these plots are the normal distances of the projectiles from the surface and the abscissas represent the projectile coordinate along the surface (figs. 7A and 8A) or the time spent by the projectiles along the course of the trajectory (figs. 7B and 8B). As seen in figs. 7A and 8A, the impact parameters contributing to the scattering angle $\theta = 90^\circ$

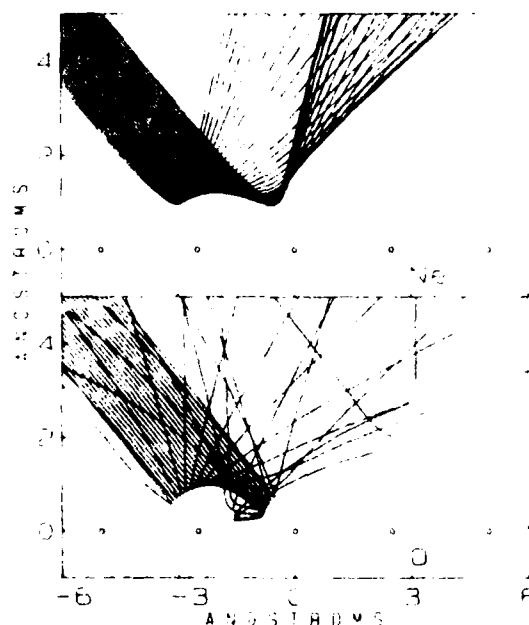


Fig. 6. Trajectory simulations using a one-dimensional string model for 50 eV Ne^+ and O^+ scattering from $\text{Ni}(111)$ at 45° incidence. The BZ and MBZ potentials have been used for Ne^+ and O^+ , respectively. The perpendicular particle-surface distance versus horizontal distance along the surface has been plotted. Atomic centers in the string are indicated by small circles. With permission from ref. [49].

differ slightly for the three projectiles; zero on the abscissa represents the position of the surface target atom that causes the first large angle deflection.

It is clear from these figures that the reactive ion trajectories, particularly those with low energies, are bent towards the surface on both their incoming and outgoing courses and that the large deflections away from the surface take place within rather short sections of the trajectory. On the contrary, deflections of Ne^+ trajectories away from the surface are distributed over larger trajectory segments. It is also apparent from figs. 7A and 8A that in the low E region, ~ 50 eV, the active ions have distances of closest approach (s_0) that are significantly shorter than those of Ne^+ . Such a difference cannot be accounted for by mass considerations alone as attested by the comparable values of s_0 observed at 200 eV. Table 1 lists s_0 for each atom at different energies as predicted by both the MBZ potential and the BZ potential. The ratios of these distances, $s_{\text{rel}} = s_{\text{MBZ}}/s_{\text{BZ}}$, are also listed in table 1. The s_{rel} values decrease with decreasing E , indicating that the effect of the attractive potential on s_0 becomes increasingly important at low energies. This effect is larger for C than for O, consistent with a deeper attractive well depth for C.

The time plots show that the active ions scatter "early" along the trajectory compared to Ne^+ . A combination of the lighter mass and attractive well depth results in this scattering feature of the active ions.

Changes in the interaction potentials along the projectile trajectory have been investigated at 50 and 200 eV for typical SS and MS events and the results are shown in figs. 9 and 10. The corresponding ion trajectories are superimposed on the diagrams. It is apparent that in each case a large deflection occurs within the regions of the repulsive potential maxima. These maxima are broader for Ne than for O and C, particularly at low energies. This indicates that the long-range attractive potential contributions from nearest and next-nearest neighbors make the repulsive potential regions sharper for the active ions. Hence, an impinging Ne^+ ion scatters from a more uniformly corrugated Ni potential hypersurface than O^+ and C^+ . This makes the scattered Ne^+ flux more dependent on the incoming direction (i.e. more anisotropic) in comparison with the scattered flux of O^+ , as indicated in fig. 6. Also, the width of the repulsive scattering regions as well as the shapes of the corresponding projectile trajectories at 50 eV show that the scattering cannot be interpreted as a sequence of nearly independent binary collisions and that a many-body interaction picture must be used to describe the event.

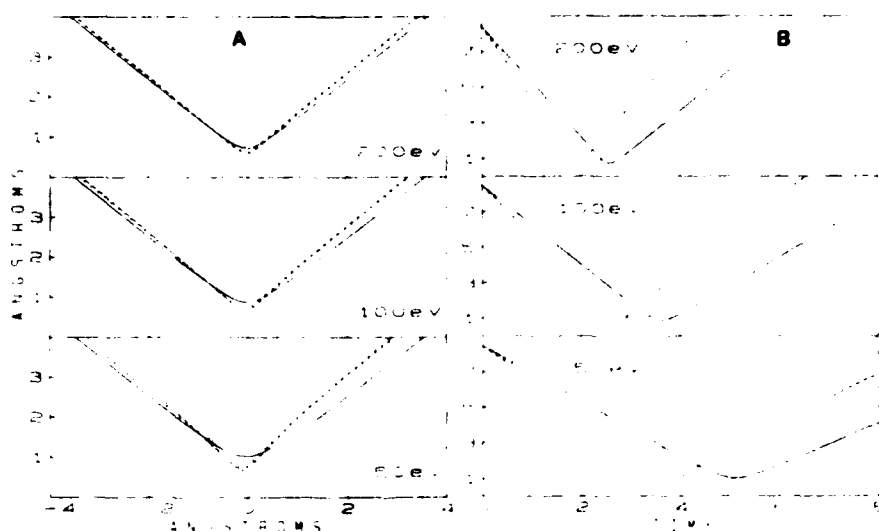


Fig. 7. Trajectory simulations of typical single scattering collisions of Ne^+ (—), O^+ (.....), and C^+ (---) using the BZ potential for Ne^+ and the MBZ potential for O^+ and C^+ . (A) Perpendicular particle-surface distance versus horizontal distance along the surface. (B) Perpendicular particle-surface distance versus time (in fs) along the course of the trajectory. The origin of the ordinate axis represents the outermost atomic layer of the surface. With permission from ref. [49].

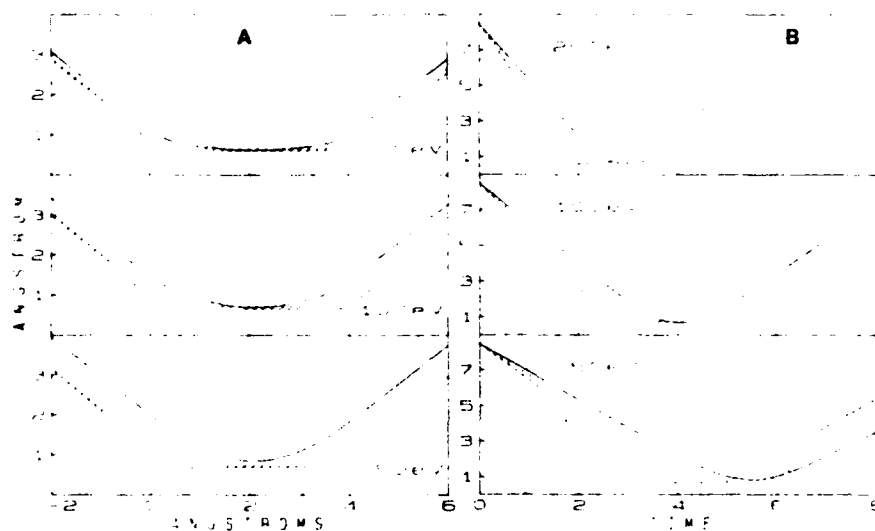


Fig. 8. Similar to fig. 7 but for double scattering collisions. With permission from ref. [49].

Table 1

Calculated fraction of scattered flux (F) and distances of closest approach s_0 for SS and MS ^{a)} of Ne^+ , C^+ , and O^+ from Ni at $\theta = 90^\circ$ and several primary energies E (from ref. [49])

	E (eV)	$F (\times 10^{-5})$ ^{b)}	$s_{\text{MBZ}} (\text{\AA})$	$s_{\text{BZ}} (\text{\AA})$	s_{rel} ^{c)}
Ne^+	200	14	—	0.864	—
		(19)	—	(1.06)	—
	100	34	—	1.06	—
		(30)	—	(1.36)	—
	50	120	—	1.30	—
		(220)	—	(1.60)	—
O^+	200	5.6	0.735	0.816	0.90
		(0.71)	(0.853)	(1.01)	(0.75)
	100	6.5	0.839	1.01	0.83
		(1.0)	(0.982)	(1.27)	(0.77)
	50	5.5	0.930	1.24	0.75
		(1.5)	(1.03)	(1.59)	(0.65)
C^+	200	4.7	0.651	0.753	0.87
		(0.33)	(0.761)	(0.940)	(0.81)
	100	5.0	0.730	0.941	0.78
		(0.39)	(0.853)	(1.18)	(0.72)
	50	4.3	0.799	1.16	0.69
		(0.48)	(0.914)	(1.51)	(0.60)

^{a)} Multiple scattering data are in parentheses.

^{b)} F is proportional to the differential scattering cross-section.

^{c)} $s_{\text{rel}} = s_{\text{MBZ}}/s_{\text{BZ}}$.

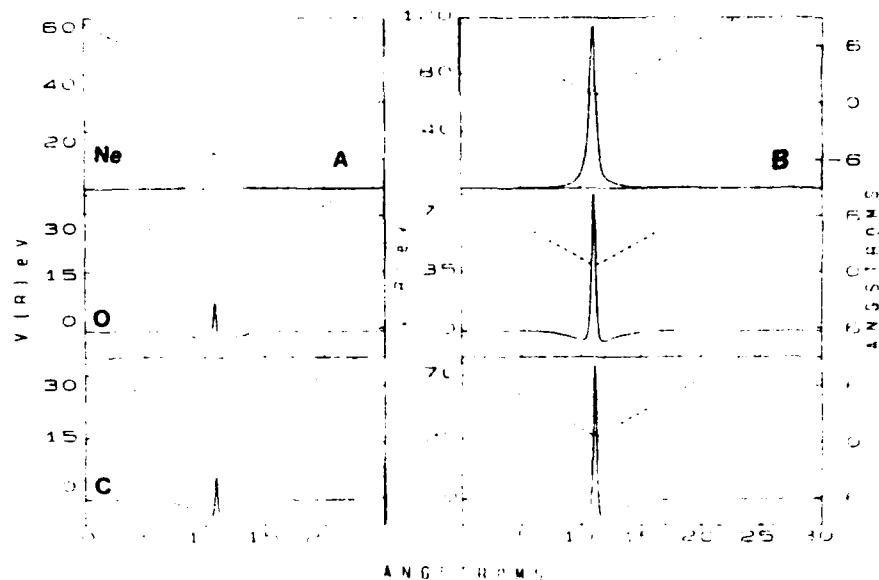


Fig. 9. Plots of the total scattering potential and single scattering trajectories versus distance traveled along the course of the trajectory for Ne^+ , O^+ , and C^+ ions scattering at (A) 50 eV and (B) 200 eV at $\theta = 90^\circ$. The left ordinate labels the potential and the right ordinate labels the normal distance of the particle from the surface. With permission from ref. [49].

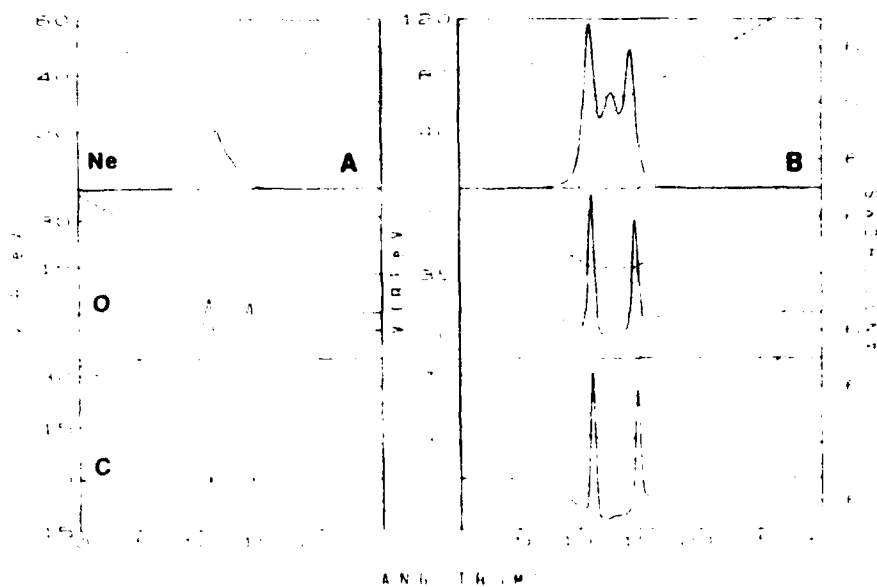


Fig. 10. Similar to fig. 9 but for double scattering collisions. With permission from ref. [49].

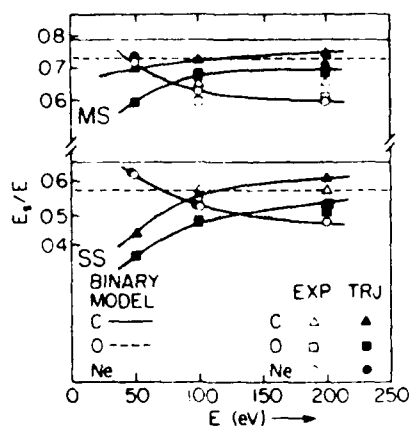


Fig. 11 Plots of the ratio of the scattering energy to primary energy (E_s/E) versus primary energy E from experimental (EXP) SS and MS measurements, the binary collision approximation, and from the trajectory (TRJ) calculations. With permission from ref. [49]

The relevance of such trajectory simulations can be seen by comparison to the available experimental data. Fig. 11 shows the relative scattering energies E_s/E versus E for MS and SS of Ne, C and O from Ni. The scattering energies calculated from the trajectory simulations are in good agreement with the experimental scattering energies. The trajectory calculations successfully predict the steep increase in E_s/E with increasing E for Ne. The calculations also predict a sharp decrease in E_s/E versus E at low primary energies, for active ions, however there is no experimental data to confirm this.

4.3. Scattering of polyatomic ions

The scattering behavior of polyatomic ions in this low energy range is complicated by the presence of several additional degrees of freedom, namely rotation, vibration and dissociation. Fig. 12 shows a typical TOF spectrum for the scattering of 100 eV CO^+ from Ni(111). The spectrum is broad and featureless. This is due to the fact that the scattered flux consists of not only CO but C and O resulting from dissociation. When an incident diatomic ion dissociates, its kinetic energy is distributed to the resulting fragments according to their mass. For CO, 58% of the incident energy goes to O upon dissociation while 42% goes to C. The scattering TOF expected for 100 eV CO multiple scattering as well as for 58 eV O^+ and 42 eV C^+ single and multiple scattering are indicated in fig. 12. As can be seen, the binary collision model provides a good description of the scattering energies for this complex system.

The dominant feature of polyatomic scattering is the collisionally induced dissociation of the ion. There is very little experimental data concerning the

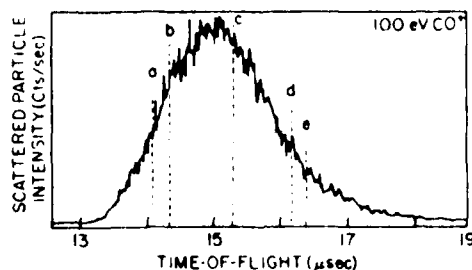


Fig. 12. TOF spectra for 100 eV CO^+ scattering from Ni at 90° . Positions marked are for (a) 42 eV C^+ multiple scattering, (b) 58 eV O^+ multiple scattering, (c) 42 eV C^+ single scattering, (d) 58 eV O^+ single scattering, and (e) 100 eV CO^+ multiple scattering. With permission from ref. [49].

dissociation of polyatomic ions at low energies, however insight may be gained by examining work at higher kinetic energies.

The interaction of keV diatomic ions with surfaces has received a great deal of interest in recent years. When diatomic ions are scattered from surfaces, the scattered flux consists of surviving molecular species in addition to atomic species resulting from dissociation. Most of the work has been concentrated on H_2^+ scattering [28,78–81]. At scattering energies up to several keV, small molecular ion fractions ($\sim < 5\%$) survive the collisions, even though the elastic losses to the surface are much larger than the bond energy of the molecular ion.

Extension to heavier diatomic ions has been confined primarily to N_2^+ [29,31,82–86]. Balashova et al. [31,84] have found that some N_2^+ survives even at collision energies up to 30 keV and also noted a strong directional dependence to the scattered N_2^+ flux. Heiland and Taglauer [83] have observed that molecular ion survival is strongly dependent on the surface condition for N_2^+ scattering from Ni at a primary ion energy of 400 eV and scattering angle of 20° . The molecular ion yield was found to increase by a factor of two for scattering from a nitrated Ni(110) surface as compared to the clean or sulfur covered surface. They attributed this to more effective vibrational quenching of the scattered N_2^+ by surface N than by Ni or S.

4.3.1. General features of diatomic scattering in the keV range

The energy spectra for 2.0 keV N_2^+ scattering from gold and graphite are given in fig. 13 [87]. Each spectrum consists of two peaks, the high kinetic energy peak corresponding to surviving molecular ions and the low energy peak corresponding to dissociated atomic ions. Also shown in fig. 13 are the energies for multiple and single scattering of 2.0 keV N_2^+ and 1.0 keV N^+ calculated from eq. (10). The molecular ion peak occurs at the multiple scattering energy while the atomic ion peak occurs at the single scattering energy. This result is general, having also been observed in CO^+ scattering

from Mg [27]. This is expected as it is more likely that a diatomic ion will survive multiple soft collisions rather than a single hard collision. The second point of importance is the relative width of the molecular peak to the atomic peak. For N_2^+ scattering from gold the atomic peak is twice as broad as the molecular ion peak. This is a common feature to dissociation of high energy diatomic ions [88] and will be discussed in more detail below. The various aspects of diatomic scattering and the mechanism of dissociation will be discussed below.

4.3.2. Classical effects

The first theoretical interpretation of the scattering behavior of polyatomic ions was given by Bitenski and Parillis [89–91]. They employed classical trajectory considerations to explain the survival of high energy molecular ions reflecting from surfaces. Basically they consider the atoms of a diatomic ion to move along independent trajectories. The incoming trajectories are correlated by the bond distance of the molecular ion and the orientation of the molecular axis to the direction of incidence. The scattering trajectories are shown in fig. 14. If the incident molecular orientation is such that the relative kinetic energy

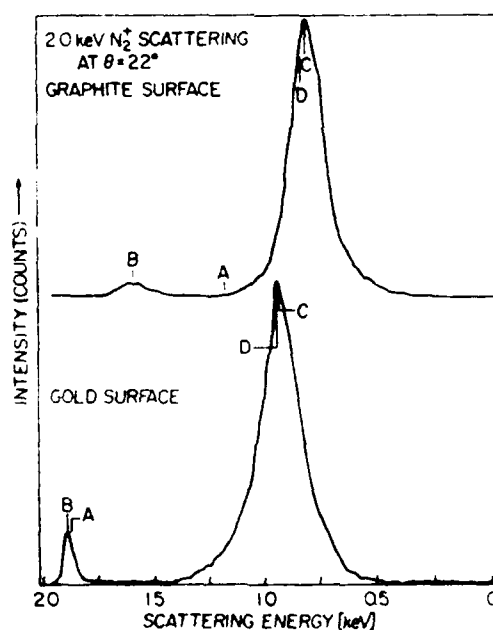


Fig. 13 Positive ion ESA spectra for 2.0 keV N_2^+ scattering from graphite and gold surfaces. The letters represent energies calculated from eq. (10) for the following cases: (A) 2.0 keV N_2^+ single scattering, (B) 2.0 keV N_2^+ double scattering, (C) 1.0 keV N^+ single scattering, (D) 1.0 keV N^+ double scattering. With permission from ref. [87]

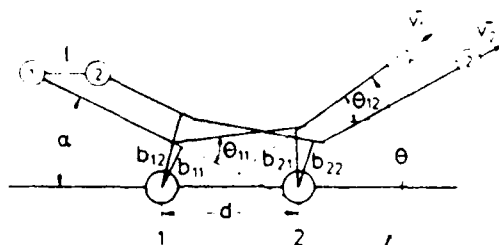


Fig. 14 In-plane double scattering of a diatomic molecule from a single-crystal surface. The surface lattice constant of a low-index crystallographic direction is d , impact parameters are b and scattering angles θ . The internuclear separation of the molecule is l , v_1 and v_2 are the velocity vectors after the scattering. With permission from ref. [93].

of the two atoms after scattering is less than the bond energy, E_b , of the ion, i.e.

$$E_{rel} = \frac{1}{2} M_l (v_1 - v_2)^2 \leq E_b, \quad (16)$$

the scattering is associative. If $E_{rel} > E_b$, the scattering is dissociative. Using this approach they were able to derive expressions for the molecular ion survival fraction. Their treatment also predicts the broadening of the energy distributions of the dissociated atoms which they attribute to self-scattering of the individual atoms. The agreement of this model is good for high energy collisions [31,84] but poor for low energy scattering [86]. One interesting aspect of this model is that it predicts overpopulation of high rotational levels for the surviving molecular ion. This has yet to be confirmed experimentally.

Jakas and Harrison [92] performed Monte Carlo simulations of diatomic scattering and found that such phenomena as target atom recoil and inter-nuclear interactions play an important role in the survival of the molecular ion.

4.3.3 Electronic effects

The most extensive work on electronic effects in diatomic scattering was performed by Heiland et al. [93]. The classical considerations of Bitenski-Parillis and Jakas-Harrison can account for surviving molecular ions, atomic ions and neutrals in the scattered flux of a diatomic ion. These approaches cannot account for the scattering of neutral molecules as this would require electron transfer from the surface to the molecular ion. Scattered neutral molecules have been observed [29,30,49,86,94-96] in time-of-flight spectra of scattered diatomics from a variety of surfaces. For example, fig. 15 shows the time-of-flight spectrum of 550 eV N_2^+ scattering from Ni(111). The scattered ions have been accelerated after scattering. It is clearly observed that

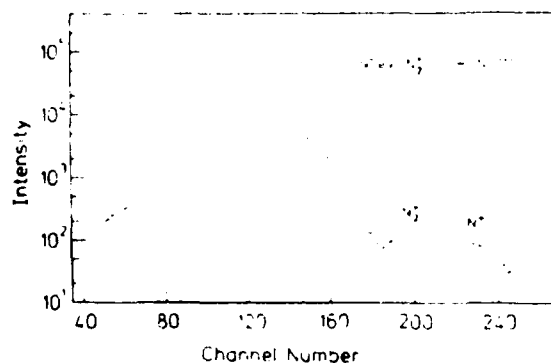


Fig. 15. Time-of-flight spectra of 550 eV N_2^+ scattering from Ni(111). The sharp peak superimposed on the neutral position is due to neutral N_2 . With permission from ref. [93].

the majority of the scattered flux is neutral. Also the sharp feature at the center of the neutral peak is assigned to neutral N_2 scattering. Obviously at the lower energies employed in these experiments, charge exchange with the surface plays an important role.

Heiland et al. [93] have proposed a model for electronic interaction of polyatomic ions with surfaces. Fig. 16 depicts schematically the possible charge exchange processes between an incident diatomic ion and the surface. Neutralization of the incoming ion can proceed via resonant transfer between the surface valence band and molecular orbitals of the ion at the same energy

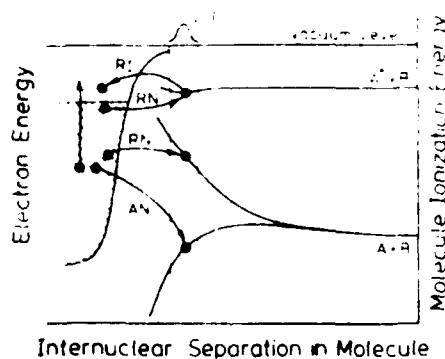


Fig. 16. Schematic illustration of possible charge exchange processes between a molecule and a surface. On the left is the "Fermi-sea" of solid state electrons. To the right the ionization energy of three typical molecular states as a function of the internuclear separation. The states shown are the ground state, an antibonding state correlating with $A + B$ and an excited state correlating with $A^* + B$. Some possible electronic processes are resonant neutralization RN, resonant ionization RI and Auger neutralization AN. With permission from ref. [93].

or by Auger neutralization to molecular orbitals lying below the valence band. Electron transfer into a bound molecular orbital results in neutral molecular scattering. Transfer into an antibonding orbital results in dissociation and neutral atomic scattering. The energy of the transferred electron in excess of the dissociation limit is given off as relative kinetic energy of the resulting fragments upon dissociation. This explains the broadened energy distribution of the scattered molecular fragments. Snowden et al. [95] analyzed the energy distribution of scattered neutral atomic N following N_2^+ scattering from Ni(111) by transforming the experimental energy distributions into relative kinetic energy distributions in the center of mass system. The relative kinetic energy distributions they obtained are shown in fig. 17. The relative kinetic energy distribution is constant for primary ion energies less than 1 keV. At higher ion energies the distributions broaden and the tail extends to higher relative kinetic energies. They attribute this to the contribution of rovibrational excitation at higher primary ion energies. Their work suggests that classical breakup mechanisms (i.e. rovibrational dissociation) is negligible at primary ion energies below 1 keV and that electronic excitation is the primary dissociation mechanism at these lower energies.

Additional support for electronically induced dissociation comes from studies of the effect of lowering the work function of Ni by Cs adsorption on N_2^+ and O_2^+ scattering [96]. The effects are shown in fig. 18. The neutral N_2 yield increases dramatically upon Cs adsorption, clearly indicating the role of electron transfer in the formation of neutral N_2 .

The work of Heiland et al. clearly demonstrates the role of electron transfer in the collisional dissociation of diatomic ions leading to neutral atomic scattering. Sass and Rabalais [87] have recently reported a study of N_2^+ scattering from graphite and gold surfaces. They measured the energy distributions of the scattered N^+ ions resulting from dissociation. These energy

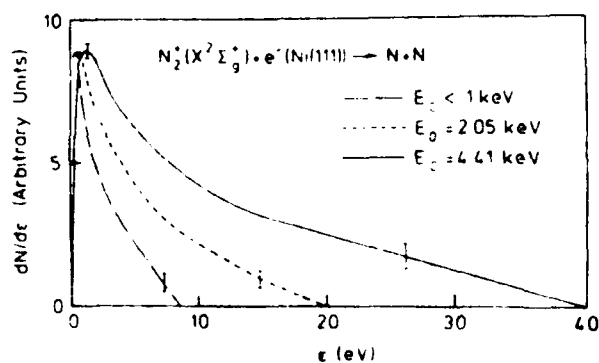


Fig. 17. Relative kinetic energy distribution of N atoms observed following dissociative attachment to N_2^+ at a Ni(111) surface. E_0 is the primary ion energy. With permission from ref. [93].

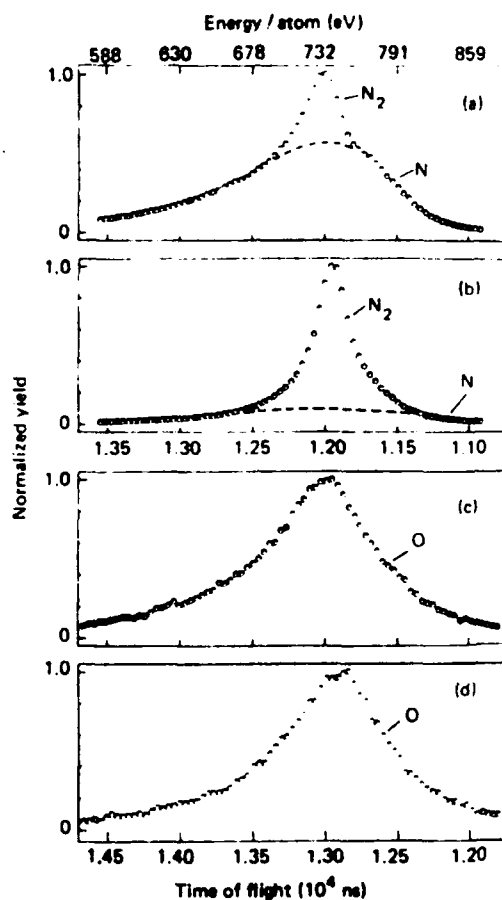


Fig. 18. Neutral particle time-of-flight spectra of 1.5 keV N_2^+ interacting at grazing incidence with (a) clean Ni and (b) Ni + Cs. For O_2^+ under identical conditions (c) and (d) are observed. With permission from ref. [93].

distributions were then converted to relative energy distributions in the center of mass system and are shown in fig. 19. The behavior is similar to the neutral N data of Heiland [95]. These relative kinetic energy distributions reflect the energy released upon dissociation. The incoming N_2^+ can undergo resonant or Auger neutralization according to the mechanism of Heiland [93] leading to neutral scattering. Ionic scattering arises from those molecules which survive in their original charge state or are reionized on the outgoing trajectory. Those molecules which survive in their original charge state collide with a surface atom in the close encounter. In the close encounter significant orbital overlap between the target atom and the molecular ion occurs, resulting in electron

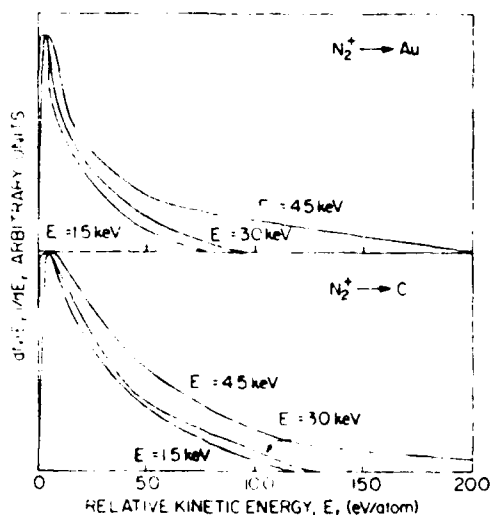


Fig. 19. Relative kinetic energy distributions of the nitrogen atomic N^+ ions resulting from 1.5, 3.0, and 4.5 keV N_2^+ scattering from gold and graphite at $\theta = 22^\circ$. With permission from ref. [87]

promotion according to the Fano-Lichten mechanism [97]. Electron promotion into an antibonding state of the molecular ion results in dissociation. For N_2^+ , the relative kinetic energy distributions indicate that most of the molecu-

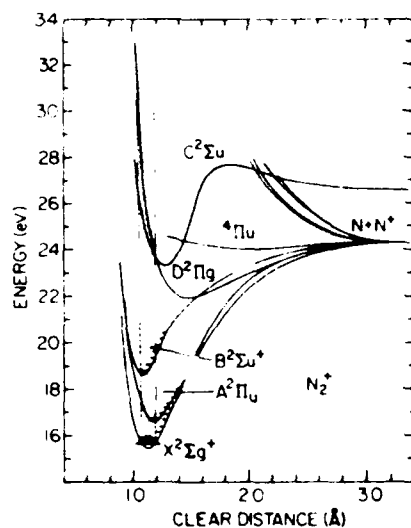


Fig. 20. Energy level diagram for N_2^+ . The ordinate represents the potential energy of an electron bound to N_2^+ . The zero of energy is the zero-point energy of ground state $1\Sigma_g^+$ neutral N_2 . The Franck-Condon region illustrates a transition leading to dissociation into $N(^4S^0) + N^+(^1P)$. With permission from ref. [87]

lar ions dissociate from levels 0–9 eV in excess of the dissociation limit. Examination of the N_2^+ energy level diagram in fig. 20 shows that electronic excitation of N_2^+ in the close encounter to the dissociative $D^2\Pi_g$ state or predissociative $C^2\Sigma_u$ state will give rise to these relative kinetic energies. Thus electron promotion in the close encounter may also play an important role in the collisionally induced dissociation mechanism of molecular ions.

4.3.4. Extension to large molecules

Cooks and co-workers [35,98,99] have studied the fragmentation of large molecules such as metal carbonyls and hydrocarbons following low energy (< 100 eV) impact with metal surfaces by mass spectrometry. The fragmentation patterns show a strong dependence on incidence energy, however in general much richer fragmentation patterns are obtained from this method than from gas-phase collisional induced dissociation. This area of research promises to develop into a powerful new analytical tool in mass spectrometry.

5. Charge transfer process in ion-surface collisions

Inelastic processes in ion-surface collisions can result in the conversion of translational kinetic energy into electronic excitation and ionization of the atoms in the collision pair. This electronic excitation of the scattered or sputtered particles can result in such phenomena as shifts in the scattering energy from the elastic scattering position [10–13], variation in the specific charge states of the sputtered or scattered species [24–26] or emission of electrons and photons from the projectile or target species [14,19].

In the past, most studies of inelastic collisional processes have been carried out in the gas phase [38–40] where the number of inelastic channels is limited. The study of ion-surface collisions is complicated by the multitude of inelastic channels possible. One of the major goals of research in this area is to determine which of these inelastic channels are operative in specific ion-surface collisions.

Projectiles scattered in distinct single binary collisions (SS) with a surface atom offer a unique opportunity to study inelastic ion-surface collisions in that their trajectories and velocities are well defined. Likewise, directly recoiled (DR) surface atoms constitute a specific case of secondary particles for which the collision energy, DR atom velocity, trajectory and point of origin are well known. The study of these well defined cases of primary and secondary particles allows the channels by which the translational energy of the primary ion is converted to electronic excitation and ionization energy to be determined. The fraction of primary or recoiled atoms in an ionized state as a result of a specific scattering or direct recoiling event is determined as the differential ion fraction $Y_{+, -}$. The ion fraction is the ratio of the number of

positive, N^+ , or negative, N^- , ions to the total number of particles recoiled or scattered into a specific solid angle, and is given by

$$Y_{+,-} = [(N + N^{+,-}) - N] / (N + N^+ + N^-), \quad (17)$$

where N is the number of neutrals. In this chapter we will attempt to give an overview of the methods by which ion fractions are measured and the information that the measurement of ion fractions provide on the charge exchange channels operative in ion-surface collisions.

5.1. Experimental considerations

The measurement of scattered and recoiled ion fractions requires the ability to separately analyze the scattered or recoiled neutral and ion flux. Two basic

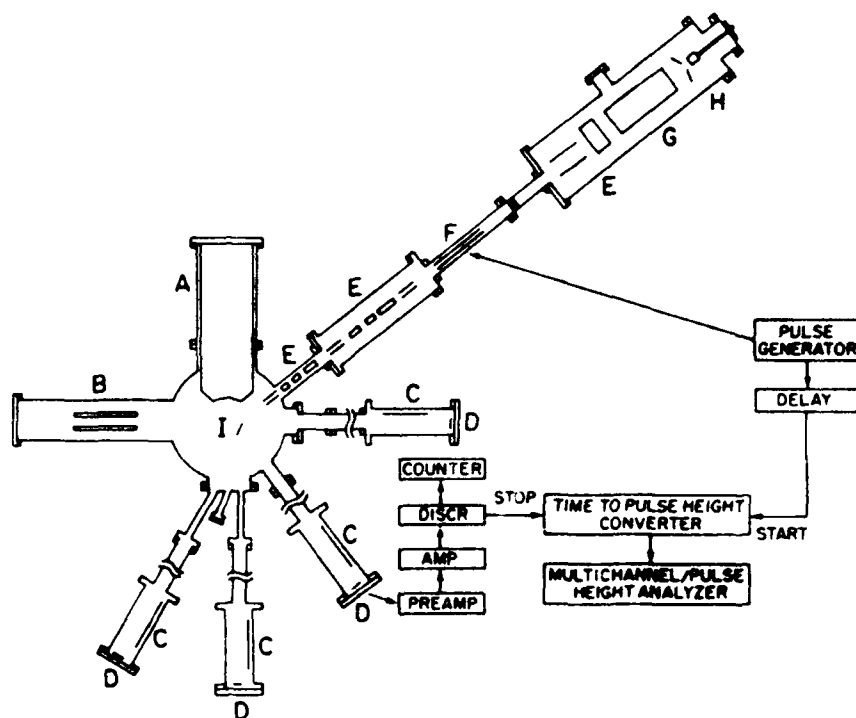


Fig. 21 Schematic diagram of UHV chamber for TOF scattering and recoiling, X-ray and UV photoelectron spectroscopy, and mass spectrometry (A) cylindrical mirror electron analyzer, (B) quadrupole mass spectrometer, (C) electrostatic deflector, (D) electron multiplier detector, (E) electrostatic lens, (F) pulse plates, (G) Wien filter, (H) Colutron ion source, and (I) sample. The UV and X-ray sources project out of the plane of this diagram and are not shown. With permission from ref. [125].

approaches to this problem have been employed. In the first approach [100], the reflected ions are first analyzed with an electrostatic analyzer. The neutrals are then analyzed by first electrostatically deflecting the scattered ions from the scattered flux. The remaining scattered neutrals then pass into a stripping cell where they are ionized by collisions with a buffer gas. The resulting ions are then analyzed with the electrostatic analyzer. The ion fraction is then the ratio of the signal for scattered ions to the signal when the neutrals are ionized. This approach suffers from the efficiency of the stripping cell which limits the accuracy of the measured ion fractions and the types of species which can be studied.

The second method for the measurement of ion fractions employs time-of-flight detection of the scattered and recorded particles [25]. A schematic of the apparatus used in these experiments is given in fig. 21. Basically, a pulsed ion beam is directed at the sample and the scattered and recoiled flux is velocity analyzed by time-of-flight (TOF) techniques. TOF analysis allows the simultaneous measurement of the velocity spectrum of both the neutrals and ions. The TOF spectrum of the neutrals only is then measured by electrostatic deflection of the scattered ions before they reach the detector. The ion fraction can then be obtained by subtracting the neutral only (N) spectra from the ion plus neutral ($N^+ + N^- + N$) spectra. The ion fractions determined by this method are more accurate than those determined with the use of a stripping cell since the neutrals are measured directly. It is also applicable to any system. This method does suffer, however, from the inherently lower resolution of the TOF velocity analysis than electrostatic energy analysis.

5.2. Model for scattered ion fractions ($Y_{+,-}$)

Scattered ion fractions have been measured for several ion/surface combinations [19,24,25,100–110]. For noble gas [109] and active ions [105] on metal surfaces, Y_{+} values range from 0–70%, while for alkali ions [110], Y_{+} is typically > 80%. In order to trace the phenomena that contribute to this wide range in scattered ion fractions, the collision sequence must be analyzed at all points of the scattering trajectory. Due to their low ionization potentials, the alkali ions represent a specific case of primary ion and will be treated separately below.

We divide the ion trajectory near the surface into three segments: (i) the incoming trajectory, (ii) the close encounter, and (iii) the outgoing trajectory. In steps (i) and (iii), it is assumed that charge exchange occurs via Auger and resonant transitions according to the treatment of Hagstrum [111]. In segment (ii), the ionization and neutralization probabilities are determined by the distance of closest approach, s_0 , according to the Fano-Lichten mechanism [97,112].

5.2.1. Incoming and outgoing trajectories

The transition rate $R(s)$ along the incoming or outgoing trajectory is assumed to be only a function of the perpendicular distance s of the ion from the surface. Assuming a simple exponential rate function [111],

$$R(s) = A \exp(-as), \quad (18)$$

where A (time⁻¹) is a pre-exponential constant and a (distance⁻¹) determines the ion-surface interaction range. Defining $P_i(s, v_i)$ as the probability that a particle with incoming velocity v_i perpendicular to the surface will reach s in its original charge state, it can be shown that

$$P_i(s, v_i) = \exp[-(A_i/av_i) \exp(-as)]. \quad (19)$$

For an outgoing particle, $P_o(s, v_o)$ is the probability that a particle with outgoing velocity v_o perpendicular to the surface will reach $s = \infty$ in its original charge state and is given by

$$P_o(s, v_o) = \exp(A_o/av_o) [\exp(-as) - 1]. \quad (20)$$

5.2.2. The close encounter

In the close encounter, we define two additional processes, $P_N(s_0)$ and $P_I(s_0)$ which are functions only of the distance of closest approach s_0 for a given projectile/target combination. $P_N(s_0)$ is the probability for neutralization of ions that have survived the incoming trajectory and $P_I(s_0)$ is the probability that neutrals formed along the incoming trajectory will be re-ionized at s_0 . The mechanism for $P_N(s_0)$ and $P_I(s_0)$ is according to electron promotion in the close encounter as described by united-separated atom diagrams [97,112], i.e., the Fano-Lichten mechanism. These processes, coupled with electron transfer on the incoming trajectory, P_i , and outgoing trajectory, P_o , are shown schematically in fig. 22.

In the discussion above, it was assumed that the scattered primary ion can assume only two charge states, namely $m = 0, +1$. This is because the production of negative charge states for noble gas ions, the primary ions used in the majority of these studies, is negligible. Also at the primary ion kinetic energies used in these studies (0.1–10 keV), the production of multiply charged positive ions is insignificant.

5.2.3. Final Y_i expressions

Based on these assumptions, expressions for the scattered ion fractions Y_i are derived by considering a primary ion beam of N_0^+ ions impinging on the surface. The yield of scattered atoms in charge state m , N^m , is given by

$$N^m = kN_0^+ (d\sigma/d\Omega) \Delta\Omega nP^m, \quad (21)$$

where k is a spectrometer constant, $d\sigma/d\Omega$ is the differential scattering cross

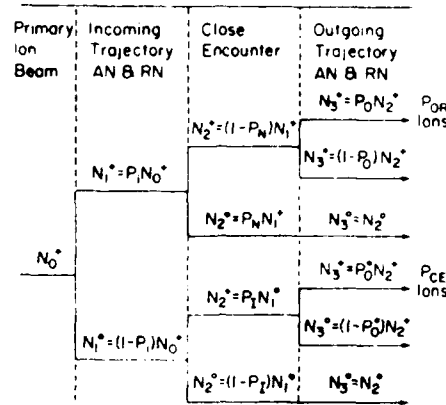


Fig. 22 Derivation of the probabilities for consecutive neutralization and ionization along the three segments of the ion trajectory. Only two channels yield ions: the upper channel produces P_{OR} type and the lower channel produces P_{CE} type ions. With permission from ref. [109].

section, $\Delta\Omega$ is the acceptance solid angle of the detector, n is the surface atom density and P^m is the probability for atom N to be in charge state $m = 0, +1$ at $s = \infty$ following a scattering event. Tracing the probabilities for consecutive neutralization and ionization along the three segments of the scattering trajectory as shown in fig. 22, it is found that only two channels yield scattered ions, P_{OR} and P_{CE} . P_{OR} represents ions which have survived neutralization in all three segments of the scattering trajectory while P_{CE} represents ions formed by reionization of neutrals formed on the incoming trajectory in the close encounter. The overall positive ion scattering probability is then

$$P^+ = P_{OR} + P_{CE}, \quad (22)$$

where

$$P_{OR} = P_I P_0 (1 - P_N), \quad (23a)$$

$$P_{CE} = (1 - P_I) P_I P_0. \quad (23b)$$

The neutral scattering probability is given by

$$P^0 = P_I (1 - P_N) (1 - P_0) + P_I P_N + (1 - P_I) P_I (1 - P_0) + (1 - P_I) (1 - P_I). \quad (24)$$

The scattered ion fraction is then

$$Y_+ = N^+ / (N^+ + N^0) = P_{OR} + P_{CE}. \quad (25)$$

Eq. (25) has the expected behavior in the limits of low and high kinetic energy. For example, at low incidence energy where s_0 is large, inelastic processes in

the close encounter are negligible, hence

$$P_N = P_I \rightarrow 0 \quad \text{and} \quad Y_+ = P_I P_0$$

as described by Hagstrum [111]. In the high energy limit,

$$v_i = v_0^\infty,$$

and therefore

$$P_I = P_0 \rightarrow 1.$$

Y_+ is then given by

$$Y_+ = 1 - P_N,$$

i.e., the only neutrals are those produced in the close encounter.

5.2.4. Transition probabilities

Rigorous calculation of the electronic transition probabilities or charge exchange probabilities in the close encounter and along the incoming and outgoing trajectories are beyond the scope of this paper. Such calculations represent an active area of research [113–119]. This section presents a qualitative approach which can be used to understand the general behavior of ion surface charge exchange.

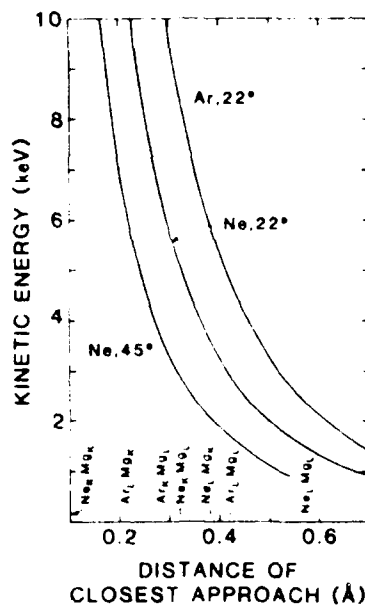
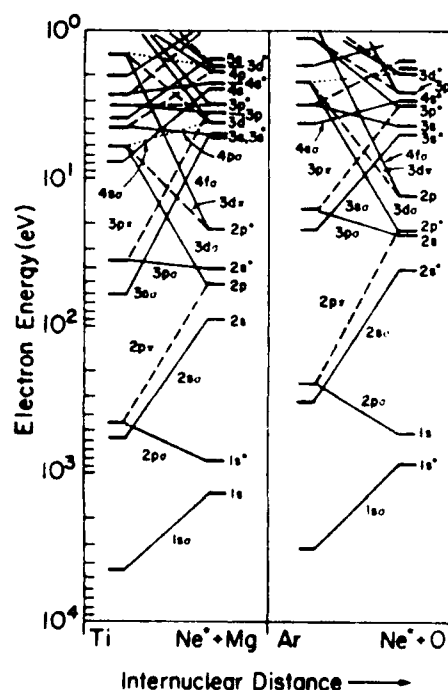


Fig. 23. Calculated distances of closest approach versus primary ion kinetic energy for Ne/Mg collisions at 22° and 45° and Ar/Mg collisions at 22°. The sum of the radii of maximum radial charge density for various combinations of the L and K shells are indicated on the figure. With permission from ref. [109].

Consider electron promotion in the close encounter. The processes occurring in the close encounter P_1 and P_2 have a strong dependence on the actual distance between the colliding atoms. The distance of closest approach s_0 can be calculated from scattering calculations [109]. Plots of s_0 versus E are shown in fig. 23 along with the positions corresponding to the sum of the radii of maximum radial charge density for various combinations of electronic shells of importance in Ne^+ and Ar^+ collisions with Mg. The plots show that for incidence energies greater than ~ 2 keV, significant penetration of the core atomic shells is achieved.

Specific electron promotions in the close encounter can be predicted [112] by constructing separated-united atom diagrams and using diabatic correlations [120]. Such diagrams, as fig. 24, show that as the separated atoms merge to form a molecule, filled MO's resulting from inner shells cross neutral MO's that correlate to higher principle quantum number AO's of the separated atoms. As atoms approach and recede from each other, electronic transitions



can occur at these crossings with the result that electrons can be trapped in AO's of high principal quantum number. The resulting electronic configurations yield autoionizing and highly excited discrete states whose lifetime (10^{-7} – 10^{-9} s) are longer than the collision times (10^{-11} – 10^{-12} s).

For Ne-Mg collisions, fig. 24, the diagram shows that excitation energy can be channeled into Ne through its 2p orbital which correlates with the highly promoted 4f σ MO. Electronic transitions [121] from the 4f σ MO to other σ MO's (e.g., 3s, 4p, 4s, etc.) can occur via radial coupling and transitions to π MO's in which the component of orbital angular momentum along the internuclear axis, Λ , changes by one unit (e.g., 3p, 3d, 4f) can occur by rotational coupling. Autoionizing and excited states produced in this encounter are major contributors to high Y_p values. Although such diagrams are only qualitative, the significant feature is that electrons occupying highly promoted MO's are very weakly bound to the molecule (~ 1 eV binding energy) and are easily ionized.

Consider the incoming and outgoing trajectory of the scattered particle. Electronic transitions along these trajectories are governed by the relative positions of the electronic energy levels of the solid and scattered particle. The transitions can be divided into two categories, resonance and Auger transitions. Letting N^m represent a scattered ion of charge state m and S represent a target surface with x electrons in its valence band, a resonance transition can be represented as



In such a resonance surface-to-particle charge-transfer transition ($S \rightarrow N$) an electron tunnels from a filled level of the solid into a level containing a vacancy at the same energy of the particle. Transition 1 or ($S \rightarrow N$) can occur only when the particle possesses a vacancy in the level E_i^* which is within the energy bounds $|E_f| < |E_i^*| < |E_B|$ or $|E_f| < |E_i^*| < |E_B|$. Resonant particle-to-surface charge-transfer ($N \rightarrow S$) transitions can only occur when the scattered particle possesses an occupied level E_i^* which satisfies the condition $E_i^* < E_f$ and $E_i^* < E_t$.

A two-electron or Auger surface-to-particle charge-transfer transition ($\leftarrow S \rightarrow N$) involves the simultaneous transition of two electrons such as



In this process an electron from a filled valence band of the solid tunnels into the scattered particle well and drops into a discrete vacant level; a second electron of the solid is excited into the conduction band or ejected into the continuum. An Auger transition can only occur when the scattered particle possesses a vacancy in the level E_i^* which satisfies the conditions, for a metal $E_f < E_i^*$ and for an insulator $|E_f| < E_i^*$ and $|E_i^*| < |2E_f| - |E_t|$.

5.3. Extension of model to directly recoiled (DR) ion fractions

DR ion fractions are typically less than 30% [122–125]. The model of ion fractions of scattered ions is directly applicable to the ion fractions of DR particles with two modifications. First, since the DR particle originates at the surface, its trajectory consists of only two segments: (i) the close encounter and (ii) the outgoing trajectory. Secondly, the original charge state of the DR atom in the surface is not as clearly defined as an impinging ion.

Two Fano-Lichten type processes are defined in the close encounter, P_-^m and P_+^m . Considering target atoms in charge state m , P_-^m is the probability that these atoms will be reduced to charge state $(m-1)$ and P_+^m is the probability that these atoms will lose one electron to produce charge state $(m+1)$ as a result of the collision. These processes are shown schematically in fig. 25. Here the subscripts 1, 2, and 3 denote, respectively, the undisturbed target atom, the atom immediately after the close encounter with a projectile atom, and the atom infinitely far from the surface following the outgoing trajectory. Prior to the close encounter, the number of target atoms in charge state m is N_1^m . Following the encounter the charge states are described by N_2^n , where $n = m, m+1, \dots, 1$ for $m = -1$ and 0 and $n = 0$ and 1 for $m = 1$. These bounds limit the maximum charge state to $n = +1$ and prohibit the reduction to negative ions $n = -1$ as a result of the collision. The upper limitation $n = +1$ is used for simplification and because previous studies [109] have

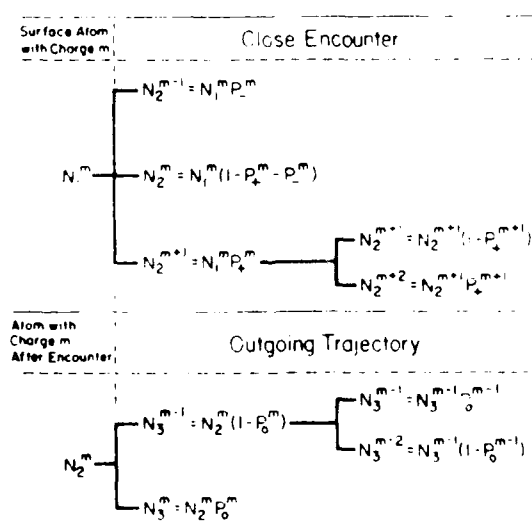


Fig. 25. Derivation of the probabilities for consecutive charge exchange during the close encounter and outgoing trajectory of a DR sequence. With permission from ref. [124]

shown that the fraction of multiply charged DR ions produced in this energy range is low. The neglect of reduction to $n = -1$ during the collision is supported by experimental data, for, as expected, a relatively unstable species such as a negative ion will tend not to survive in the violent high-energy environment of the close encounter.

Electron exchange on the outgoing trajectory occurs via the same mechanism as for scattered ions. The probability that the particle will reach $s = \infty$ in charge state m is given by eq. (20).

These processes are shown schematically in fig. 25. At $s = \infty$, the charge states are described by N_s^n , where $n = m, m-1, \dots, -1$. This limits electronic processes on the outgoing trajectory to electron pickup by the particle, i.e., charge reduction down to $n = -1$ rather than the energetic process of electron loss by the particle, e.g., ionization. Using the scheme of fig. 25, the probabilities for production of a DR in charge state m , P^m , can be derived for various initial charge states. The resulting $Y_{i,0}$ values are listed in table 2; here the initial negative and positive charge states are taken as -1 and $+1$.

Analogous arguments to those for scattered ions give a qualitative description of the transition probabilities of DR. Fig. 26 shows that in Ar-Si and Ar-O collisions, excitation energy can be channeled into Si and O via their 2p levels which correlate with the highly promoted 4f σ MO. Electronic transitions to 4f σ and other promoted MO's produce autoionizing states in the DR as the atoms recede. Transitions to partially filled Si 3p or O 2p orbitals can produce high $Y_{i,0}$ values. Experimentally it is observed that $Y_{i,0}$ values for O⁺ and C⁺ DR are considerably lower than those for Si⁺ [124].

Table 2
Expressions for $Y_{i,0}$ for initial neutral, negative, and positive bonding environments and the limits of Y as $s_0 \rightarrow \infty$ and 0 (from ref. [109])

	Limits of $Y_{i,0}$	
	$s_0 \rightarrow \infty$ $v_0 \rightarrow 0$	$s_0 \rightarrow 0$ $v_0 \rightarrow \infty$
<i>DR from neutral environment</i>		
$Y_{i,0} = P_0^n P_0^+$	0	P_0^n
$Y_{i,0} = P_0^n (1 - P_0^+ P_0^+)$	P_0^n	$1 - P_0^+$
$Y_{i,0} = 1 - P_0^n (1 - P_0^+ P_0^+)$	$1 - P_0^n$	0
<i>DR from negative environment</i>		
$Y_{i,0} = P_0^- P_0^0 P_0^+$	0	$P_0^- P_0^0$
$Y_{i,0} = P_0^n P_0^- (1 - P_0^+ P_0^+)$	0	$P_0^- (1 - P_0^+)$
$Y_{i,0} = 1 - P_0^n P_0^- (1 - P_0^+ P_0^+)$	$1 - P_0^n P_0^-$	$1 - P_0^-$
<i>DR from positive environment</i>		
$Y_{i,0} = P_0^n (1 - P_0^+)$	P_0^n	$1 - P_0^+$
$Y_{i,0} = P_0^n [1 - P_0^+ (1 - P_0^+)]$	$P_0^n (1 - P_0^+)$	P_0^n
$Y_{i,0} = 1 - P_0^n (1 - P_0^+) - P_0^n [1 - P_0^+ (1 - P_0^+)]$	$1 - P_0^n - P_0^n (1 - P_0^+)$	0

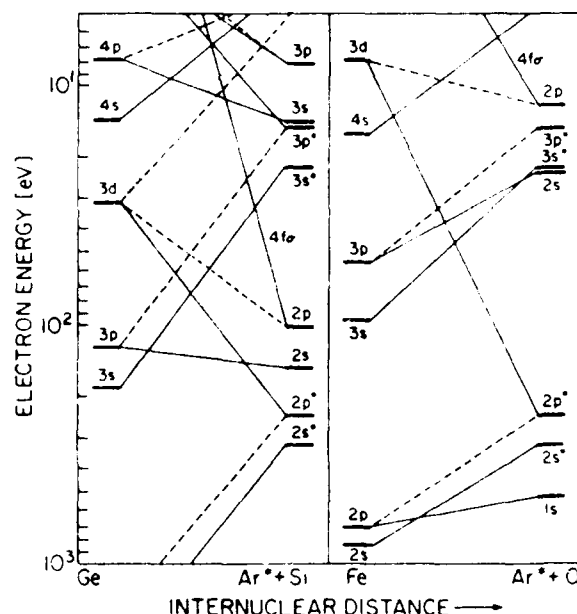


Fig. 26. United atom (UA) - separated atom (SA) correlation diagrams for electrons in the field of two differently charged nuclei. Diabatic MO's connect the levels of the infinitely separated atoms (right side) with those of the united atoms (left side), maintaining the same value of the quantum number difference ($n - l$). The diagrams are specifically for Ar/Si and Ar/O collisions and experimental energy levels are used. MO's with $M = 0, 1, 2$ (σ, π, δ) are denoted by solid, dashed, and dotted lines, respectively. With permission from ref. [124].

This result is in agreement with the predictions of Barat and Lichten [112], i.e., excitation cross sections should rise to a maximum for collision partners of similar Z and decrease with increasing Z . The similar atomic number of Ar and Si results in good orbital matchups and efficient promotion.

In the outgoing trajectory, resonance charge exchange can occur between the DR and the surface as shown in fig. 27 for Mg DR from Mg and MgO. Auger transitions are also important as shown in fig. 28 for Si DR from Si and SiO₂.

For the Si case, Si⁺ ions can be neutralized by ($S \rightarrow N$) and ($\leftarrow S \rightarrow N$) transitions and Si⁻ ions can be neutralized by ($N \rightarrow S$) transitions. Emerging neutrals cannot undergo ($N \rightarrow S$) transitions to produce positive ions because the valence band of Si is filled. For SiO₂ the large band gap makes it improbable for emerging Si⁺ and Si⁻ to undergo charge exchange processes with the surface, resulting in enhanced Y_{e} values.

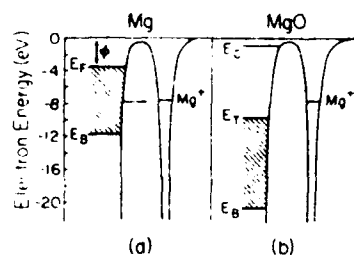


Fig. 27. Electron energy diagrams representing a particle departing a surface as a result of a collision. The electronic band structures are for magnesium metal (a) and magnesium oxide (b) and the discrete ionization potential of Mg is shown in the potential well. The abscissa represents the distance from the surface to the departing particles, and the ordinate represents the energy of an electron in the solid or particle. The filled valence band is shown shaded. The most probable charge-transfer electron transition that can occur between the particle and the surface while the departing particle is within ångströms of the surface is indicated. This represents a resonance surface-to-particle ($S \rightarrow N$) transition from the valence band to vacant level, E_p^+ , of the particle, e.g., resonance neutralization of a departing positive ion into an excited level or ground state of the neutral species. A resonance particle-to-surface ($N \rightarrow S$) transition from an occupied level, E_p^+ , of the particle into the conduction band can occur if the two levels are resonant. A two-electron Auger process in which a valence band electron tunnels into a particle vacancy at E_p^+ and the energy gained is transferred to another valence band electron which can be excited into the conduction band or ejected into the continuum, e.g., Auger neutralization of a departing positive ion can occur if $|E_p^+| < |E_C|$ for a metal and $|E_p^+| > |2E_F| - |E_C|$ for an insulator. With permission from ref. [123].

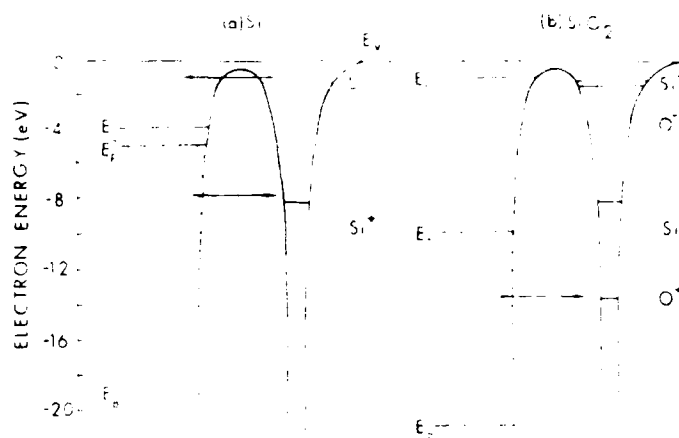


Fig. 28. Electron energy diagrams representing DR particle emission from (a) silicon and (b) silicon dioxide. With permission from ref. [123].

5.4. Examples of DR and scattered ion fractions

Fig. 29 shows the primary ion energy dependence of the scattered ion fractions of Ne^+ and Ar^+ from Mg. The Y_{sc} values are strongly dependent on the primary ion kinetic energy E and scattering angle θ . The Y_{sc} values all rise steeply at low energies and reach a plateau at high energies and they are several times higher for collision partners of similar Z , e.g. Ne^+ /Mg, than for partners of widely different Z .

Y_{sc} values for direct recoils show a similar threshold behavior as shown in fig. 30 for F^+ and Li^+ recoil from LiF . The F^+ fraction and Y_{sc} values in general show a very different behavior, usually exhibiting a maximum or flat region at some intermediate energy and decreasing with increasing energy. It is evident that the Y_{sc} and Y_{dr} values show a distinctly different energy dependence.

5.5. Applications of the models of scattered and DR ion fractions

5.5.1. Scattered ion fractions

Eq. (22) has several unknown parameters including P_{sc} , P_{I} , A_{sc} , A_{I} , and a . In order to fit this expression to experimental data, it is necessary to make the assumption of equality in the close encounter. This assumes that at a given distance of closest approach s_{sc} , P_{sc} and P_{I} are constant and independent of E and scattering angle θ . Eq. (22) can then be solved for P_{sc} and P_{I} .

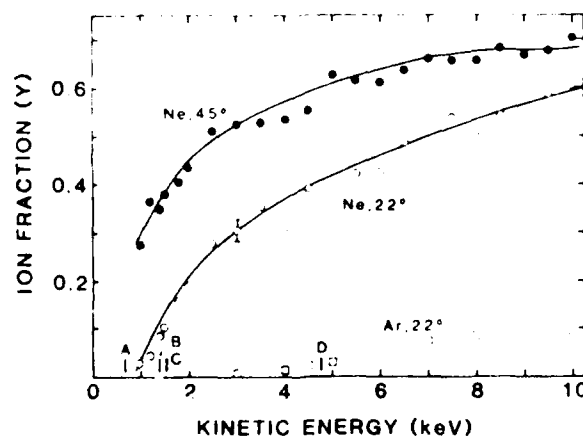


Fig. 29 Scattered ion fractions Y_{sc} versus primary kinetic energy E for Ne^+ scattering at 22° and 45° and Ar^+ scattering at 22° from Mg. The kinetic energies corresponding to overlap of specific atomic shells are indicated on the figures as A = Ne_LMg_L (45°), B = Ne_LMg_L (22°), C = Ar_MMg_K (22°), D = Ar_LMg_L (22°). The solid lines represent the fit of eq. (11) to the Ne^+ /Mg 22° and 45° data. With permission from ref. [109].

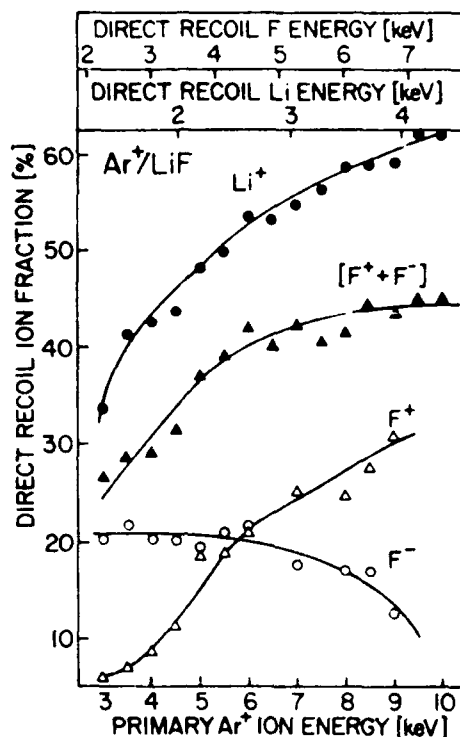


Fig. 30. Direct recoil Li^+ , F^+ , F^- and $(\text{F}^+ + \text{F}^-)$ ion fractions from Ar^+ bombardment of LiF . With permission from ref. [125].

The model predicts that $Y_i = P_0 P_i$ in the low energy limit. Fig. 31 shows a plot of $\ln Y_i$ versus $(1/v_i + 1/v_{0i})$ (eqs. (19) and (20)). The plot is linear, as expected, for energies below 4 keV for Ar^+/Y^+ collisions at 22° . No linear region is observed at 45° scattering angles, indicating that the low energy limit is obtained only for lower incident kinetic energies (larger s_0 values).

The slope of the line in fig. 31 gives an estimate of the parameter ratio $A/a = 5.5 \times 10^6 \text{ cm/s}$. This ratio has been labeled [41–43] the “characteristic velocity” v_c . The linearity of the plot indicates that excitations in the close encounter, P_c and P_i , are negligible at $E < 4.0 \text{ keV}$ and $\theta = 22^\circ$ but not at 45° for even the lowest energies measured. Similar results are obtained for Ne^+/Mg collisions [123] in which P_i and P_c were negligible at $E < 1.5 \text{ keV}$ and $\theta = 22^\circ$ but not at higher scattering angles. Estimates of $v_c = A/a$ [126–128] range from 10^6 – 10^8 cm/s and the values determined from this model fall well within this range. Fitting eq. (22) to the experimental data gives $3 < a < 6 \text{ \AA}^{-1}$ and transition rates of $10^{14} < A < 10^{15} \text{ s}^{-1}$. This is the expected order for radiationless Auger and resonant transitions.

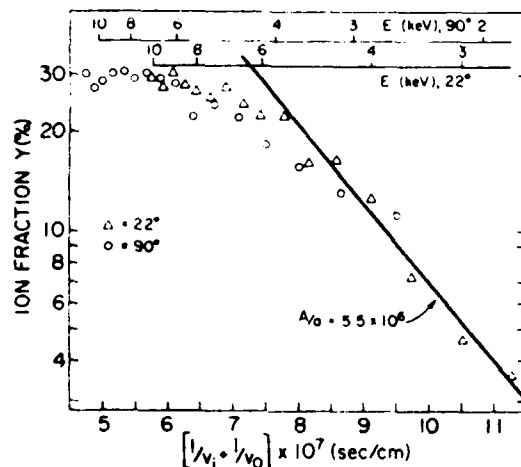


Fig. 31. Plots of scattered ion fractions Y_s versus $(1/v_i + 1/v_0)$ for Ar^+ scattering from Y at 22° and 90° . The component of the velocities perpendicular to the surface is used. The straight line represents a linear least-squares fit to the first five points on the 22° data. With permission from ref. [109].

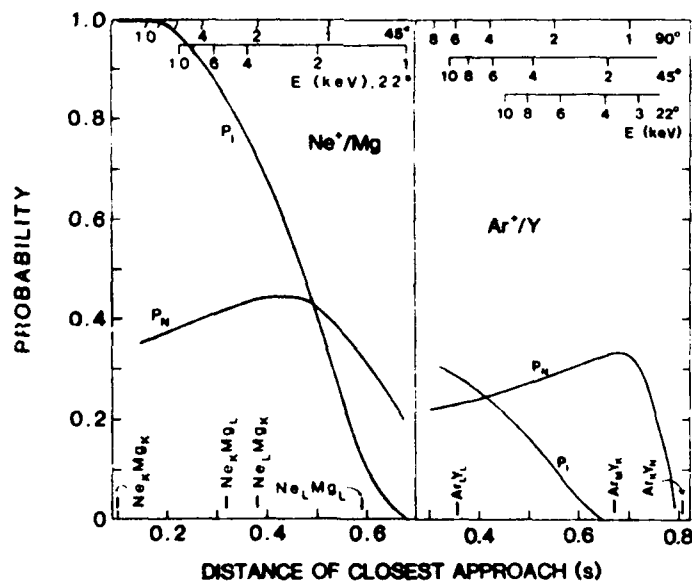


Fig. 32. Values of the probabilities P_1 and P_N as a function of the distance of closest approach derived by fitting eq. (11) to the experimental data. The positions corresponding to the sum of the radii of maximum radial charge density for various combinations of electronic shells are indicated on the diagram. With permission from ref. [109].

The values of P_N and P_I determined from fitting the data for Ne^+/Mg and Ar^+/Y collisions are shown in fig. 32. Consider the Ne^+/Mg results. The probability P_I of reionization of neutrals formed on the incoming trajectory rises from zero at $s_0 = 0.68 \text{ \AA}$ to unity at $s_0 = 0.17 \text{ \AA}$. The steep rise begins near the s values corresponding to the distance for Ne L-Mg L shell overlap. The probability P_N of neutralization of ions surviving the incoming trajectory goes through a maximum in the 0.3–0.6 \AA region. In general as s_0 decreases P_I and P_N increase due to electron promotions resulting from L shell overlaps. In this region $P_N < P_I$ because the small inelastic losses provide for preferential population of the lower energy excited states rather than higher energy autoionizing states. For $s_0 < 0.5 \text{ \AA}$, P_I continues to increase while P_N decreases slowly. In this region, the large inelastic losses result in preferential population of autoionizing states, yielding high ion fractions.

5.5.2. Positive DR ion fractions

The expressions of table 2 show that Y_+ in a neutral environment is determined by the ionization probability in the close encounter P_+^0 and the survival probability P_0^+ of the ion leaving the surface. Similar expressions are obtained for the two other environments. In the negative environment there are two consecutive ionization probabilities in the close encounter, i.e., from negative to neutral (P_-^+) and then from neutral to positive (P_+^0). In the positive environment, $(1 - P_+^+)$ is the probability that a positive surface atom is not neutralized in the close encounter. The expression for the neutral environment $Y_+ = P_+^0 P_0^+$ has two parameters, P_+^0 and A/a , which must be determined for each projectile-target pair. Plots of $\ln Y_+$ versus $1/v_0$ do not provide satisfactory linear plots, for P_+^0 is velocity dependent [106,107]. As previously discussed, values of A/a were determined for Ne^+ scattering from Mg and Ar^+ scattering from Y at low energies where P_+^0 approaches zero; these values are 4.9×10^6 and $5.5 \times 10^6 \text{ cm/s}$, respectively. Such low energies are not practical for DR measurements because relatively high ion energies are required to produce DR neutrals that are sufficiently energetic for detection. Due to the relative insensitivity of the previously determined [109] A/a values to the specific scattering system, an average value of $A/a = 5 \times 10^6 \text{ cm/s}$ is used in the expression $Y_+ = P_+^0 P_0^+$ for the purpose of observing the energy dependence of P_+^0 . The resulting P_+^0 values as a function of energy are shown in fig. 33. The somewhat arbitrary manner of assigning A/a renders arbitrariness in the resulting P_+^0 values, however the trends observed in P_+^0 as a function of energy remain valid and provide a physical interpretation of the ionization process. In all three cases, P_+^0 rises from a small value at low energy and reaches a plateau region at higher energy.

5.5.3. Negative DR ion fractions

The expressions of table 2 show that Y_- , for atoms in a neutral environ-

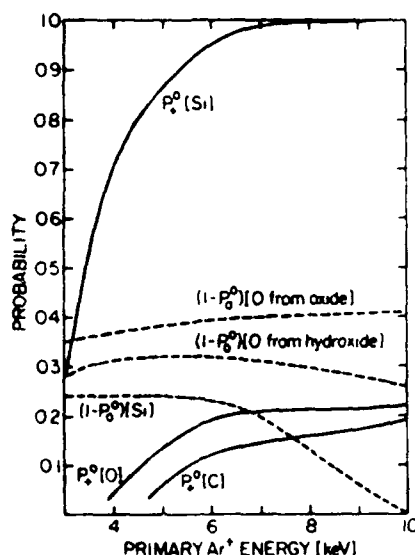


Fig. 33 Values of the probabilities of ionization in the close encounter P_0^0 and the probability that a neutral atom will capture a surface electron on its outgoing trajectory $(1 - P_0^0)$ as a function of primary ion kinetic energy. With permission from ref. [124].

ment, is determined by both P_+^0 and P_0^+ as well as the probability P_0^0 of the neutral atom leaving the surface without capturing an electron. The P_+^0 and P_0^+ values calculated above along with the experimental Y_- values can be used in this case to determine P_0^0 . The probability that a neutral atom will capture a surface electron on its outgoing trajectory is then given by $(1 - P_0^0)$. The quantity $(1 - P_0^0)$ is plotted in fig. 33 as a function of E for Si^- and O^- direct recoils. The plots show that $(1 - P_0^0)$ is high at low velocities and either decreases or remains approximately constant as velocity increases. For surface atoms in a negatively charged environment, the probability of neutralization of a negative ion in the close encounter P_+^+ becomes important (table 2) and Y_- as a function of E_0 depends on the behavior of the product $P_0^0 P_+^+$. For surface atoms in a positively charged environment, the probability of neutralization of a positive ion in the close encounter P_+^+ becomes important (table 2) and Y_+ depends on P_+^+ , P_0^+ , and P_0^0 .

5.5.4. General trends in DR ion fractions

The data presented herein show that high negative and positive ion yields are obtained for some DR species and that the behavior of these two oppositely charged species as a function of energy is distinctly different. This different energy dependence indicates that the two types of ions are produced

by distinctly different processes. These processes can be represented qualitatively according to the expressions derived (table 2) from the model.

The positive ion yields rise from a value near zero at a specific collision energy, increase with energy, and eventually reach a plateau at higher energies. This threshold-type behavior indicates that inelastic processes occurring during the close encounter, such as ionization of neutrals (P_+^0), are responsible for positive ion formation. The negative ion yields are usually high at low energy and exhibit a flat or decreasing yield with higher kinetic energy. This behavior indicates that formation of negative ions does not require the violent collisions. Their formation is largely dependent on the ability of the outgoing neutral to accept an electron from the surface. This probability is described as $(1 - P_0^0)$, where the survival probability of the neutral P_0^0 increases with increasing energy. As noted from table 2, other terms such as P_+^0 , P_0^+ , P_{++} , and P_-^+ can be involved in the Y_- function depending on the initial charge state of the surface atoms; combinations of these terms can result in unusual shapes for the Y_- yields versus energy.

5.6. Effects of chemical environment on DR ion fractions

The data show that $Y_{+,-}$ values are strongly dependent on the chemical nature of the atoms in the surface. For example, comparing Si to SiO_2 , MgO to Mg(OH)_2 , and graphite to hydrogenated graphite, the $Y_{+,-}$ values exhibit large differences. Both the chemical environment of the atoms and the different charge exchange probabilities along the outgoing trajectory can contribute to these different ion yields.

5.6.1. Influence of H on O and C DR ion fractions

The large influence of hydrogen on the O^+ and C^+ yields is particularly interesting. Both oxygen and carbon have positive electron affinities, their negative ions are stable, and their positive ions have a higher probability of being neutralized along the outgoing trajectory than the negative ions; all of these factors contribute to high Y_-/Y_+ ratios from the oxide or graphite surfaces. In the case of a OH or CH moiety, a direct collision from Ar will result in transfer of most of the momentum to the heavier O or C atom. The recoiling O and H or C and H atoms will have different velocities, leading to dissociation of the OH or CH group. It should be noted that we have never observed molecules in DR spectra, indicating that the severity of the collision results in efficient dissociation. As the XH (where X = O or C) moiety dissociates, we can consider the dissociation products of XH^- and XH (the latter produced by charge exchange with Ar^+) as shown in fig. 34. The most stable products resulting from concerted dissociation of XH^- will be $\text{XH}^- \rightarrow \text{X}^- + \text{H}$, whereas XH will yield $\text{XH} \rightarrow \text{X} + \text{H}$ and $\text{XH} \rightarrow \text{X}^- + \text{H}^+$. During dissociation of the XH moiety, the many potential energy curve crossings that

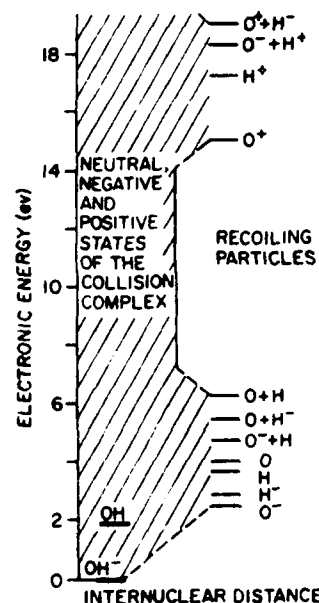


Fig. 34. Energy level diagram illustrating the ground electronic states of the OH^- , OH , and excited states of the Ar-O-H collision complex relative to states of the separated atoms, ions, and various combinations of atoms and ions. With permission from ref. [123].

result upon leaving the high density of states of the collision complex region favor production of these most stable products. For an unconcerted dissociation mechanism, X^- is also strongly favored over X^+ based on energetics. The high sensitivity of the X^+ yield to the presence of hydrogen strongly suggests that hydrogen is intimately involved in the dissociation mechanism. This large influence of hydrogen implies that there is concerted dissociation of XH^- (and XH) to yield the most stable products, i.e., X^- and H .

5.7. Scattered alkali ion fractions

The mechanism of neutralization of scattered ions near the surface is not directly applicable to alkali ions because alkali atom ionization potentials (IP) are smaller than or in the same range of the Fermi levels $|E_F|$ of metals or top of the semiconductor valence bands $|E_T|$. In other words, the lowest energy vacant level of an alkali ion $|E_i^v|$ typically lies at a higher energy than $|E_F|$ or $|E_T|$. The model would therefore predict that the probabilities of resonant and Auger neutralization of the alkali ion on the incoming and outgoing trajectory are $P_i = P_o = 0$. However, when an alkali approaches a surface, its valence level is broadened and lowered due to the image potential

induced in the surface. This can result in a partial overlap of E_i^* with the valence band of the surface, therefore, near the surface, $P_i, P_0 \neq 0$.

A model of the interactions of low energy alkali ions (< 100 eV) with metal surfaces has been developed [129-131] and successfully extended to energies in the keV range [26,132,133]. The broadening of the alkali valence level near the surface can be represented by a Lorentzian distribution [131] of width $\Gamma(s) = \hbar R(s)$, (28)

where $R(s)$ is the transition rate near the surface and is given by eq. (18).

The probability of resonant neutralization is determined by the position and width of the alkali valence level E_i^* relative to the $|E_T|$ or $|E_F|$. When the shifted and broadened E_i^* lies totally below $|E_T|$ or $|E_F|$, resonant neutralization can occur freely. If E_i^* lies above $|E_T|$ or $|E_F|$, resonance neutralization cannot occur. When there is partial overlap of E_i^* with the valence level, neutralization can occur with a probability determined by the degree of overlap. The system is adiabatic if the alkali is moving infinitesimally slowly. Under these conditions, an equilibrium is established between the charge density on the surface and on the alkali with the electrons occupying the lowest available energy levels. For real systems, the alkali has a finite velocity and this equilibrium situation cannot be maintained at all points along its trajectory. In order to treat such a system, the concept of a "freezing distance" s^* is introduced [134]. s^* is the distance beyond which the charge exchange probability becomes negligible. Equilibrium is possible only when the broadened E_i^* overlaps with the surface valence band. If a true equilibrium situation is attained along the outgoing trajectory, the final charge state of the ion bears no memory of its initial charge state or charge transfers in the close encounter [26,110,134]. The measured ion fraction of the scattered particles therefore reflects the equilibrium charge state at s^* .

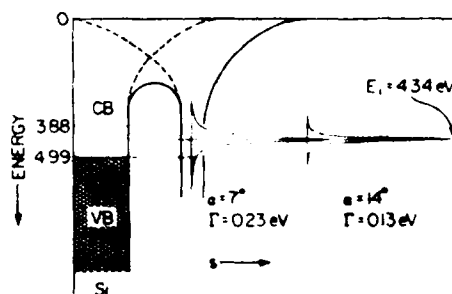


Fig. 35. Energy level diagram representing K^+ approaching a silicon surface. The discrete 4s energy level of potassium at 4.34 eV is broadened during the approach to the surface. The width of the 4s level Γ is shown for the cases of v_{\perp} corresponding to angles $\alpha \approx 7^\circ$ and 14° . The silicon valence band (VB) is hatched and the conduction band is labeled (CB). The portion of the broadened K 4s level that overlaps with the Si valence band is shaded. With permission from ref [135].

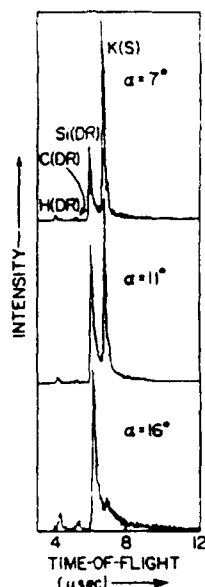


Fig. 36. Neutral TOF spectra from clean Si(100) induced by 4 keV K^+ at different incidence angles α for $\theta = 21^\circ$ along the $(01\bar{1})$ azimuth. With permission from ref. [135].

Fig. 35 shows a schematic energy level diagram for K^+ scattering from Si [135]. The K 4s level at 4.34 eV lies above $|E_T| = 4.99$ eV for Si. At large separation there can be no charge transfer between Si and K^+ . The broadening of K 4s calculated by eq. (28) is shown for two values of incidence angle α and therefore two values of perpendicular take-off velocity from the surface. Note that at $\alpha = 14^\circ$, overlap of K 4s with the valence band is negligible while at $\alpha = 7^\circ$ there is measurable overlap. Therefore, it is expected that neutralization is more significant at lower values of α . Fig. 36 shows the dependence of the neutral scattering spectra of K^+ from Si as a function of incidence angle α . As predicted, the neutral K scattering decreases from $\alpha = 7^\circ$ to $\alpha = 16^\circ$.

Algra et al. have derived an expression [26] for the equilibrium occupation $n(s)$ of the alkali valence level

$$n(s) = [\arctg 2(-E_T + E_i)/\Gamma - \arctg 2(-E_B + E_i)/\Gamma] / \pi, \quad (29)$$

where E_B and E_T are the bottom and top of the surface valence band, respectively. The calculated $n(s)$ curve as a function of exit velocity of the alkali perpendicular to the surface v_\perp is shown in fig. 37 along with experimental ion fractions for the K/Si system at scattering angles of $\theta = 21^\circ$ and 33° . For any given scattering angle Y_0 is only a function of v_\perp , as predicted. However, the difference in Y_0 as a function of θ indicates that a second

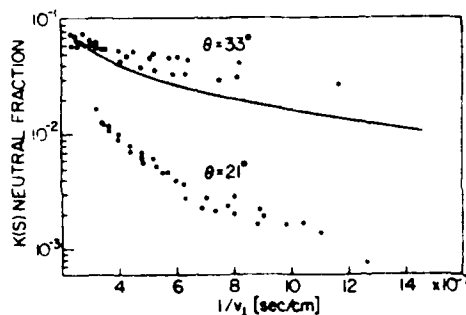


Fig. 37. Scattered potassium K(S) neutral fractions plotted as a function of the reciprocal outgoing velocity perpendicular to the surface (v_{\perp}) for two scattering angles $\theta = 21^\circ$ and 33° . The multitude of points at each θ are obtained by using several primary K^+ energies E . The curve represents the probability of occupation of the potassium 4s level ($n(s^*)$) calculated from eq. (29). With permission from ref. [135].

phenomenon, most likely neutralization in the close encounter, is important in the overall neutralization process.

5.8. Charge exchange in low energy atomic and molecular ions

Snowdon et al. [136–138] have recently reported a number of elegant experiments on charge transfer of low energy (< 1.5 keV) atomic and molecular ions upon grazing collisions with surfaces. At the low angles of incidence used in these experiments, E_{\perp} to the surface is small and in the range of chemical binding energies. The small E_{\perp} makes the assumption of distinct binary collisions between the ion and surface atoms no longer valid. In scattering of Si^+ from Cu(111), Snowdon et al. [136] observed discrete energy losses in the scattered positive and negative ion peaks. They attribute this to transient adsorption or a skipping motion of the ion along the surface. It is proposed that at the low perpendicular velocities v_{\perp} of the ion, the charge equilibrium between the ion and the surface is nearly adiabatic, i.e. the occupation of levels in the projectile approaches that corresponding to an adsorbed atom on the surface. They have developed a theoretical formalism to describe this behavior [137]. This work has been extended to polyatomic ions [138]. In O_2^+ and CO_2^+ scattering from Ag(111) production of O_2^- and CO_2^- are observed. These species have been suggested as intermediates [139] in the dissociative adsorption of CO_2 and O_2 on Ag, supporting the adiabatic approximation and also suggesting that this technique can provide a probe of intermediate states in adsorption and reaction at surfaces.

6. Reactions of energetic ions with clean surfaces

A basic objective of reactive ion beam induced interactions at surfaces has been in the application of the fundamental steps of the interactions to alteration of surface properties and in controlling surface interactions in hostile environments. Examples of the former include preparation of films that are chemically inert and corrosion resistant, surface hardening and passivation (carbides, nitrides), preparation of catalytic surfaces that are reaction specific, and tuning electronic band gaps in materials (oxides). Examples of interactions in hostile environments include plasma etching and processing of materials and development of non-equilibrium plasma phenomena.

The fundamental research that has preceded technology involves a broad spectrum of ion beam-surface interactions. For convenience, the reactions have been divided into those involving atomic ion and molecular ion beams.

6.1. Atomic ion beam interactions with surfaces

In general, measurements of ion beam interactions with clean surfaces are described in terms of "initial" sticking or reaction probabilities (P_r). This requires that the total atomic ion flux preceding measurement of P_r be kept suitably small to ensure that the measured P_r reflects true gas atom-lattice atom interactions. A typical study involves exposing a well defined target surface to a known flux of reactive ions and then using a combination of surface and gas-phase analytical tools to measure the fraction of primary ions trapped at the surface. While such an experiment can be performed with a variety of species, this section will concern itself with those species which have been studied in most detail, namely C, N, O, F and alkali atoms.

6.1.1. Reactions of low energy C^+ , N^+ , O^+ and F^+ ions

Reactions of 3–300 eV C^+ ions with Ni(111) [47], Si(100), and polycrystalline Au [140] have been studied recently. For the C^+ /Ni(111) system, experiments have been carried out both as a function of ion energy and dose. A stable carbide phase of the deposit is formed for doses of $\sim 2 \times 10^{15}$ atoms/cm² at all E ; the behavior of P_r versus E for C^+ is shown in fig. 38. P_r is highest at low E (~ 0.85) and decreases fairly rapidly at $E > 100$ eV. The behavior of P_r as a function of ion fluence for 20 eV C^+ is illustrated in fig. 39. There is no significant variation in the P_r for fluences corresponding to the surface lattice atom density; for Ni $\sim 1.86 \times 10^{15}$ atoms/cm². Continued C^+ exposure to surfaces in the range 30–800 eV results in formation of deposits that highly resemble diamond. This aspect is discussed in greater detail in section 9.

P_r data for the O^+ /Ni(111) system [47], illustrated in figs. 38 and 39, is qualitatively similar to the C^+ /Ni(111) system. However, P_r remains invariant

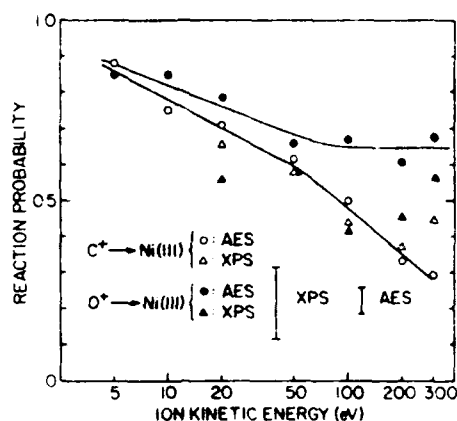


Fig. 38. Variation of reaction probability P_r for C^+ and O^+ as a function of projectile kinetic energy E monitored by both AES and XPS. The AES data points represent P_r averaged over several independent measurements. With permission from ref. [47]

even for $E > 60$ eV (fig. 38). The P_r of 20 eV O^+ as a function of O^+ fluence is plotted in fig. 39 and shows a gradual decrease in the reaction probability as the O adatom coverage increases.

Nitridation reactions have been carried out by 0–100 eV N^+ bombardment of Mo [34]. The atom capture probability or reaction cross section was found to be nearly independent of E . Fig. 40 illustrates this feature and compares nitridation efficiency on Mo using 0–100 eV N^+ and N_2^+ . The nitridation reaction involving N^+ , N_2^+/Mo is discussed in greater detail in section 7.2.

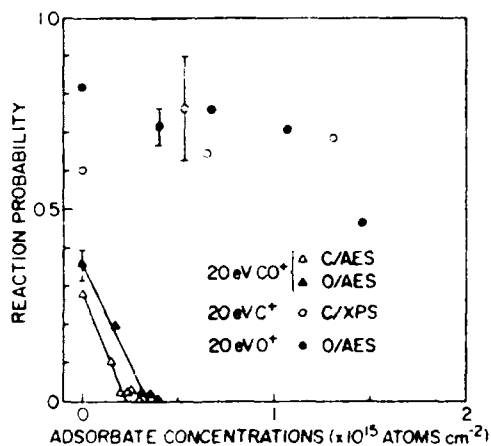


Fig. 39. Variation of reaction probability P_r for 20 eV C^+ , O^+ , and CO^+ as a function of surface coverage. With permission from ref. [47].

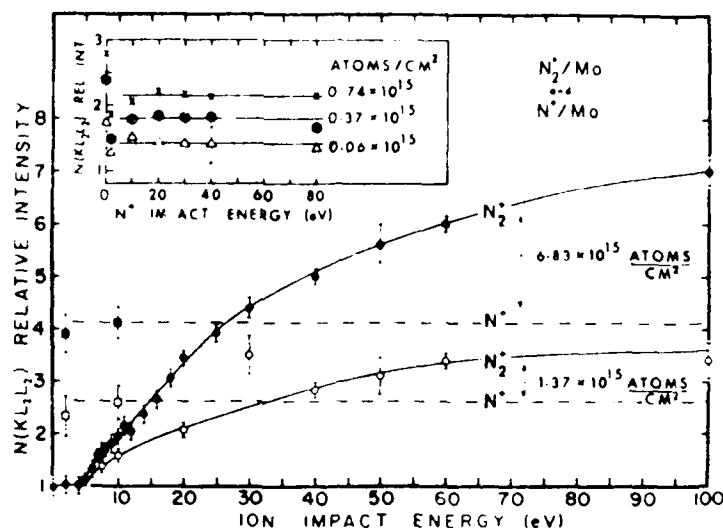


Fig. 40. Nitrogen KL_2L_2 Auger peak intensity in the surface layer of polycrystalline molybdenum as a function of impact energy for mass-selected beams of N^+ (square points, dashed curve) and N_2^+ (round points, solid curve). The inset shows similar plots for N^+ at lower doses. All curves are qualitative fits to the data points. With permission from ref. [34].

Fluorination of polybutadiene, polystyrene, and polyacetylene surfaces by means of 1 keV mass-selected beams of (i) F^+ , (ii) CF_3^+ , and a non-mass selected beam of (iii) CF_n^+ ($n = 0, 1, 2, 3$) has been studied [141] by XPS. The bonding environment of fluorine in the films was determined from the C 1s XPS chemical shifts and the fluoropolymer film thicknesses determined from XPS intensity ratios. The results showed that $-CHF-$ and/or $-CF_2-$ fluorine bonding environments, which are independent of the type of unsaturated sites in the target polymer, can be produced by selective ion bombardment. The fluoropolymer films were found to be considerably thinner than film thicknesses predicted by ion range calculations, due to electronic stopping mechanisms associated with the reactive fluorine atoms.

6.1.2. Reactions of low energy alkali atoms

The first studies of the chemical aspects of atom-surface interactions in the hyperthermal range are those of Hurkmans et al. [59,60], involving the interaction of alkali atoms with tungsten surfaces in the 1–20 eV range. Fig. 41 plots the trapping factor, P_t , for K atoms on W(110); P_t decreases from near unity for $E < 1$ eV to zero above 15 eV. This rather dramatic variation in the P_t with E is in contrast to the more gradual changes in P_t observed with C and O atomic interactions. Such differences can be understood in terms of the reaction energetics, the exoergicity of C–Ni interactions being more than three

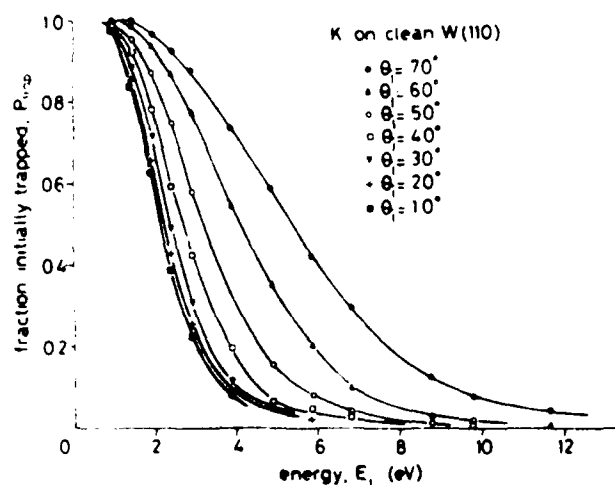
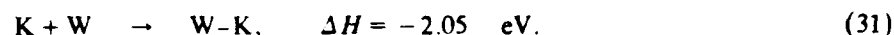
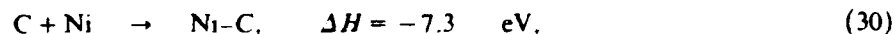


Fig. 41. Trapping probability of K atoms by W(110) as a function of incident energy for seven different angles of incidence at $T_s = 1150$ K. The angle of incidence θ_i is measured from the surface normal. With permission from ref. [60].

times larger relative to the K-W system:



P_t measurements have been carried out for the K-W system [60] as a function of the incidence angle of the impinging reactive atoms. The atom capture probability is highest at the grazing geometry and also exhibits a relatively slower decrease with particle energy at these angles. This observation can be explained in terms of the higher probability for trapping a particle in a potential well at the surface at large angles with respect to the surface normal.

The trapping phenomenon for the K/W(110) system was approximated by Los and co-workers [60] by calculating the in-plane trajectory of a projectile scattered from a diatomic surface molecule. The important feature observed was the conversion of tangential momentum to normal momentum of the projectile. Two interaction patterns were identified as a function of the incidence angle. At grazing incidence, many-body effects were dominant, whereas at near normal incidence, single particle interaction was found to contribute most to momentum transfer. The attractive interaction between the incoming atom and a surface atom was modeled by a square well potential D that is merely the experimentally measured desorption energy. This factor was added to E to give a net energy $E + D$. The Born-Mayer potential was used to model the repulsive interaction between projectile and surface. Fig. 42 plots

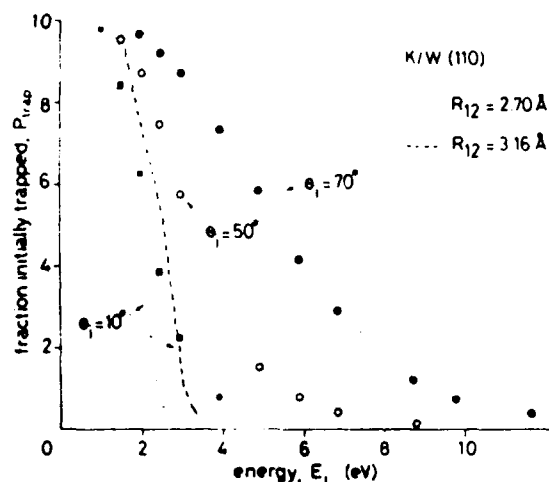


Fig. 42. Comparison of measured values of the trapping probability for K on W(110) with results of the trajectory calculations, as a function of energy for three different angles of incidence. Measurements: (■) $\theta_i = 10^\circ$; (○) $\theta_i = 50^\circ$ and (●) $\theta_i = 70^\circ$. Calculations: The corresponding curves have been calculated for two atomic distances: (---) $R_{12} = 3.16 \text{ \AA}$ and (.....) $R_{12} = 2.70 \text{ \AA}$. With permission from ref. [60].

the trapping yields predicted by trajectory calculations along with the experimental data; the agreement is satisfactory.

6.1.3. Factors affecting reaction probabilities

It is well known that for many adsorbate/metal substrate combinations, the presence of adsorbate atoms can significantly alter the reactivity of the surface towards certain reactants. Los and co-workers [60] have extended their study of 0–30 eV alkali atom interaction with W(110) by examining variations in trapping yields for oxygen covered W(110). Fig. 43 plots the trapping probability of K atoms on the oxygen covered W(110) surface for a number of angles of incidence, as a function of primary energy. By comparing this data with that for a clean W(110) surface (fig. 41), it can be seen that oxygen adsorption (0.5 ML) causes a considerable enhancement in the trapping probabilities. Such an effect has also been verified for other alkali atoms. In addition to the enhanced trapping effect, an increase in the desorption energy of the trapped particle was observed. The enhancement in the trapping probabilities was explained qualitatively in terms of mass considerations and relative efficiency of energy transfer between the different collision partners, viz. K/O and K/W.

The dissipation of energy, necessary for adsorption at surfaces is generally discussed in terms of lattice vibrational excitations. In contrast, the role of electronic excitations has been given mainly theoretical consideration [1].

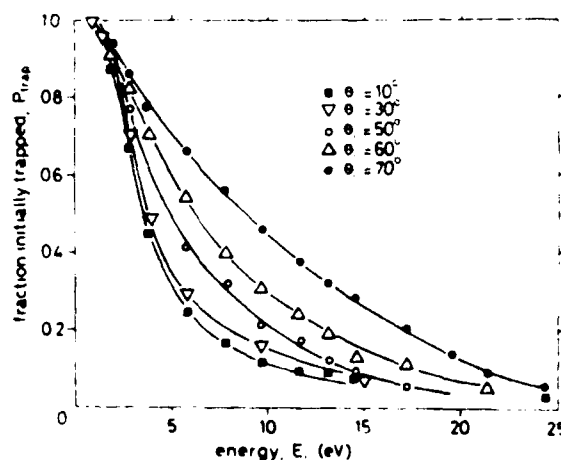


Fig. 43. Trapping probability P_{trap} of K atoms scattered by oxygen covered W(110) as a function of incident energy E_i at five different angles of incidence θ_i , $T_s = 1230$ K. With permission from ref [60].

Recently, direct measurement of the excitation of electron-hole pairs at single crystal surfaces by the scattering of ground state Xe atoms over the range ~ 2 –10 eV has been reported [142]. This represents the first experimental evidence for the nature and extent of participation of electronic excitations in hyperthermal gas-surface interactions.

In order to derive meaningful mechanistic information regarding the interaction processes, it is useful to isolate physical entrapment phenomena from chemical trapping. This can be achieved by using inert gas ion beams. When beams of rare-gas ions are employed, there is little chemical affinity between the beam particles and the lattice atoms. In such cases the majority of the ions diffuse to the surface and escape rather than remaining in the shallow potential wells of the trapping sites. By studying those ions that remain trapped in the lattice, one can gain insight into the relative physical trapping abilities of materials and the available trapping sites. An example for such a reference study is given in the following section.

6.2. Molecular ion beam interactions with surfaces

The chemisorption behavior of molecules at thermal energy, range from zero sticking probability to associative or dissociative absorption. Addition of kinetic energy to the molecule opens a number of new interaction channels. The particle translational energy can be dissipated via rotational or vibrational excitation, molecular fragmentation and subsequent chemical reaction at the target surface.

6.2.1. Reactions of low energy homonuclear diatomic ions

Winters and co-workers have measured the relative fractions of incident ions dissociatively backscattered or captured versus those molecularly backscattered for N_2^+/Mo and other systems [143]. In subsequent studies [51,144], P_r and saturation coverages of nitrogen for N_2^+/W at several impact energies were reported, as also the energy transfer from the gas-phase molecule to the W lattice [145].

The oxidation of lead due to 44 eV O_2^+ bombardment of Pb to high doses was shown [146] to produce an oxide layer ~ 200 Å thick due to a diffusion effect. A study of D_2^+ bombardment of Mo [147] showed a high P_r (> 0.8) at low doses, but also an accompanying low thermal stability (at $T > 320$ K) of the deuteride. Cooks and co-workers [148] have studied the reactions of various sulfur containing molecular ions with lead and found various chemical states of the reacted lead and sulfur depending on the parent ion type and energy.

Rabalais and co-workers have spectroscopically characterized reaction products on surfaces resulting from the interaction of 500 eV N_2^+ beams with surfaces of a metal M, and its oxides MO and MO_2 [149]. For $M = \text{Si, Ge}$ the N_2^+ ions were found to undergo charge exchange and dissociation at the target surface to form hot N atoms, producing corresponding nitrides. No nitrates or nitrite formation was observable from XPS measurements. With tin and its oxides, reaction was barely detectable, while no reaction was observed for $M = \text{Pb}$, in accord with known instabilities of such nitrides. Similar N_2^+ exposure studies have also been performed over the range 0.3–4.0 keV on Al [150].

Ion beam nitridation of the first row transition metals (Ti–Co) has been carried out over the range 0.2–3.0 keV [149] and the metal 2p chemical shifts in the XPS for the nitrated samples found to decrease to the right across the first transition row, consistent with the decreasing enthalpy of formation and stability of the nitrides. Isotopic labeling experiments carried out by 1 keV bombardment of V with $^{14}\text{N}_2/^{15}\text{N}_2$ mixtures followed by TDS measurements showed that there is complete isotopic mixing in the metal nitride, implying complete dissociation of the parent molecule in the collision at the surface.

The nitridation reactions have also been studied under more controlled conditions. 0–50 eV mass-selected N_2^+ beams have been used to induce nitride film formation on Al, Cu, Mo, Ni and Ag [33]. The efficiency of nitridation, monitored by KL_2L_2 nitrogen AES signal intensity, exhibits a large E dependence below ~ 30 eV as shown in fig. 44. The threshold impact energy for nitridation varies for the different metals; it is nominally zero for Al and Ni, ~ 4 eV for Mo, > 0 for Cu, and does not occur at all at any energy below 200 eV for Ag. The difference in the ion dose required to produce similar nitride signals on various metals suggests that the surface electronic structure plays an important role in the reaction probabilities. Another feature of the

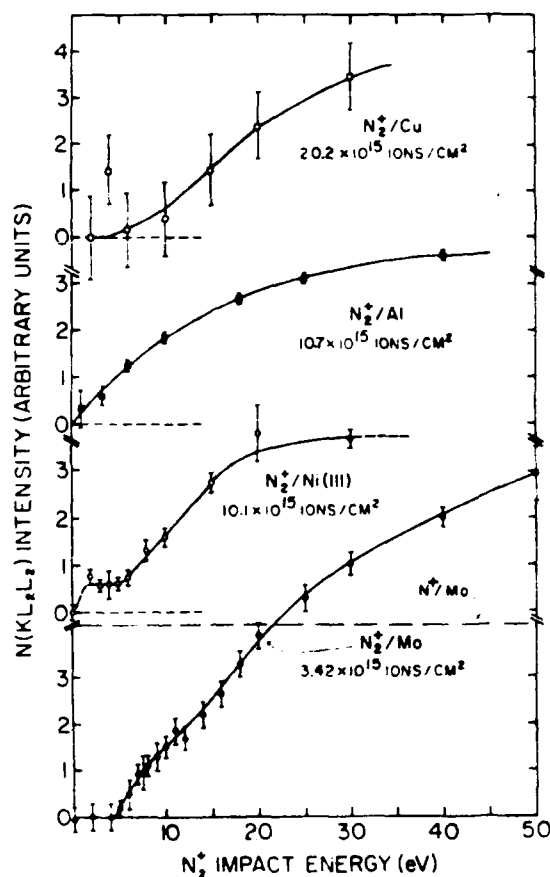


Fig. 44. $N(KL_2L_2)$ Auger peak intensity in the surface layer of Cu, Al, Ni, and Mo as a function of impact energy for mass-selected beams of N_2^+ and N^+ for Mo (from ref. [34]). The data for Cu has very large error estimates due to the weak $N(KL_2L_2)$ signals from the small amount of nitride formed. With permission from ref. [33].

nitridation reactions is that plots of nitride intensity versus E exhibit structure or different shapes in the low E range (fig. 44).

N^+ and N_2^+ interactions with polycrystalline Mo have been studied in detail [34]. Nitridation of Mo by 0–100 eV mass-selected beams of N_2^+ and N^+ produces a thin film of the nitride on the surface. The relative reaction probabilities for N^+ and N_2^+ have been investigated (fig. 40). Exposures of 1.37×10^{15} and 6.83×10^{15} atoms/cm² are shown for both ions. The reaction probability is nearly energy independent in this energy range for N^+ and is higher than the probability for N_2^+ , for $E < 30$ eV. The nitridation by N_2^+ bombardment does not occur for $E < 4$ eV due to the necessity for collision

induced dissociation of the N_2 molecule. The reaction probability for the molecular ion surpasses that for N^+ at $E \approx 30$ eV and reaches a plateau at ~ 100 eV.

6.2.2. Chemical effects in low energy ion beam studies

An interesting extension to the nitridation studies is the study of the reactions of 30–500 eV N_2^+ and NO^+ beams with surfaces of carbonaceous materials, where a range of chemical reactivities can be probed by using graphite, diamond, Teflon and graphite monofluoride as the primary targets [151]. For NO^+ , reaction of hot N and O atoms produced in the collision step with graphite produced two products, a cyanide or oxide type compound and interstitial N or O atoms between the layers of rings or at defect sites.

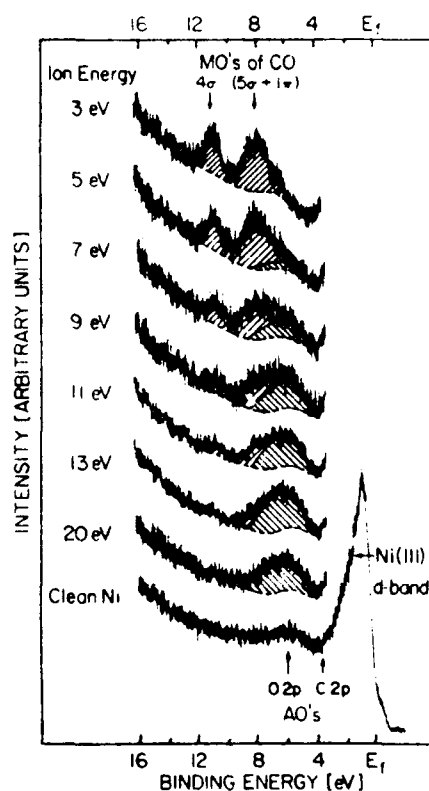


Fig. 45. HeII photoelectron spectra of clean Ni(111) and CO^+ bombarded Ni(111). A CO^+ dose of 1.0×10^{15} ions cm^{-2} was used at kinetic energies of 3, 5, 7, 9, 11, 13, and 20 eV. The two peaks at 8.1 and 10.9 eV correspond to ionization of the $(5\sigma+1\pi)$ and 4σ MO's, respectively, of molecular CO on the surface. The peak at ~ 6 eV corresponds to ionization of the 2p AO of the oxide. With permission from ref. [47].

Reactions of N_2^+ with the other carbonaceous materials produced only a cyanide-type compound. Ion kinetic energy in the range 30–3000 eV served only to drive the ions deeper into the target and had little influence on the chemical alteration itself.

It was mentioned previously that comparison of inert gas ion and active ion interactions allows separation of chemical trapping and physical trapping effects. Such studies have been carried out using 30–3000 eV Ar^+ and Xe^+ interactions with carbonaceous materials [152]. Implanted rare gases from a 500 eV beam in doses of $\sim 1.5 \times 10^{12}$ A/cm² could be detected only in graphite and graphite monofluoride, the binding energies of the rare-gas atoms indicating entrapment as neutral atoms within the lattice. Reduced carbon species were formed in both Teflon and graphite monofluoride.

More recently, some interesting chemical dynamics measurements have been carried out by reacting 1–300 eV CO^+ with Ni(111) [46,47]. CO , in contrast to N_2 , chemisorbs associatively on Ni(111) at room temperature. Fig. 45 shows the evolution of UPS spectra for Ni(111) surfaces bombarded by CO^+ beams of different E , but same total fluence. For $E < 7$ eV, the dominant process is addition of molecular CO on the surface. With increasing E , dissociative addition of CO occurs, with the formation of individual carbide and oxide bonds to the surface Ni atoms. Fig. 46 plots the corresponding variation in $P_r(CO^+/Ni(111))$. The CO dissociation function, although not readily apparent from fig. 46 because of the logarithmic E scale, increases almost linearly with E in the range 3–20 eV. A linear least-squares fit to the data provided a threshold for CO bond rupture of ~ 2.7 eV. This value is considerably lower than the bond dissociation energy of ground state CO (11.16 eV), suggesting that a significant fraction of the incident CO^+ flux is

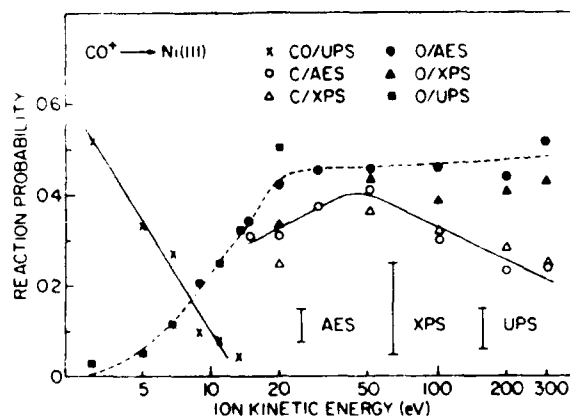


Fig. 46. Variation of reaction probability P_r for CO^+ as a function of projectile kinetic energy E monitored by both AES and XPS. With permission from ref. [47].

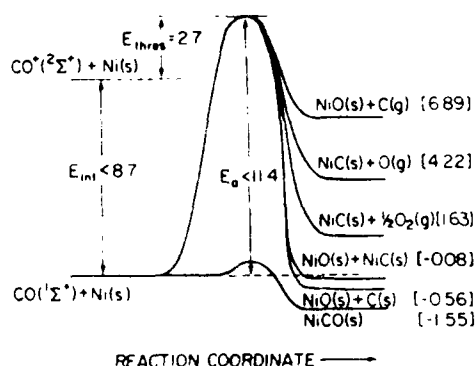


Fig. 47. Simplified potential energy diagram for the reaction of incoming CO^+ with a Ni(111) surface. Ground-state neutral CO is shown as the zero-energy reference point. Various combinations of the simplest possible reaction products, along with their reaction enthalpies relative to $\text{Ni(s)} + \text{CO(g)}$, are shown on the right-hand side. All energies are in eV. With permission from ref. [46].

neutralized into excited states (section 2.2) which would have lower dissociation energies. The activation barrier is also a strong function of the orientation of the molecular axis with respect to the surface plane during collision. The 2.7 eV energy threshold is therefore considered as an averaged factor over an ensemble of electronic states and molecular orientations. Fig. 47 shows a simplified energy diagram for the reaction of CO^+ with Ni(111). Ground-state neutral CO is chosen as the zero-energy reference point. Various combinations of the simplest possible reaction products, along with their relative reaction enthalpies, are shown. The fact that P_r for $\text{CO}^+/\text{Ni(111)}$ is a significant number for E up to 30 eV indicates an activation barrier whose height ranges from 2.7 to 30 eV. Such a wide distribution of barrier heights is a consequence of the diverse impact geometries and electronic states accessible in molecular ion interactions with surfaces.

6.2.3. Low energy molecular ion reaction dynamics

The energetics for molecular CO addition and desorption can be qualitatively expressed in terms of a simplified potential energy diagram shown in fig. 48. For thermal energy CO, translational energy is easily dissipated to rotational or vibrational motions upon impact on the surface leading to trapping in the upper rovibronic levels of the CO/Ni potential well (path A). When E is of the order of a few eV, the excess energy remaining after collision can be significant compared to the CO/Ni potential well depth, favoring CO desorption over chemisorption (path B). This explains the fact that $P_r < 1$ at low E . CO dissociation does not occur until sufficient energy is available for surmounting the reaction activation barrier (path C). Once the barrier is overcome, it can be seen from fig. 48 that the resulting carbon and oxygen

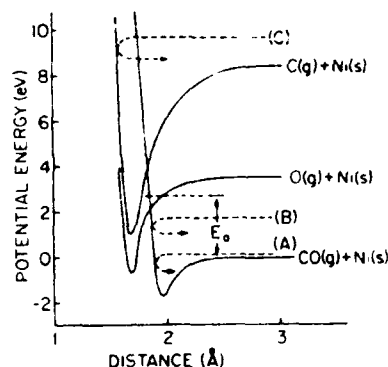


Fig. 48. Simplified potential energy diagrams for Ni-CO, NiC, and NiO as a function of the Ni-X coordinate. Ground state CO(g), C(s), O₂(g), and Ni(s) are chosen as the zero energy reference point. The curves are fixed at the equilibrium Ni-X distances and bond energies, although the shapes are drawn qualitatively. The observed threshold for CO dissociation at 2.7 eV is indicated as E_a . The three different paths represent (A) molecular chemisorption of thermal CO, (B) scattering of hyperthermal CO, and (C) dissociation of high energy CO. With permission from ref. [47].

atoms are trapped in their respective potential wells in Ni-C and Ni-O bond formation.

A simple quantum mechanical model has been developed [33] to describe chemical reactions of low energy ($E \leq 30$ eV) beams of diatomic homonuclear cations X_2^+ with metal surfaces to produce binary compounds $M_\alpha X_\beta$. The overall reaction is simulated by four elementary steps: (1) neutralization of the incoming ion (section 2.2), (2) impact dissociation of X_2^+ , (3) de-excitation and thermalization of X, and (4) chemical reaction between M and X. The neutralization process is treated by a simplified quantum mechanical procedure involving resonance and Auger neutralization probabilities and Franck-Condon and Honl-London factors for X_2^+ transitions to the ground and excited states and rovibronic levels of X_2 . The probability of dissociation from a given rovibronic level is modeled through use of a function developed for the decomposition of gas-phase polyatomic molecules. Model calculations using free electron and modified free electron bands for the metal and various manifolds of electronic and vibronic states for X_2^+ and X_2 are presented in that work, to illustrate the sensitivity of the model to individual steps in the mechanism.

7. Beam-surface reaction kinetics

7.1. Kinetics model

In order to model the surface concentration $N(t)$ (atoms cm⁻²) of reacted beam atoms as a function of exposure time, it is necessary to define the

maximum number of surface sites per unit area N_{\max} that are available for reaction. N_{\max} is primarily dependent upon the mean ion penetration depth and hence the ion impact energy. The model assumes that all of the N_{\max} sites are within the sampling depth of the analytical technique employed for measurement and, hence it is applicable to depth-integrated elemental analyses. Employing a rudimentary concept of depth, consider that there are two guest atom populations in the host lattice, one occupying near-surface sites with concentration $N_1 = N_1(t)$ and another occupying sub-surface sites with concentration $N_2 = N_2(t)$. Under an active ion flux density Φ (atoms $\text{cm}^{-2} \text{s}^{-1}$), atoms are captured at a rate

$$dN_1/dt = \sigma_{1c}\Phi(N_{1,\max} - N_1), \quad (32)$$

where σ_{1c} is the reaction-capture cross-section (cm^2) for the outer sites. A similar expression can be written for dN_2/dt using σ_{2c} and $N_{2,\max}$. Both σ_{1c} and σ_{2c} are averages over various binding sites available on polycrystalline surfaces. The reacted atoms are sputtered by the incoming atoms at rates $dN_1/dt = -\sigma_{1s}\Phi N_1$ and $dN_2/dt = -\sigma_{2s}\Phi N_2$ with sputter cross-sections $\sigma_{2s} = 0$, but it is carried forward for symmetry and because its omission does not significantly simplify the solution. Also note that σ_{1c} and σ_{2c} include all product loss mechanisms including the reverse reaction to liberate N_2 gas. The impinging ions may cause transport of some of the N_1 population to N_2 at the rates $dN_1/dt = -\sigma_{12}\Phi N_1$ and $dN_2/dt = \sigma_{12}\Phi N_1$, with σ_{12} being the beam-induced $N_1 \rightarrow N_2$ transport cross-section. Transport in the $N_2 \rightarrow N_1$ direction also may occur by similar mechanisms but is probably dominated by host lattice sputtering which uncovers N_2 atoms so that they become part of N_1 . The rates $dN_2/dt = -\sigma_{21}\Phi N_2$ and $dN_1/dt = \sigma_{21}\Phi N_2$ have been derived elsewhere [153] under the assumption $\sigma_{12} \approx \sigma_{21}$, the lattice sputtering cross-section. Collecting the capture, sputtering, and transport rates for each population, the overall rates are

$$dN_1/dt = \sigma_{1c}\Phi(N_{1,\max} - N_1) - \sigma_{1s}\Phi N_1 + \sigma_{21}\Phi N_2 - \sigma_{12}\Phi N_1, \quad (33)$$

$$dN_2/dt = \sigma_{2c}\Phi(N_{2,\max} - N_2) - \sigma_{2s}\Phi N_2 - \sigma_{21}\Phi N_2 + \sigma_{12}\Phi N_1, \quad (34)$$

Impose the following definitions:

$$a_{10} = \sigma_{1c}\Phi N_{1,\max}, \quad (35a)$$

$$a_{11} = -(\sigma_{1c} + \sigma_{1s} + \sigma_{12})\Phi, \quad (35b)$$

$$a_{12} = \sigma_{21}\Phi, \quad (35c)$$

$$a_{20} = \sigma_{2c}\Phi N_{2,\max}, \quad (35d)$$

$$a_{21} = \sigma_{12}\Phi, \quad (35e)$$

$$a_{22} = -(\sigma_{2c} + \sigma_{2s} + \sigma_{21})\Phi. \quad (35f)$$

Then simplify eqs. (33) and (34) to

$$dN_1/dt = a_{11}N_1 + a_{12}N_2 + a_{10}, \quad (36)$$

$$dN_2/dt = a_{21}N_1 + a_{22}N_2 + a_{20}. \quad (37)$$

These coupled equations can be integrated, yielding the solution $N(t) = N_1 + N_2$. Letting the initial surface concentrations be N_{10} and N_{20} , the solution can be expressed as:

$$N(t) = A_1 \exp(\alpha_1 t) + A_2 \exp(\alpha_2 t) + B, \quad (38)$$

where

$$\alpha_{1,2} = \frac{1}{2}[(a_{11} + a_{22})] \pm \frac{1}{2}[(a_{11} - a_{22})^2 + 4a_{12}a_{21}]^{1/2}, \quad (39)$$

and

$$A_{1,2} = [(a_{1,2} - a_{22} + a_{21})/a_{21}] C_{1,2}, \quad (40)$$

with

$$C_{1,2} = \pm (\alpha_1 - \alpha_2)^{-1} [a_{21}N_{10} - (\alpha_{2,1} - a_{22})N_{20} + \alpha_{2,1}F], \quad (41)$$

and with

$$F = (a_{21}a_{10} - a_{11}a_{20})(a_{11}a_{22} - a_{21}a_{12})^{-1}. \quad (42)$$

Finally,

$$B = [a_{10}(a_{21} - a_{22}) + a_{20}(a_{12} - a_{11})](a_{11}a_{22} - a_{21}a_{12})^{-1}. \quad (43)$$

Eq. (38) is a bi-exponential "growth" from areal concentration $N = A_1 + A_2 + B$ at $t = 0$ to a steady state $N = B$ at $t = \infty$. Growth is en-quoted because $A_{1,2}$ can be positive or negative quantities, corresponding respectively, to the case in which sputtering dominates and to the case in which beam atom capture dominates. Simplifications occurring in some physical cases include negligible $N_1 \rightarrow N_2$ transport ($\sigma_{12} \approx 0$) or negligible $N_2 \rightarrow N_1$ transport ($\sigma_{21} = 0$), either of which lead to simplification of eq. (39) for $\alpha_{1,2}$ (the curvature constants of the exponentials), i.e. the apparent cross-sections derived from experiment. Setting $\sigma_{12} = \sigma_{21} = 0$ decouples eqs. (36) and (37) to give

$$N_i(t) = N_{i,\infty} + (N_{i0} - N_{i,\infty}) \exp[-(\sigma_{ie} + \sigma_{is})\phi t], \quad i = 1, 2, \quad (44)$$

where, generically,

$$N_{i,\infty} = N(t = \infty) = N_{\max}\sigma_e/(\sigma_e + \sigma_s). \quad (45)$$

Allowance for the existence of two captured beam atom populations is intended as the simplest implementation of the concept of depth in a model that otherwise refers only to concentrations as atoms per unit area, integrated over depth. By this structuring, expressions can be obtained (in the no-capture case [153]) for surface concentrations versus fluence that have the same functional form as Sigmund et al.'s [154] expressions (their eqs. (32) and (33)).

Of course, the detailed meaning of those expressions differs from these in that they use a relocation cross-section [155] of an isotropic form (eq. (27) of ref. [154]) while these use the $\sigma_{12} \leftrightarrow \sigma_{21}$ coupling to allow a simple kind of inward/outward transport anisotropy. However, these do not consider explicitly the relocation of the host matrix atoms as do Sigmund et al. In general, that model is more rigorous than this one in that it is depth-explicit rather than depth-averaged, but it was intended for higher ion impact energies than employed here.

7.2. Reaction of N_2^+ and N^+ with molybdenum

Gaseous N_2 does not react with the passivated Mo surface used in this study at room temperature. The beam-surface reaction was driven by energy, both potential (ionic) and kinetic, supplied by the accelerated ion beam. The reaction mechanism [33,34] includes neutralization of the ion followed by collision-induced dissociation of the neutral N_2 with subsequent thermalization and chemical bonding of the individual atoms. Of course, either the molecule or its fragments may backscatter and hence not react, and product loss occurs through self-sputtering and reverse reaction to form N_2 gas. Ion neutralization

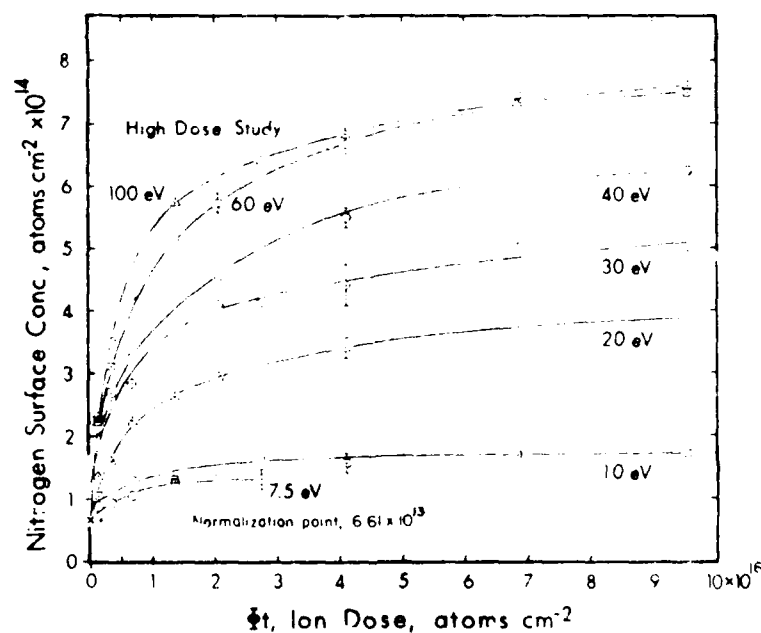


Fig. 49. Nitrogen surface concentration versus N_2^+ dose for 1–100 eV N_2^+ bombardment of Mo. With permission from ref. [32].

controls the bond strength of the neutral N_2 via known processes [33], but the collisional dissociation of the neutral, as well as the penetration, stopping and bonding of the beam atoms, and the corresponding motions of the host matrix atoms to accommodate this, are poorly understood. Experiments to directly probe these processes have not yet been attempted, and computational approaches are difficult because of the strong coupling of electronic and nuclear motions in these events.

Fig. 49 shows the surface nitrogen uptake for N_2^+ impact on Mo. There are two distinct nitrogen uptake regimes. The first is a fast initial uptake, that is strongly developed for $E > 10$ eV. The second, slower uptake is encountered at doses higher than $(3-5) \times 10^{16}$ atoms/cm². Wirz et al. [156] have described a third uptake regime associated with growth of bulk nitride, but this occurs at higher temperatures and doses, not encountered in the former work. The concentration versus dose plots of fig. 49 reach a plateau at high doses as a steady state is achieved with a fast capture/self-sputter competition.

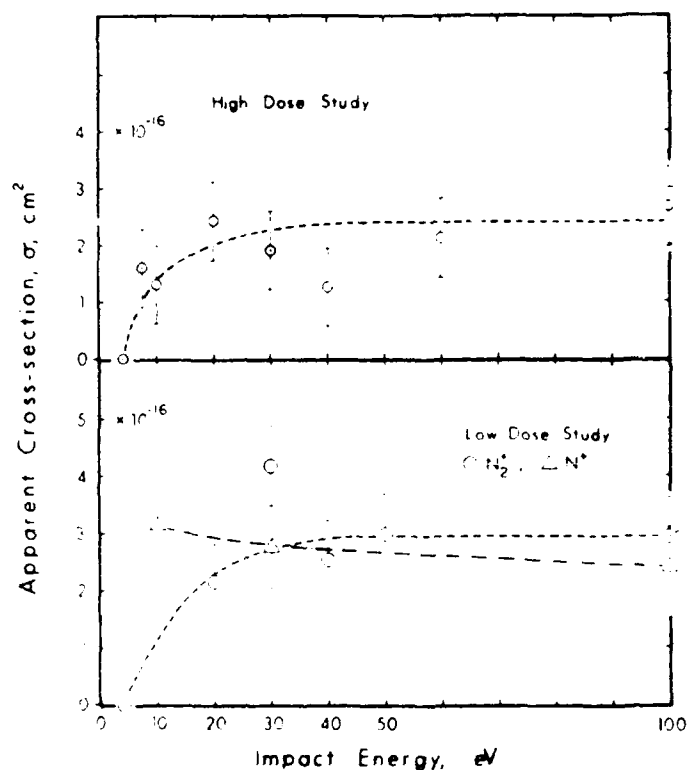


Fig. 50. Cross sections obtained by fitting the kinetics model to the concentration versus dose curves are shown for the high dose study of fig. 49. With permission from ref. [32].

7.3. Application of kinetics model to N_2^+ and N^+ reactions with Mo

The major result of the kinetics investigation is that the concentration versus dose curves can be fitted by a double-exponential rate law, i.e., one that is the sum of two single-exponential rate laws of the algebraic form of eq. (44). This is in contrast to previous studies, albeit on other ion/surface combinations [157-159], in which a single-exponential rate law sufficed. From the results of analysis within a double-exponential rate law, reaction cross-section (σ) and extent of reaction (N) values can be obtained for different E . Reaction cross-sections obtained by fitting the kinetics model to the concentration plot of fig. 49 are shown in fig. 50. The cross-sections are remarkably independent of energy above ~ 30 eV for N_2^+ and at all energies for N^+ . The rise from the assumed zero value at 4 eV threshold for N_2^+ to the plateau around 30 eV is due to the increased efficiency of collisional dissociation with impact energy.

8. Desorption induced by energetic particle bombardment

A general overview of desorption processes occurring under energetic particle bombardment has been given in section 2.4. Experiments and model computations designed to shed light on "physical" versus "chemical" desorption processes form the focus of this section. The surface under consideration can be that of a clean metal or semiconductor, an eutectic or any multiphase alloy, an ordered adsorbate (over) layer on a single crystal or other possibilities. In order to keep the discussion tractable the focus will be on sputtering of adsorbate atoms from metal substrates. A number of excellent reviews have appeared recently [160-162] that discuss the other aspects of the desorption or sputtering problem.

8.1. Physical sputtering effects of ion-surface interactions

When energetic particles impact on a surface, transfer of energy to adsorbate and lattice atoms can result in a number of secondary effects: (1) adsorbate and/or lattice atoms can be ejected from the surface by a direct knock-off, (2) the primary ion can impact an adsorbate atom after reflection from a lattice atom and eject the former, and (3) sputtered lattice atoms can remove adsorbate atoms during their outward movement at the surface. Such processes have been grouped together as physically induced desorption. To eliminate any complications arising from use of reactive ions (section 8.3), most of the work on these momentum transfer processes has involved the use of inert gas ions.

Sputtering of N_2 chemisorbed on W by inert gas bombardment has been

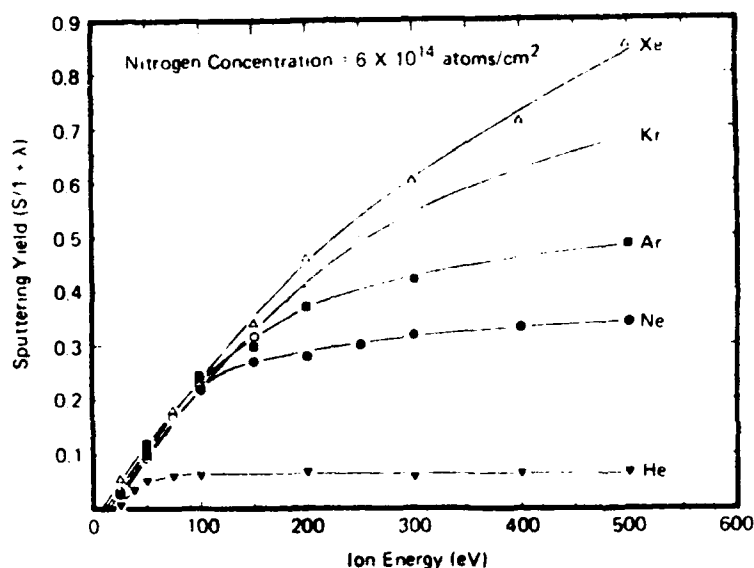


Fig. 51. Sputtering yield versus ion energy for inert gas sputtering of nitrogen adsorbed on W. λ is the secondary electron coefficient. With permission from ref. [163].

reported [52,163]. Fig. 51 shows the sputtering yield for nitrogen chemisorbed on W, using different inert gas ions at various energies. If the desorption proceeded with formation of molecular nitrogen, a desorption rate proportional to the square of the surface coverage would be expected. The desorption yield is coverage independent at low surface concentrations suggesting desorption of the nitrogen as atoms. The yield is found to increase with E and the mass of the primary ion and shows some interesting features. There is an apparent energy threshold for removal of nitrogen for all the projectile ions investigated, however, the yields for nitrogen are large despite the high binding energy of N to W. This latter observation is consistent with preferential ejection of lighter elements in the sputtering of a multicomponent system or the "mass-effect" [161]. The behavior was explained in terms of direct knock-off and/or reflected primary ion impact, steps 1 and 2 from above.

Molybdenum nitride films formed by 100 eV N_2^+ bombardment to saturation of polycrystalline Mo have been sputtered to high fluences by normally incident 100 eV Ar^+ and He^+ and 15 eV Ne^+ [153]. The choice of sputter beam parameters was based on the fact that removal of nitrogen was by momentum transfer: (1) 100 eV Ar^+ should sputter both N and Mo efficiently, (2) 100 eV He^+ should sputter N preferentially, and (3) 15 eV Ne^+ represents a sputter threshold case and should only remove accessible nitrogen. The nitrogen AES signal was found to decay exponentially as shown in fig. 52, to

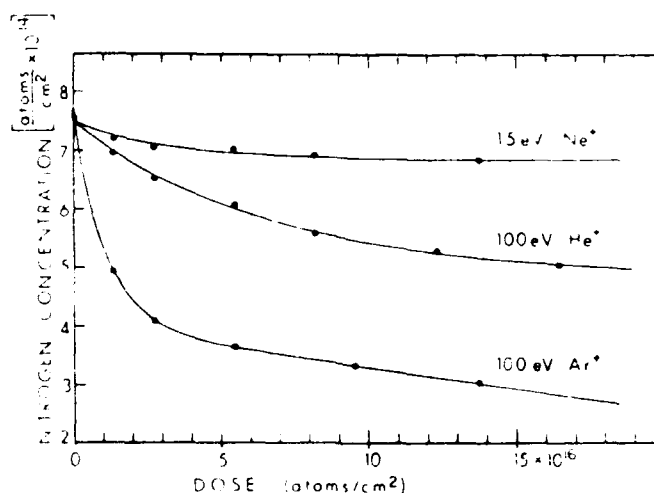


Fig. 52. Nitride surface concentration versus noble gas ion dose for 15 eV Ne^+ , 100 eV He^+ and 100 eV Ar^+ sputtering of molybdenum nitride layers formed by 100 eV N_2^+ bombardment of Mo. With permission from ref. [153].

below sputtering levels for the 15 eV Ne^+ and 100 eV He^+ cases and bi-exponentially to near bulk contamination levels for the 100 eV Ar^+ case. The degree of nitrogen desorption for the three cases is in agreement with a momentum transfer type mechanism for the sputtering. A two-layer adaptation of the standard model for adsorbate monolayer sputtering was used to model the kinetics.

Taglauer et al. [164] have reported studies of the desorption of S from Ni surfaces with inert gas ions of energy in the 200–1600 eV range. The experimental results were compared to calculations by Winters and Sigmund and with numerical model calculations. Agreement was found in the dependence of the desorption cross-section (σ_d) on the basic parameters and the absolute yields agreed within an order of magnitude.

Ion impact desorption of oxygen (≤ 1 monolayer) on Ni has been studied by the same authors [165] by He^+ ion scattering. Desorption cross-sections for non-normal incidence of Ne^+ and He^+ ions with E in the 500–1600 eV range have been measured and compared to those predicted by model calculations in order to understand the influence of various parameters. Calculations and experiments show the same dependence of σ_d on E , i.e. σ_d increases with E in the given range, for Ne^+ ions and that there is a slight decrease with increasing E for He^+ ions. This has been explained in terms of the effective contribution of sputtered Ni atoms to O desorption.

Sputtering of carbon from thin films deposited on metal substrates using Ne^+ ions at E as low as 1000 eV has been reported [166]. The sputtering yield

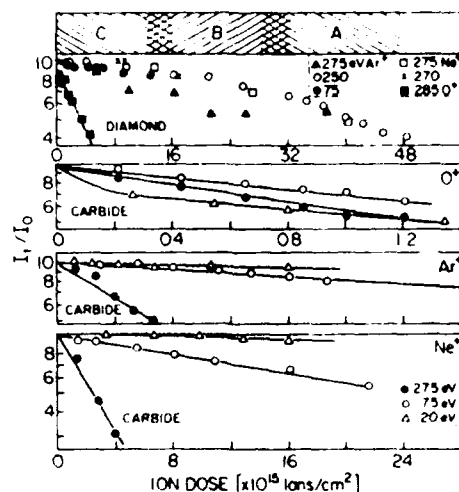


Fig. 53. Plots of $\ln I_t/I_0$ versus ion dose for sputtering of carbide and diamond films on Ni(111) by 20–300 eV O^+ , Ne^+ , and Ar^+ . The hatched areas drawn parallel to the dose scale labeled C, B, and A for the diamond film indicates the dose regions in which the C KLL line shapes are those of figs. 68 (right) (c) and (d), (b), and (a), respectively. Note the use of different dose scales for different films. With permission from ref. [50]

was found to increase fairly rapidly with ion energy. Such measurements for carbon have been extended to very low energies and under well-controlled exposure conditions [50]. Fig. 53 plots the decay in the carbon KLL AES intensity for 20–300 eV Ne^+ , Ar^+ , and O^+ sputtering of a carbide overlayer and a diamond film on Ni(111). The efficiency of carbon removal increases with E for the inert gas ions and is reflected in the corresponding sputtering cross-sections listed in table 3.

Table 3

Sputtering cross-sections for carbide and diamond film surfaces on Ni(111) using 20, 75, and 275 eV O^+ , Ne^+ , and Ar^+ primary ions (from ref. [50])

Target	Bombarding ion	Sputtering cross-sections (\AA^2)		
		20 eV	75 eV	275 eV
Carbide	O^+	6.3	3.4	5.9
	Ne^+	0.05	0.27	3
	Ar^+	0.05	0.12	1.2
Diamond	O^+	1.9		
	Ne^+	0.05		
	Ar^+	0.05		

8.2. Electronic effects and model calculations

Physical sputtering of the $p(2 \times 2)$ chemisorbed oxide phase on Ni(111) by bombardment with 5–200 eV Ne^+ at normal incidence to the surface has been investigated by a combination of techniques [167]. Decreases in surface oxygen as a function of Ne^+ ion dose were monitored by AES and TOF-DR using a pulsed grazing incidence 3 keV Ar^+ beam (fig. 54). Oxygen removal has been observed down to 20 eV and σ_d is $\sim 7 \text{ \AA}^2$ (the corresponding sputtering yield, $S \approx 0.43$) at $E > 150$ eV. The desorption of O for $E \leq 120$ eV is postulated to be mainly by direct knock-off, while at the higher energies removal is mainly by sputtered Ni atoms moving outward through the surface region. The structure in the experimental σ_d versus Ne^+ E data, in the form of local maxima and minima, cannot be explained on the basis of a binary collision model of sputtering (momentum transfer), where a smooth dependence of σ_d with E would be expected. Electronic sputtering has been suggested to be the origin of the structure, and the actual sputtering mechanism for the Ne^+/NiO system is a composite of momentum transfer and electronic sputtering. Electronic sputtering takes place as follows: When the incoming trajectory brings it near an oxygen atom, Auger neutralization of Ne^+ is possible by electrons tunneling from the oxygen valence band. The process involves an O 2p electron filling the Ne^+ hole, while another O 2p electron is promoted into either the conduction band or vacuum continuum of states. The process leaves the oxygen atom with two holes in its valence band, consequently, the originally attractive Madelung potentials become repulsive, and desorption occurs. Similar mechanisms have been proposed to interpret low energy ion induced desorption of F^+ from LiF samples [168]. A second possible electronic

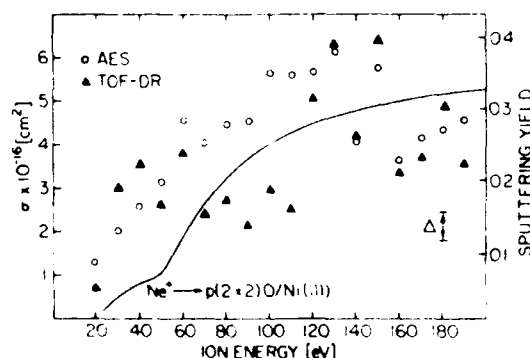


Fig. 54. Sputtering cross sections and yields for 5–200 eV Ne^+ sputtering of oxygen from the $p(2 \times 2)\text{O}/\text{Ni}(111)$ surface. The solid line represents sputtering yield S calculated from the Monte Carlo simulation. Δ represents the typical uncertainty in the experimental points. With permission from ref. [167]

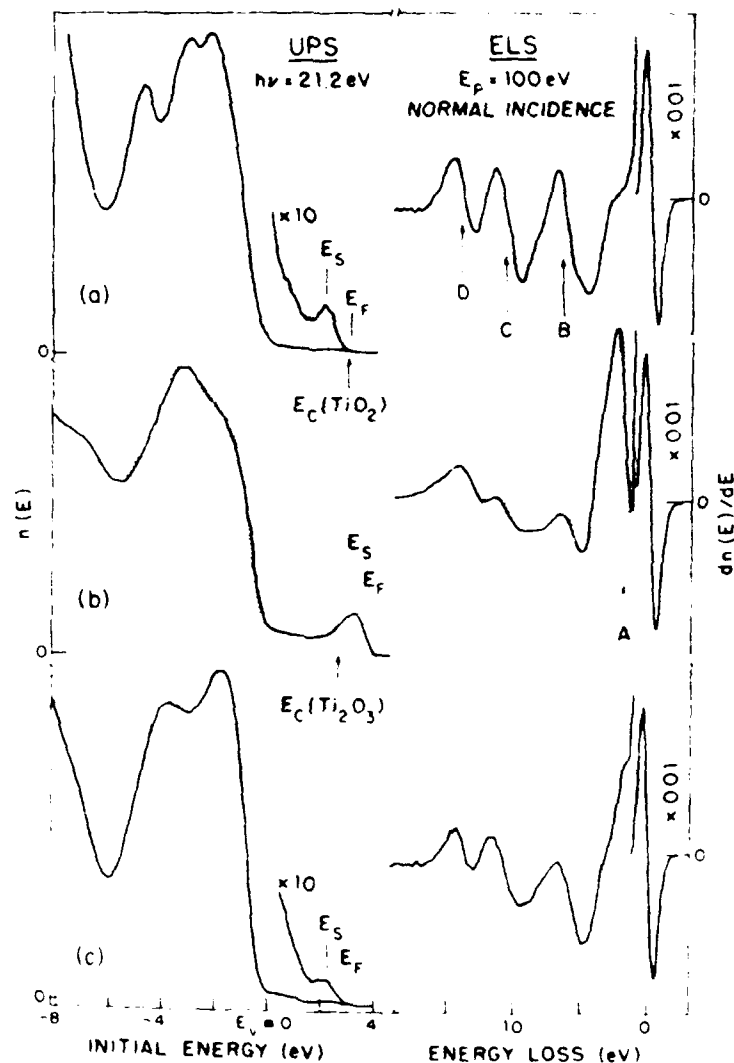


Fig. 55. UPS (HeI) and ELS (100 eV) spectra for (a) annealed (110) TiO_2 , (b) surface of (a) bombarded by 500 eV Ar^+ (solid lines) and for vacuum fractured Ti_2O_3 (dotted lines), and (c) surface of (b) exposed to 10^8 L of O_2 . With permission from ref. [169]

sputtering route involving merging of Ne and O AO's into MO's of a quasi-diatomic molecule, resulting in electron transfer processes, has also been suggested.

Some interesting electronic effects have been observed in low E ion-surface interactions, especially with oxide and halide surfaces. Fig. 55 shows the

effects of Ar^+ bombardment of crystalline TiO_2 [169]. Ar^+ bombardment initially amorphized the surface (LEED pattern disappeared) without significant removal of oxygen. Additionally an extrinsic surface state possibly involving Ti^{3+} was observed in the UPS. With continued bombardment the energy of the surface state shifted with concomitant loss of oxygen. The final UPS and ELS spectra for the bombarded surface was seen to be very similar to those of vacuum-fractured Ti_2O_3 . Interestingly, exposure to O_2 was seen to restore the bombarded surface back to the original TiO_2 surface.

Theoretical modeling of low energy inert gas ion induced desorption has been attempted [163,165,167,170]. Monte Carlo procedures have been used to simulate the sputtering of adsorbate layers. A modified version of the computer program MARLOW [171] has been used [165] to model the removal of sulfur and oxygen adsorbed on Ni by bombardment with 0.5 keV Ne^+ and He^+ . A modified version of the TRIMSP code [76] has been used to simulate the desorption of O from Ni(111) by 5–200 eV Ne^+ bombardment [167]. Both Monte Carlo programs simulate desorption by calculating many single-particle trajectories within the solid. The atoms move in straight line segments, changing their directions in binary collisions with stationary target atoms placed at the end of each segment, the scattering angles being calculated by an analytical method based on the Molière interatomic potential. A major limitation of the models is that the many-body aspects of low energy atom-atom interactions are neglected [172].

8.3. Chemical sputtering effects in reactive ion-surface interactions

Chemical desorption is indicated by observation of a sputtering yield with no sharp desorption threshold and which is higher than for other ion/target combinations of similar mass. The implantation of a reactive projectile in the target matrix is believed to precede chemical bonding and product desorption. This subject has been the topic of several recent reviews [5,6] so only an overview of the effect will be given here.

8.3.1. Atomic ion induced desorption

Fig. 56 shows the sputtering yields of carbon by hydrogen and oxygen ions as a function of the target temperature. In nearly all cases the sputtering yield exhibits a temperature dependent maximum between 720 and 920 K, a behavior typical of chemically induced erosion. The physical sputtering yield of C by energetic hydrogen (fig. 56a) is $\sim 10^{-2}$ atoms/ion in the range 100–1000 eV, while the maximum of the chemical sputtering yield increases to a value almost 10^{-1} atoms/ion. The temperature dependence of chemical sputtering of graphite by energetic oxygen is shown in fig. 56b. For 500 eV O^+ ions impinging on graphite, a monotonic increase in the sputtering yield was observed with increase in temperature between 22 and 500°C.

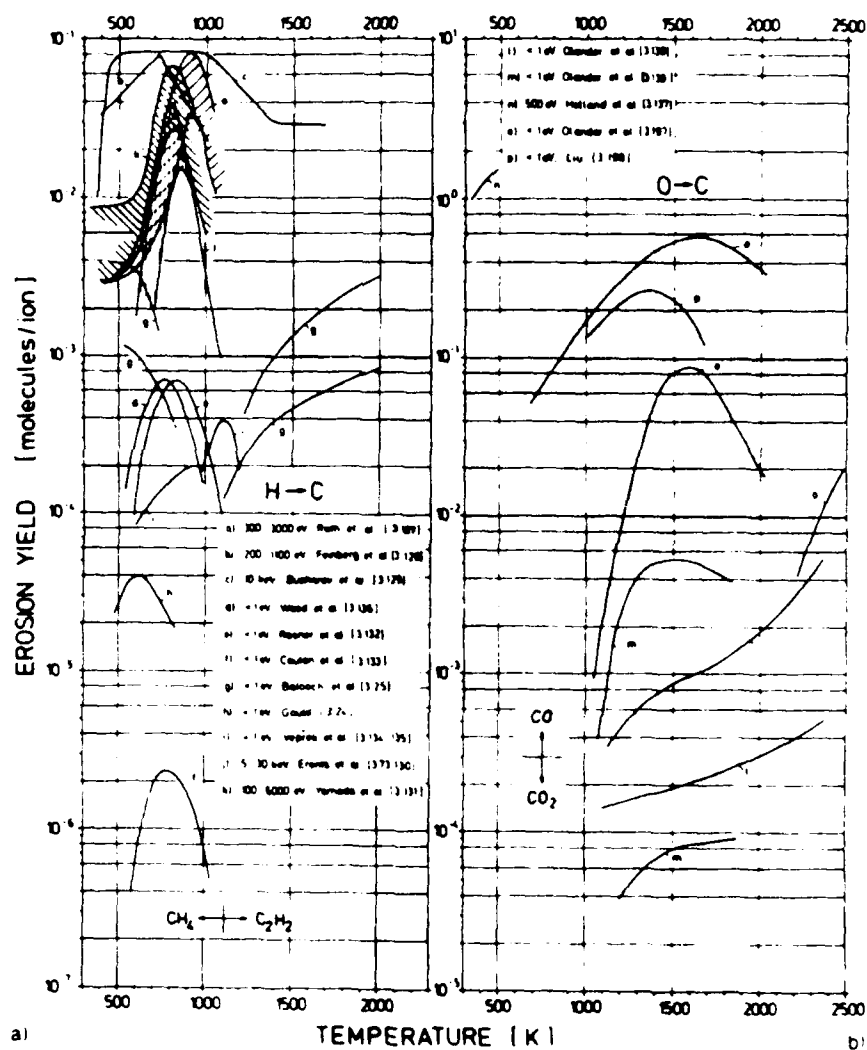


Fig. 56. Erosion yield of graphites due to interaction with hydrogen and oxygen as a function of temperature (a-f, i, n) measured by change in weight or volume, (g, k, j-m, o, p) measured by emission of CH_4 , C_2H_2 , CO or CO_2 . The shaded areas between curves a, h, and j indicate the range of reaction yields for different incident ion energies. Curves i and the higher curves g are obtained on prism planes, curves m and the lower curves g on basal planes of pyrolytic graphite. The lower curve e is obtained for O_2 , curve o for H_2O attack of graphite. With permission from ref. [6].

Sputtering of graphite has also been carried out with H, D and He ions with energies in the range 20-1000 eV [173]. At room temperature, the yield curve for He^+ ions decreases with energy as expected for physical sputtering. For

H^+ and D^+ ions, however, the sputtering yield increased with decreasing energy below 100 eV. This increase has been correlated with detection of desorbed CH_4 and CD_4 respectively.

The chemical sputtering behavior of an element is dependent on its chemical environment. Recently, the chemical sputtering of sintered diamond compacts, a diamond film, and graphite have been measured as a function of target temperature and H_2^+ ion energy [174]. Fig. 57 shows the energy dependence of the chemical sputtering yields (C/H) of the carbon surfaces. The CH_4 , C_2 , and C_1 hydrocarbon production yields from the diamond compacts are significantly lower than those for graphite. Raman spectroscopy showed that the bombarded surfaces of diamond compacts and films retained their sp^3 configuration, whereas the bombarded graphite surface was transformed into microstructural domains. These surface structural changes have been correlated with the higher erosion yields for graphite. Fig. 58 plots the energy dependence of σ_d for bombardment of graphite with a mass-analyzed beam of O^+ , C^+ and Ne^+ ions. Notice the high value for the sputtering yield for reactive oxygen bombardment, while sputter removal by Ne^+ shows a high E threshold. At the higher E , the sputtering yield of Ne^+ approaches that of O^+ suggesting that both ions induce desorption by momentum transfer. Similar studies of carbon desorption from a carbide and diamond films on Ni(111) by mass-analyzed beams of O^+ , Ne^+ and Ar^+ have been performed [50] as shown in fig. 53 and table 3. In the range 20–300 eV, O^+ ions exhibit

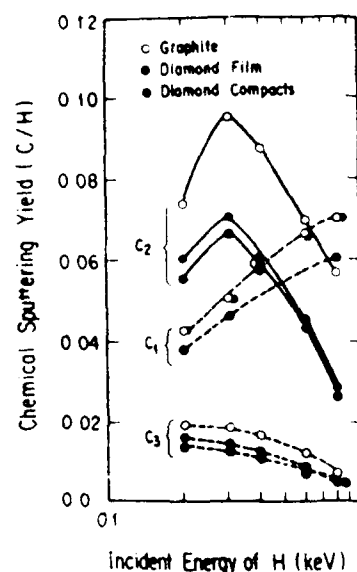


Fig. 57. Energy dependencies of the evaluated chemical sputtering yields (C/H) of C_1 , C_2 , and C_3 hydrocarbons at the peak temperature T_m . With permission from ref. [174].

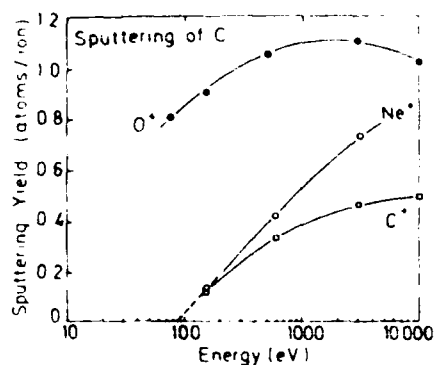


Fig. 58. Energy dependence of carbon sputtering with O^+ , Ne^+ , and C^+ ions at room temperature. With permission from ref. [6].

an energy independent sputtering behavior, in contrast to the > 30 eV threshold observed with Ne^+ and Ar^+ ions.

Fig. 59 shows the energy dependence of the sputtering cross-sections (yields) of $p(2 \times 2)$ oxide on $Ni(111)$ by (5–200 eV) C^+ . The figure illustrates in a very dramatic manner, the characteristics of chemical sputtering in comparison to physical sputtering. C^+ bombardment induced removal of O

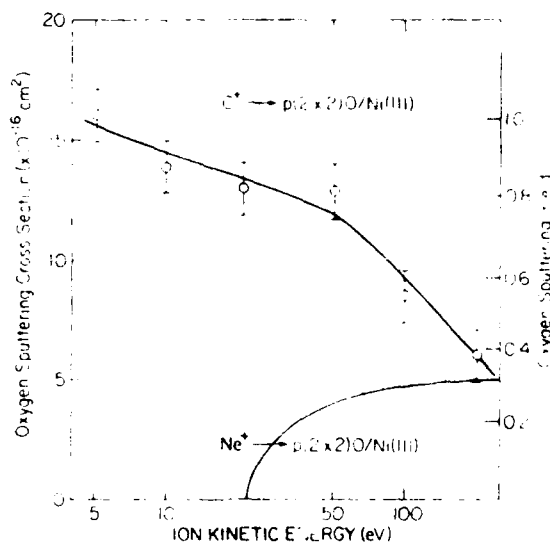


Fig. 59. Oxygen desorption yield as a function of projectile energy for the C^+/NiO and Ne^+/NiO systems. The oxygen is adsorbed as a $p(2 \times 2)$ oxide phase. With permission from ref. [48].

proceeds very efficiently ($S \approx 1.0$) at the lowest energies and gradually decreases with E , ultimately reducing to the momentum transfer limit at $E > 100$ eV. Ne^+ sputtering of O exhibits a significant threshold (~ 20 eV), implying that C^+/NiO interactions are completely chemical in the $E < 20$ –25 eV range.

8.3.2. Molecular ion induced desorption

An interesting aspect of the low energy chemical sputtering studies is the difference in the sputtering yields of atomic and molecular projectile ions. For the reaction of hydrogen at $E < 1$ –2 eV with graphite, Gould [175] has observed an increase in σ_d by orders of magnitude upon dissociation of hydrogen molecules. Balooch and Olander [176] have reported a similar result. For the reaction of graphite with oxygen, a similar difference in the desorption efficiencies of atomic and molecular oxygen has been observed [177].

Recently, collisions of polyatomic ions like pyrazine, acetaldehyde, etc. with surfaces of stainless steel, Pt, and Ag have been studied using a mass spectrometer [178]. The incident ion was found to abstract a hydrogen atom from the surface, although pick-up of up to four hydrogen atoms and/or a methyl group was observed in some cases. Interestingly, with very few exceptions, only odd-electron ions were found to undergo reactive ion-surface collisions, consistent with the thermochemical stability of the even-electron configuration.

8.3.3. Ion-assisted desorption in a reactive gas environment

Several studies have investigated chemical sputtering in an alternative way, i.e. by inert ion bombardment in a reactive gas atmosphere [179,180]. The ion beam provides energy for atom mobility at the collision site, while the reactive gas species chemically etch the surface. Table 4 shows the enhancement of the sputtering yield of Si and SiO_2 by 3 keV Ar^+ in a Cl_2 or XeF_2 atmosphere [181]. The chemical reactions that contribute to the etching process are also listed along with the reaction exothermicities. The enhancement factors have been explained in terms of an etch mechanism analogous to that of Winters

Table 4

Enhancement of the sputter yield in the presence of the reactive gas compared to the pure physical sputter yield under approximately equal experimental conditions; in the last column the exothermicity of reactions which take place in the collision cascade is indicated (from ref. [181])

System	Sputter yield enhancement	Chemical reaction
$\text{SiO}_2(\text{Cl}_2, \text{Ar}^+)$	1	$\text{Si}-\text{O} + \text{Cl} \rightarrow \text{Si}-\text{Cl} + \text{O} + 0.2 \text{ eV}$
$\text{SiO}_2(\text{XeF}_2, \text{Ar}^+)$	3	$\text{Si}-\text{O} + \text{F} \rightarrow \text{Si}-\text{F} + \text{O} + 1.1 \text{ eV}$
$\text{Si}(\text{Cl}_2, \text{Ar}^+)$	4	$\text{Si}-\text{Si} + \text{Cl} \rightarrow \text{Si}-\text{Cl} + \text{Si} + 2.8 \text{ eV}$
$\text{Si}(\text{XeF}_2, \text{Ar}^+)$	> 20	$\text{Si}-\text{Si} + \text{F} \rightarrow \text{Si}-\text{F} + \text{Si} + 3.7 \text{ eV}$

and Coburn [182]: adsorption of the reactive gas is followed by inert gas promoted atomic mixing and product formation, and finally ejection of the product complex.

A topic of debate in ion-assisted etching has been the observation that a majority of products have kinetic energy higher than thermal energy but much less than is usually observed with collisional sputtering processes [183,184]. Surface kinetic processes with residence times considerably longer than the collision cascade relaxation time have also been reported. Recently, this problem has been studied [185] by using modulated ion beam techniques to measure product identity and kinetic energy in ion-induced sputtering of GaAs by Cl_2 at room temperature. Modulated ion beams of 1 keV Ne^+ were used to etch the surface in the presence of a steady-state flux of Cl_2 with a neutral/ion flux ratio of 0–100. The major product species detected were GaCl_3 and AsCl_3 , and elemental Ga and As. Collisionally activated formation of products and desorption of the products during the relaxation time of the collision cascade was proposed as the etch mechanism.

8.4. Mechanisms for energetic reactive particle induced desorption

Chemical sputtering is a multistep process wherein the final step is formation of a volatile molecule. A process to be considered with adatoms on surfaces is electronic excitation of adsorbate complexes leading to desorption

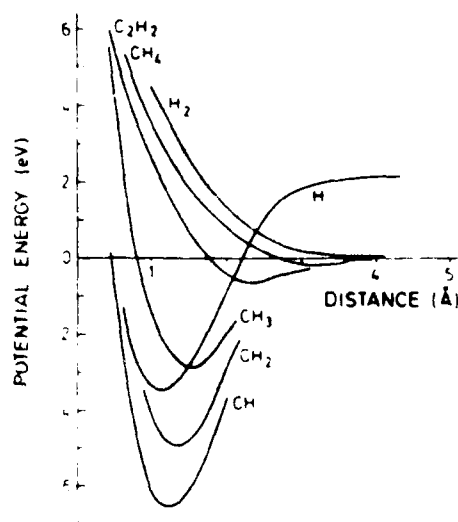
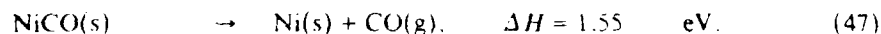
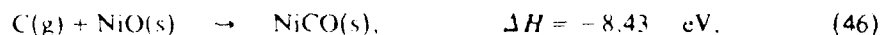


Fig. 60. Schematic diagram of the potential energies for the adsorption of hydrogen and different hydrocarbons on a carbon surface. With permission from ref. [6].

of the complex as ions or neutrals. This requires a primary excitation to a repulsive potential curve, by which conversion from electronic excitation to nuclear motion can occur.

A qualitative mechanism has been proposed [6] for the reaction of hydrogen with a carbon surface that is illustrated in fig. 60. Molecular hydrogen does not adsorb on a carbon surface, whereas atomic hydrogen is strongly bound. The hydrogen atoms adsorbed may then react with surface carbon atoms leading to the final formation of CH_4 and acetylene (C_2H_2), the former product desorbing spontaneously at temperatures above 50 K on account of its low binding energy (0.2 eV). These steps are represented by curve-crossings in the potential energy diagram.

A similar approach has been adopted to the reaction of C^+ and oxygen from a NiO surface to form gaseous CO [48]. The reaction has two intrinsic steps.



Reaction (46) is highly exoergic and the reaction energy released is complemented by the C^+ translational and inertial energy. The resulting energy released upon reaction can therefore be significantly greater than 8.43 eV and will act as a source of excitation to a repulsive potential for the system, thereby desorbing the CO adduct by rupturing the relatively weak Ni-CO bond.

Two theoretical models of surface reactive desorption processes have been given. The first is a version of the TRIM computer code used previously in examining Ne^+/NiO interactions, modified to include a bond formation mechanism [186], while the second is a stochastic trajectory calculation approach that incorporates attractive interatomic potential surfaces [187].

The Monte Carlo trajectory calculation approach (TRIM) has been used to model oxygen removal from a Ni(111) surface by C^+ bombardment [48]. For simulation of the momentum transfer contribution, C was treated as a non-reactive projectile and calculational procedures were similar to those discussed for the Ne/NiO system (section 8.2). Simulation of chemical desorption was performed by inclusion of a C-O bond formation step in the computations. Without rigorously incorporating attractive potential functions, a simplistic representation is made of the bond formation by assuming that a C atom moving within the range of the CO equilibrium distance from an O atom, with energy sufficiently low to be trapped in the domain, will combine with that O atom to form a CO molecule. Fig. 61 plots results for such calculations for a range of C^+ energies. Contributions of individual physical sputtering and chemical desorption processes as calculated by TRIM are shown, as also the calculated total sputtering yield. E_i in the figure represents

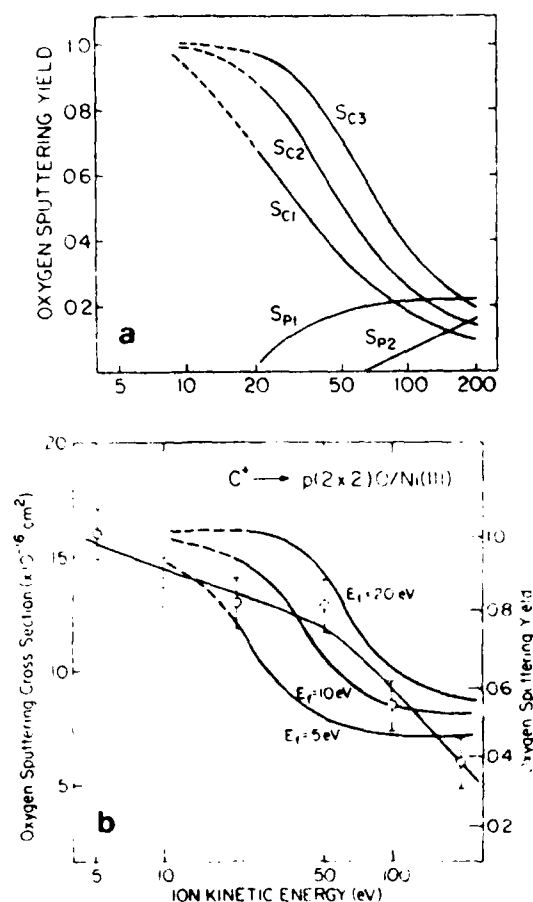
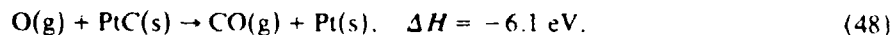


Fig. 61. (a) Contributions of individual physical sputtering and chemical desorption processes for $p(2 \times 2)$ NiO calculated by TRIMSP. S_{P1} : direct knock-off, S_{P2} : substrate sputtering, S_{C1} , S_{C2} , and S_{C3} : chemical desorption for final C trapping energies (E_f) of 5, 10, and 20 eV, respectively. The dotted lines below 20 eV E_k are extrapolated towards unit sputtering yield corresponding to complete C and O recombination. (b) Calculated total sputtering yields and experimental data.

the final energy in the collision processes below which the C atom is regarded as a trapped species. The calculations are in good agreement with experimental data and serve to emphasize the decreasing importance of chemical (potential) effects at higher energies on account of increasing ion ranges in the solid and the shorter duration of the attractive interactions between a projectile atom and an adsorbate atom.

A different approach based on stochastic classical trajectory calculations focuses on the dynamics of surface recombination processes [187]. Thermal

energy atomic O interaction with C adsorbed on a Pt(111) surface has been studied by this method. Sampling was done using 512 trajectories, 497 of which resulted in CO formation and desorption within 5 ps by the reaction



Only 4 trajectories (< 1% of total) corresponded to a trapping of the product CO molecule on the Pt surface. Fig. 62 plots the total energy distribution of the desorbed CO molecule, with > 90% of the heat liberated in the reaction (48) being retained in the CO molecule, indicating inefficient energy dissipation into surface and bulk. An interesting feature of the energy distribution is the lack of energy loss in Pt-CO bond dissociation (~ 1.2 eV). Such nonstatistical patterns of energy distribution could be due to preferential excitation of the CO molecule and could provide an interesting system for the study of surface reaction dynamics via state-specific detection of desorbed product molecules.

Classical trajectory simulations of atom and molecule ejection during low energy reactive ion bombardment have also been carried out for the Cu/(< 200 eV) O⁺ system [75]. The effect of adding an attractive part to the interaction potential on the sputtering was examined. The attractive part, essentially a Morse function was found to have no effect on atom ejection. However, O⁺ bombardment was found to result in relatively high yields of Cu₂ molecules

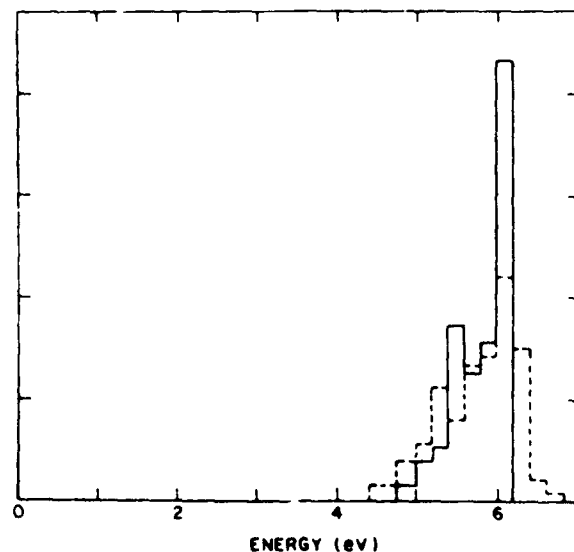


Fig. 62 Distribution of total energy (translation plus vibration plus rotation) in the product CO molecule computed for an O atom incident with $E = 0.087$ eV. Solid lines, surface temperature = 0 K. Dashed lines, surface temperature = 500 K. With permission from ref. [187].

and for $E < 100$ eV, CuO molecules were formed between surface Cu and primary O^+ .

Finally, it is useful to discuss the relative desorption efficiencies of thermal energy molecules versus thermal or energetic atoms/ions. It has been reported [48] that low energy (1–100 eV) O^+ ions remove surface carbonyl from NiCO, and carbon from NiC more efficiently than thermal energy oxygen molecules. Fig. 63 shows a schematic of a simplified potential energy diagram for the O/NiCO, O_2 /NiCO, O/NiC, and O_2 /NiC systems. CO removal by O_2 proceeds by the Langmuir–Hinshelwood mechanism [188] in which dissociation of O_2 and subsequent chemisorption of the oxygen atoms has to precede the chemical interaction between an oxygen atom and a CO molecule. The barrier to C and O recombination inhibits the reaction rate in this mechanism. In contrast, atomic oxygen (thermal or energetic) removes surface CO by the Rideal–Eley mechanism [188], in which the interaction between the gas-phase species and the surface complex is a direct one, without an intermediate adsorption step for the gas-phase atom. This is represented in the potential energy diagram of fig. 63, where an incoming oxygen atom can react with CO to form a CO_2 adduct that has a very shallow binding potential and so can easily escape from the surface with the excess energy available from the CO_2 formation reaction. The removal of NiC by O_2 or O follows an identical mechanistic route as above.

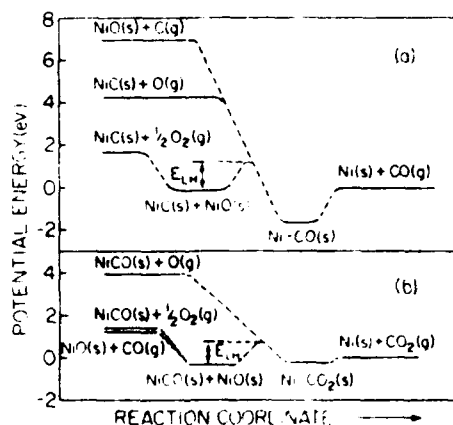


Fig. 63. Reaction coordinate diagrams for the (a) C and O recombination and (b) O and CO recombination reactions. Potential energies of reactants and products are drawn to scale, however the E_{LH} barrier heights are arbitrary. The desorption products, $Ni(s) + CO(g)$ and $Ni(s) + CO_2(g)$, are chosen as the zero potential energy references in (a) and (b), respectively. With permission from ref. [48].

9. Thin film deposition by low energy reactive ion bombardment

Many thin film deposition techniques involve some form of energetic bombardment of the growing matrix. It is now an established fact that the nature of the bombarding particle and its primary energy influence different film characteristics. As such, energetic particle bombardment includes plasma systems [8], dual beam sputtering [189], ionized cluster beam deposition (ICBD) [190], and mass-selected ion beams (MSIBD) [191]. The MSIBD offers the greatest control of the various parameters and can therefore provide the most insight into film growth phenomena on an atomic scale.

9.1. Homonucleation studies by mass-selected ion beam deposition (MSIBD)

Perhaps the simplest examples of low energy (< 100 eV) reactive bombardment based film growth are those in which the surface and beam atoms are the same chemical element. For $E < 100$ eV deposition occurs efficiently but as E increases self-sputtering becomes an important phenomenon. Depending on the sputter-deposition ratio a steady-state situation or a continuously receding surface layer of the substrate may be achieved. The advantage of using mass-analyzed, low energy ions to “deposit” films lies in the precise control over the ion type, flux, energy, and spatial profile of the impinging flux. Films can be grown with excellent isotopic composition, accurate thickness, and uniformity. Additionally, the methodology is ideally suited for parametric investigations of film growth processes [192].

Freeman [193] in 1976 described the adaptation of a laboratory-scale isotope separator for epitaxial growth of silicon by deposition of Si^+ ions retarded to low energy on to heated wafers of single-crystal silicon. Such behavior is expected from thermodynamic considerations and from the vapor-phase behavior of crystalline silicon. The epitaxial growth has been independently verified [194].

MSIBD of the semiconductor materials Si and Ge has been demonstrated recently in the range 40–200 eV on Si(100) and Ge [195]. Ge and Si layers that were perfectly continuous, had good thickness uniformity, and exhibited a sharp film–substrate interface were formed from ion doses of $(1-2) \times 10^{16}$ atoms/cm².

Epitaxial synthesis of diamond by MSIBD of low energy carbon ions has been reported [196]. An interference micrograph of such an epitaxial deposit, containing some large carbonaceous inclusions is shown in fig. 64. The photograph illustrates the continuous correlation between the deposited film and the substrate. Reproducible crystalline growth up to 10 μm in thickness and several mm² in area has been observed for 900 eV C^+ deposition on both natural and polished diamond substrates. In addition, three different forms of carbon have been observed.

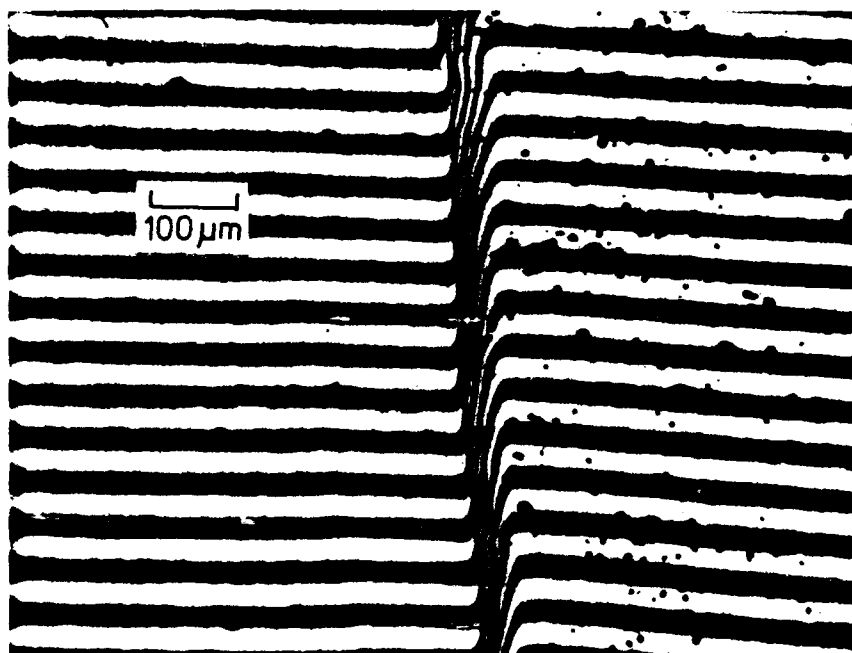


Fig. 64. Interferometric micrograph of an epitaxial carbon deposit containing inclusions on a polished diamond plaque. With permission from ref. [196].

9.2. Heteronucleation studies by MISBD

Deposition of particles on a chemically different substrate is chemically and physically more complex. Consideration must be given to the possibility of formation of binary phases, preferential substrate sputtering, segregation phenomena, and phase changes associated with the film itself. These processes compete with the growth of the described film and the relative efficiencies are dependent on deposition parameters such as ion energy, ion type, ion flux, presence/absence of fast neutrals in the projectile beam, vacuum conditions in the deposition chamber, substrate type, and temperature. Efficient film deposition is possible only by performing parametric investigations of the film growth.

Thomas et al. [197] have coined the term ion beam "epiplantation" for MISBD and have carried out deposition of thin films of Ag and Ge on Si(111) by this method. For both systems, epitaxial growth was achieved at temperatures (230–350°C) lower than encountered in chemical vapor deposition (CVD). In conjunction with the film deposition, sticking probability measurements have been made for 25–125 eV Ag⁺ and 25–300 eV Ge⁺ and are shown

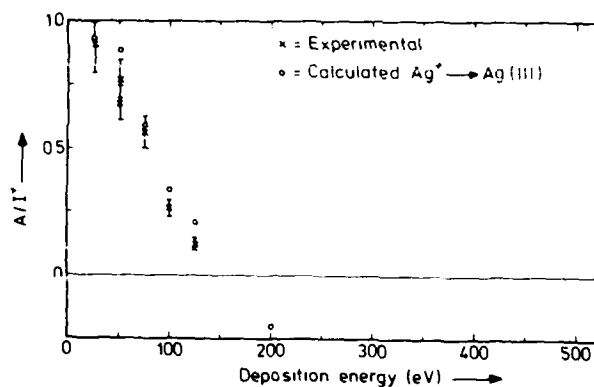


Fig. 65. Measured sticking probability of Ag^+ on its own lattice as a function of the deposition energy and simulations of the sticking probability from the MARLOWE calculations. With permission from ref. [197].

in figs. 65 and 66, respectively. In both cases S drops from near unity at the lowest E to near zero at the higher E . Growth of the crystalline films was explained in terms of localized hot spots generated by the energetic projectile atoms, i.e. the thermal spike model [198]. Other systems have been studied by MSIBD. Pb and Mg films have been grown by MSIBD in UHV [199]. Fig. 67 shows a series of electron diffraction patterns obtained from lead deposits on either a carbon film or NaCl. The crystallinity of the film had an E dependence; for low E an amorphous or polycrystalline structure resulted, while for $E \approx 120$ eV, a definite orientation was observed.

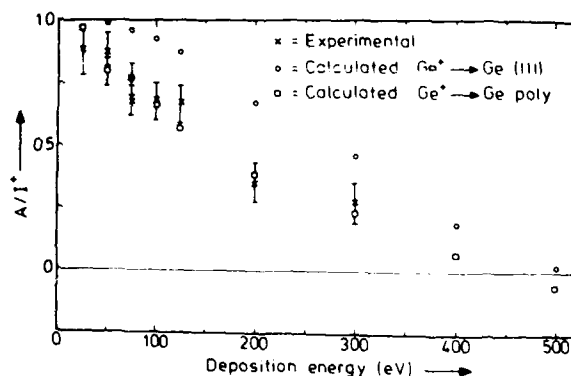


Fig. 66. Measured sticking probability of Ge^+ as a function of the deposition energy. MARLOWE calculations for Ge(111) and "amorphous" Ge are included for comparison. With permission from ref. [197].

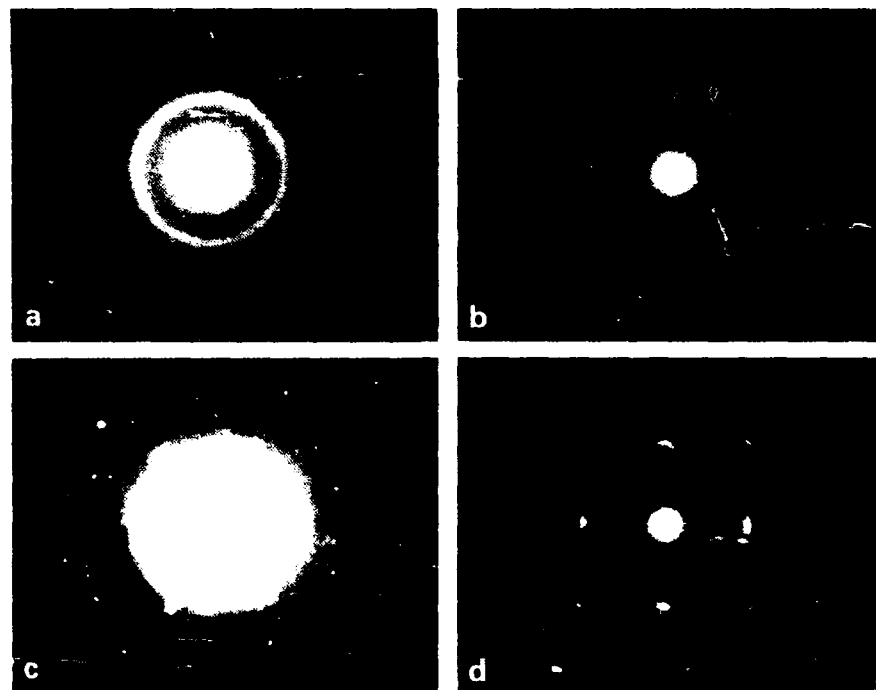


Fig. 67. Electron diffraction patterns of lead deposits on (a), (c) carbon film or (b), (d) NaCl: (a), (b) incident energy, 48 eV; (c), (d) incident energy, 121 eV. With permission from ref. [199].

MSIBD has been used recently [200] to enhance doping efficiency during growth of III-V compound semiconductor films. Traditionally, MBE techniques have been used in doping procedures but suffer from very low sticking probabilities for the dopant (group V) atoms. By supplying the dopant atoms by MSIBD methods, and combining it with MBE deposition of Group III atoms, enhanced sticking efficiencies have been obtained. Single-crystal GaAs films have been grown by this approach at substrate temperatures of 220–550°C, using As^+ ions of 100–200 eV.

Recently, there has been widespread interest in deposition of carbon films that have properties identical to those of diamond [50,189,192,201,202]. Chaikovskii et al. [202] have used 30–100 eV C^+ beams to deposit polycrystalline diamond films on a variety of substrates maintained at 25–50°C. The phase composition of the films was observed to be very sensitive to the presence of neutrals in the beam, graphitization becoming a severe problem with the presence of neutrals. Electron diffraction, AES and other techniques were used to identify the diamond phase.

Miyazawa et al. [203] and Anttila et al. [204] have also reported deposition

of diamond-like coatings using MSIBD. The coatings were amorphous, but had good adhesion and mechanical properties. Anttilla et al. [204] have compared the properties of coatings made from C^+ and various other hydrocarbon ion beams. The films prepared from hydrocarbon ions uniformly exhibited brittleness and poor adhesion.

Comprehensive surface spectroscopic characterization of low energy MSIBD of diamond film growth has been provided by Kasi et al. [50,192,201,205]. The first proof for chemical bonding of these films was obtained from AES, ELS, and ILS data. Fig. 68 (right) shows C KLL AES signatures for 30–180 eV C^+ deposition on Ni(111). Initial carbon deposition results in the formation of a subsurface carbide layer [fig. 68 (right, a)] that transforms with continued carbon exposure into a graphitic [fig. 68 (right, c)] and finally a diamond film structure [inset, fig. 68 (right)]. Similar evolutionary details have been mapped

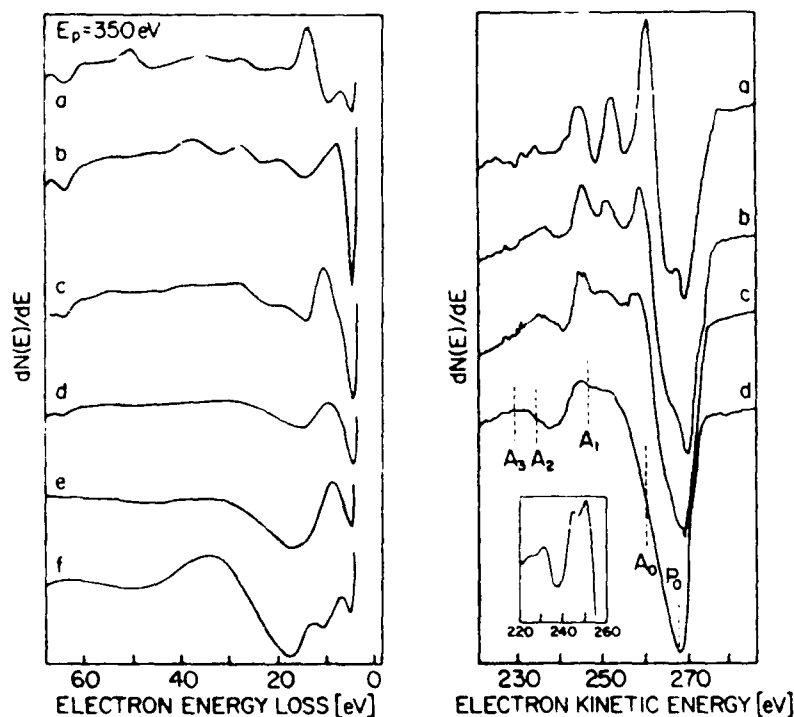


Fig. 68. Right panel: Evolution of the AES line shape from (a) carbidic to (d) e-beam damaged diamond for 75 eV C^+ deposition on Ni. The doses are as follows: (a) 2.0×10^{15} , (b) 6×10^{15} , (c) 9×10^{15} , and (d) $> 2 \times 10^{16}$ ions/cm². The inset shows a spectrum obtained with minimal electron beam exposure at the final stage. Left panel: ELS spectra of (a) clean Ni and the same surface after exposure to (b) 3×10^{15} , (c) 5×10^{15} , (d) 7×10^{15} , (e) 9×10^{15} , and (f) 2×10^{16} C^+ ions/cm² at 75 eV. The electron beam energy was 350 eV. With permission from ref. [192].

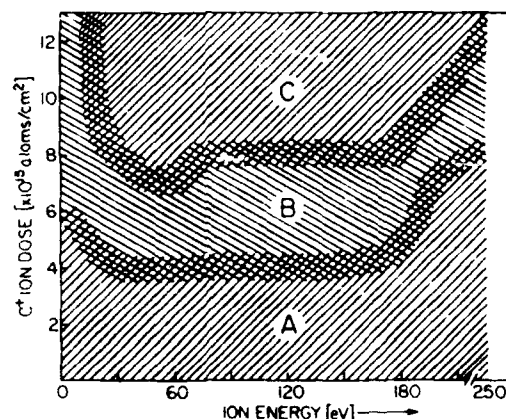


Fig. 69. Carbon phase transformations as a function of ion energy and fluence. Regions A, B, and C correspond to CKLL AES signatures of (a), (b), and (c) of fig. 68 (right). With permission from ref. [50].

out using ELS [fig. 68 (left)]. ELS and C 1s XPS data confirm the absence of π -bonding in the films, and the energy loss suffered in exciting a bulk plasmon in the film matched that of natural diamond. Epitaxial growth has been verified by XRD for room temperature C^+ deposition on Si(100) and TEM studies indicate that the film is composed of microcrystalline deposits of ~ 50 Å. Parametric investigations of the effect of C^+ energy and dose have been carried out [50] and the ideal energy range for diamond deposition reported to be 30–180 eV. Fig. 69 shows the energy-fluence dependence of the carbon phase transformations (fig. 68) for room temperature C^+ deposition on Ni(111). For $E \approx 30$ –180 eV efficient chemical rearrangement of the carbon deposits occurs and diamond formation occurs fastest. For $E < 30$ eV, the phase transformation does not proceed to the diamond structural stage, and highlights the important role of energy in low energy MSIBD. For $E > 180$ eV radiation effects in the form of lattice displacements and onset of self-sputtering become important, and when combined with increased ion range and straggling, necessitates higher doses to attain a final diamond structure in the AES. Lattice damage effects can be sometimes annealed out by maintaining the substrate to be coated at a high temperature during deposition. Freeman et al. [196] obtained crystalline diamond films for 900 eV C^+ deposition on diamond substrates maintained at $\sim 700^\circ\text{C}$.

Radiation induced segregation is a common phenomenon in multicomponent systems. For thin films, outward diffusion of the substrate or diffusion of the film material into the substrate lattice under the influence of energetic radiation is to be taken into account in formulating an efficient deposition

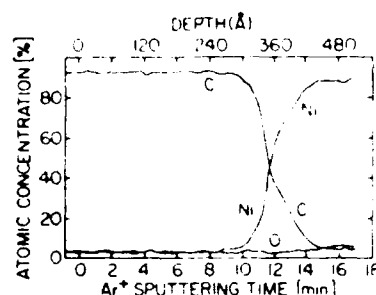


Fig. 70. Depth concentration profile using 3 keV Ar^+ ions for a 75 eV C^+ MSIBD diamond film on Ni(111). With permission from ref. [50].

scheme. For 150 eV C^+/Ni , Kasi et al. [50] have examined possible diffusion effects by 3 keV Ar^+ inert gas depth profiling. Fig. 70 shows the sputter depth profile data for the system and no segregation effects are evident. A sharp film-substrate interface characterizes the low energy MSIBD scheme.

It is clear from the many examples available in literature that film growth by MSIBD has numerous advantages. Systems which have been studied include, Cr [206], Zn [207], Pb [208], and cubic BN [209].

9.3. Ion-assisted deposition (IAD) of thin films

In section 8.3.3 reference was made to the possibility of sputter removing surface material chemically using a beam of inert gas ions in a reactive gas atmosphere. In a similar manner the simultaneous impact of energetic inert gas ions and thermal reactive atoms at a surface can be used to form thin films of the reactive atoms on the surface. Such a deposition arrangement is called ion-assisted deposition (IAD) wherein the inert gas ions provide local activation energy for chemical rearrangement. Parameters important to film growth and properties include ion energy and ion/vapor flux ratio [189].

Results of IAD of Cu films have been recently reported [210]. The effect of ion bombardment on the crystallographic texture, microhardness, crystallite size, and resistivity of the thick Cu films was seen to be very different at high energy (600 eV) as opposed to low energy (62 eV). Larger crystallite sizes and consequently lower resistivities were observed for lower E . The microhardness was higher for 600 eV Ar^+ IAD. The results have been interpreted in terms of increased Ar incorporation and lattice damage at the higher E . These studies emphasize the importance of ion E in the deposition process.

9.4. Theoretical formulation of energetic particle deposition

Simulation of film growth process has been performed using different classical approaches to develop an understanding of the mechanisms of MSIBD and IAD.

Thomas et al. [197] used a modified version of the program MARLOWE-10 [171,211] concentrating on two specific aspects of the "epiplantation" procedure: (i) the increase in concentration of the primary ions on the surface or in the near surface region and (ii) creation of damage in the crystal via atomic displacements initiated by the primary ions. The model was briefly described in section 8.1. The important parameter is E ; its dissipation creates lattice damage that is governed by a number of adjustable parameters; E^d - the bulk displacement energy, E^b - bulk binding energy, E^i - the minimum energy a moving atom can possess before it is trapped in the lattice, and E^s - surface displacement energy for an atom with a velocity component directed outward from the crystal surface. Figs. 65 and 66 show the predictive capabilities of the simulation procedure when applied to low energy MSIBD. While the agreement is satisfactory for $\text{Ag}^+/\text{Ag}(111)$, the calculated sticking probabilities for $\text{Ge}^+/\text{Ge}(111)$ were consistently higher than the experimental data and were better correlated when an amorphous target was used in the calculations. The results of the calculations were consistent with a growth process that involved short penetration depths, increased sputtering with E , and minimal back-scattering of the projectile ions.

Herbots et al. [195] have modeled 0-200 eV MSIBD of Si^+ and Ge^+ on Si by performing Monte Carlo calculations with TRIMSPUT [212]. The procedure produces a distribution that can be fitted by a Gaussian intersecting the surface of the substrate near the maximum of the distribution. Film growth by MSIBD was suggested to proceed in three steps: (i) in the initial stages, the implanted ions distribute in the first few layers until the maximum of the profile reaches an atomic concentration, N_i , equal to the atomic density of the material being deposited, η ; (ii) continued saturation of the layers between the surface and the maximum of the Gaussian at the same N_i , creating a new surface layer that contains only the MSIBD species; and (iii) true film growth involving increasing film thickness. Comparison of the experimental and calculated results showed that the Monte Carlo simulation code TRIMSPUT was able to provide quantitative values of the sputtering yields, ion ranges, and range straggling in the 40-200 eV range provided that the surface binding energy of the substrate, which is a crucial parameter in sputter removal of top layer substrate atoms during deposition, is known accurately for the experimental conditions.

Lifshitz et al. [205] have more recently described a "subplantation" model for growth of rigid, metastable films by MSIBD. Subsurface implantation, energy loss, preferential displacement of weakly bonded atoms in favor of

rigidly bonded atoms, and sputtering of substrate material are processes considered for hyperthermal particle interactions with the substrate. Epitaxial growth and preferred orientation result from the angular dependence of the displacement energy and the host *mold* effect. The model, supported by ion trajectory calculations and experimental data, has been applied to diamond film formation from 30–150 eV C^+ ions.

There have also been theoretical studies of the influence of projectile energy in thin film deposition using IAD. Two-dimensional molecular dynamics (2D MD) simulation [213,214] of the growth process and the resulting film structure has been investigated for a growing film of Lennard-Jones particles (zero substrate temperature). For IAD, 100 eV Ar^+ ion induced structural rearrangement of a growing Ni film was examined by the 2D MD procedure. The simulation technique of MD is a classical model in which the representative sample of the system is followed on the microscopic scale of time and

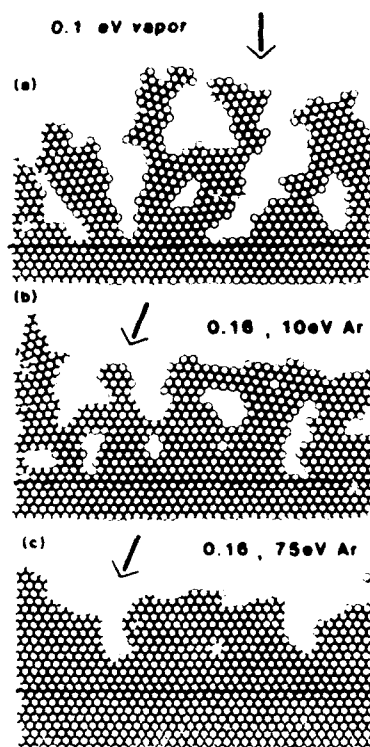


Fig. 71. (a)–(c) Typical microstructure obtained for condensing vapor atoms of 0.1 eV kinetic energy arriving under normal incidence (a) without ion bombardment, (b) with Ar bombardment of $E = 10$ eV and $J_i/J_v = 0.16$, (c) with Ar bombardment of $E = 75$ eV and $J_i/J_v = 0.16$. The atom-atom potential is U . With permission from ref. [213]

distance. Hamilton's equations were solved for a system of interacting film atoms, arriving vapor atoms, and the impinging ions. Ions are assumed to interact with the film atoms by a pairwise additive and spherically symmetric Molière potential. Fig. 71 shows the change in film microstructure for a fixed ion-to-vapor flux ratio ($j_{\text{ion}}/j_{\text{v}} = 0.16$), with increasing E . The sputtering yields were $S \approx 0$ for $E = 10$ eV, and $S \approx 0.7$ for $E = 75$ eV. It can be seen that void filling and corresponding film densification is more efficient at higher E for Ar^+ . Homoepitaxial growth is also supported by ion-assisted deposition according to the results of the simulations. Similar qualitative behavior is reported for increased ion/vapor ratios. The results have been explained in terms of increased adatom mobility due to the availability of local energy at the growth site.

10. Perspective

The interactions of low-energy, reactive ions with surfaces has been surveyed in this contribution. The spectrum of interaction channels available to atomic and molecular ions with energy in the chemically interesting range of 1–1000 eV has been considered. Elucidation of the panorama of interaction phenomena including, electronic processes, molecular dynamics, and chemical reactions has been provided by treatment of the phenomenological aspects of the ion-surface interaction. Specifically, examples have been provided of experimental and theoretical approaches used in the study of different aspects of the energetic gas-surface interaction problem. Information obtained from such segments can be used to reconstruct a complete picture of the multi-dimensional problem that is low-energy ion-surface interactions. Experimentally, these interactions can be studied within an ultra-high vacuum environment, allowing for dynamic in situ characterization of the reacted surface and any gas phase product evolution. Established surface analytical tools, such as AES, XPS, UPS, and LEED have found wide use, as have the more recent time-of-flight scattering and recoiling techniques.

Understanding ion-surface interactions is basic to a number of technologically important phenomena. Some of the most significant applications include film deposition, alteration of surface properties, understanding and controlling reactions in hostile environments, and inducing endothermic reactions. Concerning film deposition, low-energy, mass-selected ion beams are emerging as a new and exciting methodology for growing pure epitaxial films at low substrate temperatures. In alteration of surface properties, applications include preparation of metal surfaces or films that are chemically inert and corrosion resistant, surface hardening and passivation, preparation of catalyst surfaces that are selective and specific to desired reactions, adjustment of electronic band gaps and surface conductivities, and alteration of polymer

surfaces. Applications in hostile environments include plasma etching and processing of materials, nuclear reactors, interstellar atmospheric processes, high-temperature and stress situations, and development of non-equilibrium plasma chemistry. Inducing novel reactions includes stimulation of endothermic processes at low temperature, studies of catalytic reaction mechanisms, and production of new and novel compounds on surfaces.

Acknowledgments

This material is based on work supported by the National Science Foundation under Grant Nos. DMR-8610597 and CHE-8513966, by the R.A. Welch Foundation under Grant No. E-656, and the US Air Force Research Office under Contract No. F19628-86-K-0013.

References

- [1] R.B. Gerber, *Chem. Rev.* 87 (1987) 29.
- [2] M.P. D'Evelyn and R.J. Madix, *Surface Sci. Rept.* 3 (1984) 413.
- [3] J.A. Barker and D.J. Auerbach, *Surface Sci. Rept.* 4 (1985) 1.
- [4] L.C. Feldman, *CRC Crit. Rev. Solid State Mater. Sci.* 10 (1981) 143.
- [5] P. Sigmund, in: *Sputtering by Particle Bombardment I*, Ed. R. Behrisch, Vol. 47 of Topics in Applied Physics (Springer, New York, 1981).
- [6] J. Roth, in: *Sputtering by Particle Bombardment II*, Ed. R. Behrisch, Vol. 52 of Topics in Applied Physics (Springer, New York, 1983).
- [7] U. Wille and R. Hippler, *Phys. Rept.* 132 (1986) 131.
- [8] H.F. Winters, *Topics in Current Chemistry*, Vol. 94 (Springer, Berlin, 1980) p. 69.
- [9] D.M. Gruen, A.R. Krauss, M.J. Pellin and C.E. Young, Eds., *Particle and Photon Interactions With Surfaces* (North-Holland, Amsterdam, 1987).
- [10] W. Eckstein, V.A. Molchanov and H. Verbeek, *Nucl. Instr. Methods* 149 (1978) 599.
- [11] S.B. Luitjens, A.J. Algra, E.P. Th. M. Suurmeijer and A.L. Boers, *Surface Sci.* 99 (1980) 631.
- [12] W. Heiland and E. Taglauer, *Nucl. Instr. Methods* 132 (1976) 535.
- [13] R. Kumar, M.H. Mintz and J.W. Rabalais, *Surface Sci.* 147 (1984) 15.
- [14] R.A. Baragiola, *Radiation Effects* 61 (1982) 47.
- [15] R.A. Baragiola, E.V. Alonso and H.J.L. Raiti, *Phys. Rev. A* 25 (1982) 1969.
- [16] G. Zampieri, F. Meier and R. Baragiola, *Phys. Rev. A* 29 (1984) 116.
- [17] S.V. Pepper and J. Ferrante, *Surface Sci.* 88 (1979) L1.
- [18] T.D. Andreadis, J. Fine and J.A.D. Matthew, *Nucl. Instr. Methods* 209/210 (1983) 495.
- [19] For recent reviews, see E.W. Thomas, *Vacuum* 34 (1984) 1031; *Progr. Surface Sci.* 10 (1980) 383.
- [20] M. Braun and B. Emmoth, *Nucl. Instr. Methods* 170 (1980) 585.
- [21] K.W. Hill, J. Comas, D.J. Nagel and A.R. Knudsen, *Phys. Scripta* 20 (1979) 652; A.R. Knudson, D.J. Nagel, J. Comas and K.W. Hill, *Nucl. Instr. Methods* 149 (1978) 507.
- [22] R.S. Bhattacharya, K.G. Lang, A. Scharmann and K.H. Scharfner, *J. Phys. D (Appl. Phys.)* 11 (1978) 1935; R.S. Bhattacharya, D. Hasselkamp and K.H. Scharfner, *J. Phys. D. (Appl. Phys.)* 12 (1979) L55.
- [23] K.H. Scharfner, H.J. Flaig, D. Hasselkamp and A. Scharmann, *Nucl. Instr. Methods* 168 (1980) 419.

- [24] T.M. Buck, G.H. Wheatley and L.K. Verheij, *Surface Sci.* 90 (1979) 635.
- [25] J.W. Rabalais, J.A. Schultz, R. Kumar and P.T. Murray, *J. Chem. Phys.* 78 (1983) 5250.
- [26] A.J. Algra, E. van Loenen, E.P.Th.M. Suurmeijer and A.L. Boers, *Radiation Effects* 60 (1982) 173.
- [27] Y.S. Jo, J.A. Schultz, T.R. Schuler and J.W. Rabalais, *J. Phys. Chem.* 89 (1985) 2113.
- [28] W. Eckstein, in: *Inelastic Particle-Surface Collisions*, Eds. E. Taglauer and W. Heiland (Springer, Berlin, 1981) p. 157.
- [29] B. Willerding, W. Heiland and K.J. Snowdon, *Phys. Rev. Letters* 53 (1984) 2031.
- [30] B. Willerding, H. Steininger, K.J. Snowdon and W. Heiland, *Nucl. Instr. Methods B* 2 (1984) 453.
- [31] L.L. Balashova, A.I. Dodonov, Sh.N. Gann, E.S. Mashkova and V.A. Molchanov, *J. Phys. B* 16 (1983) 2609.
- [32] D.A. Baldwin, N. Shamur and J.W. Rabalais, *Surface Sci.* 141 (1984) 617.
- [33] N. Shamur, D.A. Baldwin, T. Darko and J.W. Rabalais, *J. Chem. Phys.* 76 (1982) 6417.
- [34] D.A. Baldwin, N. Shamur and J.W. Rabalais, *Appl. Surface Sci.* 11/12 (1982) 229.
- [35] M.D.A. Mabud, M.J. Dekrey and R.G. Cooks, *Intern. J. Mass Spectrom. Ion Phys.* 67 (1985) 285.
- [36] B. Willerding, K.J. Snowdon, U. Imke and W. Heiland, 11th Intern. Conf. on Atomic Collisions in Solids, Georgetown University, Washington, DC, August 1985.
- [37] A.C. Luntz, A.W. Kleyn and D.J. Auerbach, *Phys. Rev. B* 25 (1982) 4273; *J. Chem. Phys.* 76 (1982) 737.
- [38] J.C. Brenot, D. Dhucq, J.P. Gauyacq, J. Pommier, V. Sidis, M. Barat and E. Pollack, *Phys. Rev. A* 11 (1975) 1245.
- [39] B. Fastrup, G. Hermann and K.J. Smith, *Phys. Rev. A* 3 (1971) 1591.
- [40] N.H. Tolk, J.C. Tully, C.W. White, J. Kraus, A.A. Monge, D.L. Simms, M.F. Robbins, S.H. Neff and W. Lichten, *Phys. Rev. A* 13 (1976) 969.
- [41] J. Bohdanský, J. Roth and H.L. Bay, *J. Appl. Phys.* 51 (1980) 2861.
- [42] P. Apell, *Nucl. Instr. Methods B* 23 (1987) 242.
- [43] H.D. Hagstrum, *Phys. Rev.* 96 (1954) 336.
- [44] H.D. Hagstrum and G.F. Becker, *Phys. Rev. B* 8 (1973) 107.
- [45] L.J. Varnerin, Jr., *Phys. Rev.* 91 (1953) 859.
- [46] H. Kang, T.R. Schuler and J.W. Rabalais, *Chem. Phys. Letters* 128 (1986) 348.
- [47] H. Kang, S.R. Kasi and J.W. Rabalais, *J. Chem. Phys.* 88 (1988) 5882.
- [48] H. Kang, S.R. Kasi, O. Grizzi and J.W. Rabalais, *J. Chem. Phys.* 88 (1988) 5894.
- [49] S.R. Kasi, M. Kilburn, H. Kang, J.W. Rabalais, L. Tavernini and P. Hochmann, *J. Chem. Phys.* 88 (1988) 59.
- [50] S.R. Kasi, H. Kang and J.W. Rabalais, *J. Chem. Phys.* 88 (1988) 5914.
- [51] H.F. Winters and D.E. Horne, *Surface Sci.* 24 (1971) 587.
- [52] H.F. Winters, *J. Vacuum Sci. Technol.* 8 (1971) 17.
- [53] J.N. Chen, M. Shi, S. Tachibana and J.W. Rabalais, *Nucl. Instr. Methods B* 16 (1986) 91.
- [54] E.A. Kurz, *Am. Lab.* March 1979.
- [55] C.N. Burrows, A.J. Lieber and V. Zaviantseff, *Rev. Sci. Instr.* 38 (1967) 1477; M.A. Gruntman and V.A. Morozov, *J. Phys. E* 15 (1982) 1356; S. Takagi, Y. Kawasumi, N. Noda and J. Fujita, *Japan. J. Appl. Phys.* 22 (1983) 1453; J.G. Timothy and R.L. Bybee, *Rev. Sci. Instr.* 49 (1978) 1192.
- [56] R.H. Jones, D.R. Olander, W.J. Siekhaus and J.A. Schwarz, *J. Vacuum Sci. Technol.* 9 (1972) 1429.
- [57] J. Bates, D.M. Gruen and R. Varma, *Rev. Sci. Instr.* 47 (1976) 1506; D.M. Gruen, S.L. Gaudioso, R.L. McBeth and J.L. Lerner, *J. Chem. Phys.* 60 (1974) 89.
- [58] P.A. Finn, D.M. Gruen and D.L. Page, in: *Radiation Effects on Solid Surfaces*, *Advan. in Chem. Ser.* 158 (1976) 30.

- [59] A. Hurkmans, E.G. Overbosch, D.R. Olander and J. Los, *Surface Sci.* 54 (1976) 154.
- [60] A. Hurkmans, E.G. Overbosch and J. Los, *Surface Sci.* 62 (1977) 621; 63 (1977) 417; 59 (1976) 488.
- [61] J.J.C. Geerlings, I.F.T. Kwakman and J. Los, *Surface Sci.* 184 (1987) 305.
- [62] R.M. Lemmon, *Acc. Chem. Res.* 6 (1973) 65.
- [63] H.M. Pohlit, W.R. Erwin, T.H. Lin and R.M. Lemmon, *J. Phys. Chem.* 75 (1971) 2555.
H.M. Pohlit and R.M. Lemmon, *J. Phys. Chem.* 75 (1971) 2558.
T.H. Lin and R.M. Lemmon, *J. Phys. Chem.* 75 (1971) 3524.
- [64] D.P. Smith, *J. Appl. Phys.* 38 (1967) 340.
- [65] H. Goldstein, *Classical Mechanics* (Addison-Wesley, Reading, MA, 1959).
- [66] L.I. Schiff, *Quantum Mechanics*, 3rd ed. (McGraw-Hill, New York, 1968).
- [67] C. Lehmann, *Interaction of Radiation With Solids and Elementary Defect Production* (North-Holland, Amsterdam, 1977).
- [68] D.E. Harrison, *Radiation Effects* 70 (1983) 1.
- [69] A. van Veen and J. Haak, *Phys. Letters A* 40 (1972) 378.
- [70] L.I. Tongson and C.B. Cooper, *Surface Sci.* 122 (1975) 263.
- [71] V.I. Veksler, *Soviet Phys.-Solid State* 6 (1965) 1767.
- [72] V.A. Arifov, *Interactions of Atomic Particles With a Solid Surface* (Plenum, New York, 1969) p. 93.
- [73] E. Hulpke, *Surface Sci.* 52 (1975) 615.
- [74] V. Gelach-Meyer, E. Hulpke and H.D. Meyer, *Chem. Phys.* 36 (1979) 327.
- [75] D.E. Harrison, P. Avouris and R. Walkup, *Nucl. Instr. Methods B* 18 (1987) 349.
- [76] J.F. Ziegler, J.P. Biersack and U. Littmark, *The Stopping and Ranges of Ions in Solids*, Vol. 1 (Pergamon, New York, 1985).
- [77] I.M. Torrens, *Interatomic Potentials* (Academic Press, New York, 1972).
- [78] W. Eckstein, H. Verbeek and S. Datz, *Appl. Phys. Letters* 27 (1975) 527.
- [79] P. Massmann, H. Hopman and J. Los, *Nucl. Instr. Methods* 165 (1979) 531.
- [80] H. Verbeek, W. Eckstein and R.S. Bhattacharya, *Surface Sci.* 95 (1980) 380.
- [81] P.J. Schneider, W. Eckstein and H. Verbeek, *Nucl. Instr. Methods* 194 (1982) 387.
- [82] W. Heiland, U. Beitz and E. Taglauer, *Phys. Rev. B* 19 (1975) 1677.
- [83] W. Heiland and E. Taglauer, *Nucl. Instr. Methods* 194 (1982) 667.
- [84] L.L. Balashova, Sh.N. Gann, A.I. Dodonov, E.S. Mashkova and V.A. Molchanov, *Surface Sci.* 119 (1982) L378.
- [85] A.I. Dodonov, Sh. N. Gann, E.S. Mashkova and V.A. Molchanov, *Surface Sci.* 140 (1984) L244.
- [86] B. Willerding, K.J. Snowdon, U. Imke and W. Heiland, *Nucl. Instr. Methods B* 13 (1986) 614.
- [87] C.S. Sass and J.W. Rabalais, *J. Chem. Phys.* 89 (1988) 3870.
- [88] K.H. Purser, R.H. Rose, N.B. Brooks, R.P. Bastide and A.B. Wittkower, *Phys. Letters* 6 (1963) 176.
- [89] I.S. Bitenski and E.S. Parillis, in: *Proc. Symp. on Sputtering*, Vienna, Eds. P. Varga, G. Betz and F. Viehbock (1980) p. 688.
- [90] I.S. Bitenski and E.S. Parillis, *Soviet Phys.-Tech. Phys.* 26 (1981) 1042.
- [91] I.S. Bitenski and E.S. Parillis, *Nucl. Instr. Methods B* 2 (1984) 364.
- [92] M.M. Jakas and D.E. Harrison, *Surface Sci.* 145 (1985) 500.
- [93] W. Heiland, U. Imke, S. Schubert and K.J. Snowdon, *Nucl. Instr. Methods B* 27 (1987) 167.
- [94] B. Willerding, K. Snowdon and W. Heiland, *Z. Phys. B* 59 (1985) 435.
- [95] K.J. Snowdon, B. Willerding and W. Heiland, *Phys. Rev. B* 34 (1986) 41.
- [96] S. Schubert, J. Neuman, U. Imke, K.J. Snowdon, P. Varga and W. Heiland, *Surface Sci.* 171 (1986) L375.
- [97] U. Fano and W. Lichten, *Phys. Rev. Letters* 14 (1965) 627.

- [98] M.D.A. Mabud, M.J. Dekrey, R.G. Cooks and T. Ast, *Intern. J. Mass Spectrom. Ion Phys.* 69 (1986) 277.
- [99] M.J. Dekrey, H.I. Kenttamaa, V.H. Wysocki and R.G. Cooks, *Org. Mass Spectrom.* 21 (1986) 193.
- [100] P.J. Schneider, W. Eckstein and H. Verbeek, *Nucl. Instr. Methods* 194 (1982) 387.
- [101] R. Kumar, J.A. Schultz and J.W. Rabalais, *Chem. Phys. Letters* 97 (1983) 256.
- [102] J.A. Schultz, R. Kumar and J.W. Rabalais, *Chem. Phys. Letters* 100 (1983) 214.
- [103] J.W. Rabalais, J.N. Chen and R. Kumar, *Phys. Rev. Letters* 55 (1985) 1124.
- [104] R. Kumar, J.N. Chen and J.W. Rabalais, *Langmuir* 1 (1985) 294.
- [105] J.N.M. van Wunnik, J.J.C. Geerlings, E.H.A. Granneman and J. Los, *Surface Sci.* 131 (1983) 17.
- [106] R.J. MacDonald, D.J. O'Connor and P. Higgenbottom, *Nucl. Instr. Methods B* 2 (1984) 418.
- [107] R.J. MacDonald and D.J. O'Connor, *Surface Sci.* 124 (1983) 423.
- [108] R.F. Garrett, R.J. MacDonald and D.J. O'Connor, *Surface Sci.* 138 (1984) 432.
- [109] J.W. Rabalais, J.N. Chen, R. Kumar and M. Narayana, *J. Chem. Phys.* 83 (1985) 6489.
- [110] A.L. Boers, *Nucl. Instr. Methods B* 2 (1984) 353.
- [111] H.D. Hagstrum, *Electron and Ion Spectroscopy of Solids*, Eds. L. Tiersman, J. Vennik and W. Dekeyser (Plenum, New York, 1978).
- [112] M. Barat and W. Lichten, *Phys. Rev. A* 6 (1972) 211.
- [113] U. Imke, K.J. Snowden and W. Heiland, *Phys. Rev. B* 34 (1986) 41.
- [114] U. Imke, K.J. Snowden and W. Heiland, *Phys. Rev. B* 34 (1986) 48.
- [115] J.N.M. van Wunnik and J. Los, *Phys. Scripta T* 6 (1983) 27.
- [116] D.M. Newns, K. Makoshi, R. Brako and J.N.M. van Wunnik, *Phys. Scripta T* 6 (1983) 5.
- [117] C.A. Moyer and K. Orvek, *Surface Sci.* 114 (1982) 295.
- [118] C.A. Moyer and K. Orvek, *Surface Sci.* 121 (1982) 138.
- [119] G. Doyen, *Surface Sci.* 117 1982 85.
- [120] F.T. Smith, *Phys. Rev.* 179 (1969) 111.
- [121] W. Lichten, *J. Phys. Chem.* 84 (1980) 2102.
- [122] J.A. Schultz, M.H. Mintz, T.R. Schuler and J.W. Rabalais, *Surface Sci.* 146 (1984) 438.
- [123] J.N. Chen and J.W. Rabalais, *Nucl. Instr. Methods B* 13 (1986) 597;
J.N. Chen and J.W. Rabalais, *J. Am. Chem. Soc.* 110 (1988) 46.
- [124] J.W. Rabalais and J.N. Chen, *J. Chem. Phys.* 85 (1986) 3615.
- [125] J.N. Chen, M. Shi and J.W. Rabalais, *J. Chem. Phys.* 86 (1987) 2403.
- [126] M.J. Vasile, *Surface Sci.* 115 (1982) L141.
- [127] K. Wittmaack, in: *Inelastic Ion-Surface Collisions*, Eds. N. Tolk, J.C. Tulley, W. Heiland and C.W. White (Academic Press, New York, 1977) p. 153.
- [128] W.F. van der Wig and D.J. Bierman, *Physica* 44 (1969) 206.
- [129] J.W. Gadzuk, *Surface Sci.* 6 (1967) 133.
- [130] J.W. Gadzuk, *Phys. Rev. B* 1 (1970) 2110.
- [131] B. Rasser and M. Remy, *Surface Sci.* 93 (1980) 223.
- [132] D.P. Woodruff, *Nucl. Instr. Methods* 194 (1982) 639.
- [133] A.J. Algra, PhD Thesis, Groningen (1981).
- [134] E.G. Overbosch, B. Rasser, A.D. Tenner and J. Los, *Surface Sci.* 92 (1980) 310.
- [135] S. Aduru and J.W. Rabalais, *Surface Sci.* 205 (1988) 269.
- [136] K.J. Snowden, P.J. O'Connor and R.J. MacDonald, *unpublished results*.
- [137] K.J. Snowden, *Nucl. Instr. Methods B*, in press.
- [138] S. Schubert, U. Imke, W. Heiland, K.J. Snowden, P.H.F. Reijnen and A.W. Kleyn, *unpublished results*.
- [139] B. Bartos, H.J. Freund, H. Kühlenbeck, M. Neumann, H. Linder and K. Müller, *Surface Sci.* 179 (1987) 59.

- [140] S.R. Kasi, Y. Lifshitz and J.W. Rabalais, to be published.
- [141] H.K. Hu, J.A. Schultz and J.W. Rabalais, *J. Phys. Chem.* 86 (1982) 3364.
- [142] A. Amirav and M.J. Cardillo, *Phys. Rev. Letters* 57 (1986) 2299;
A. Amirav, M.J. Cardillo, P.L. Trevor, C. Lim and J.C. Tully, *J. Chem. Phys.* 87 (1987) 1796.
- [143] H.F. Winters, *J. Chem. Phys.* 44 (1966) 1472.
- [144] H.F. Winters, *J. Appl. Phys.* 43 (1972) 4808.
- [145] H.F. Winters and D.E. Horne, *Phys. Rev. B* 10 (1974) 55.
- [146] J. Geerk and O. Meyer, *Surface Sci.* 32 (1972) 222.
- [147] C. Grangaza, G. Carter and G. Farrell, *Nucl. Instr. Methods* 132 (1976) 679.
- [148] V. Franchetti, B.H. Solka, W.E. Baiting, J.W. Amy and R.G. Cooks, *Intern. J. Mass Spectrom. Ion Phys.* 23 (1977) 29.
- [149] J.A. Taylor, G.M. Lancaster, A. Ignatiev and J.W. Rabalais, *J. Chem. Phys.* 68 (1978) 1776;
J.A. Taylor, G.M. Lancaster and J.W. Rabalais, *J. Electron Spectrosc. Related Phenomena* 13 (1978) 435.
- [150] H.K. Hu and J.W. Rabalais, *J. Phys. Chem.* 85 (1981) 2459.
- [151] J.A. Taylor, G.M. Lancaster and J.W. Rabalais, *J. Am. Chem. Soc.* 100 (1978) 4441.
- [152] J.A. Taylor, G.M. Lancaster and J.W. Rabalais, *Appl. Surface Sci.* 1 (1978) 503.
- [153] D.A. Baldwin, N. Shamir, P. Hochmann and J.W. Rabalais, *Surface Sci.* 130 (1983) 361.
- [154] P. Sigmund, A. Oliva and G. Falcone, *Nucl. Instr. Methods* 194 (1982) 541.
- [155] P. Sigmund and A. Gras-Marti, *Nucl. Instr. Methods* 182/183 (1981) 25.
- [156] E. Wirz, H.R. Oswald and S. Veprek, in: *Proc. 4th Intern. Symp. on Plasma Chemistry*, Vol. 2, Eds. S. Veprek and J. Hertz (Univ. Zurich, Zurich, 1979) p. 492.
- [157] H.K. Hu, Y. Fukuda, D.A. Baldwin, P.T. Murray and J.W. Rabalais, *J. Chem. Phys.* 72 (1980) 6158.
- [158] H.K. Hu, P.T. Murray, Y. Fukuda and J.W. Rabalais, *J. Chem. Phys.* 74 (1981) 2247.
- [159] J.-E. Sundgren, B.-O. Johansson and S.-E. Karlsson, *Surface Sci.* 128 (1983) 265.
- [160] R. Sigmund, *Nucl. Instr. Methods B* 27 (1987) 1.
- [161] R. Kelly, *Surface Sci.* 100 (1980) 85.
- [162] R. Shimizu, *Nucl. Instr. Methods B* 18 (1987) 486.
- [163] H.F. Winters and P. Sigmund, *J. Appl. Phys.* 45 (1974) 4760.
- [164] E. Taglauer, U. Beitz, G. Marin and W. Heiland, *J. Nucl. Mater.* 63 (1976) 193.
- [165] E. Taglauer, G. Marin, W. Heiland and U. Beitz, *Surface Sci.* 63 (1977) 507.
- [166] S. Nagata, H. Bergsaker, B. Emmoth and L. Ilyinsky, *Nucl. Instr. Methods B* 18 (1987) 515.
- [167] J.W. Rabalais, T.R. Schuler and O. Grizzi, *Nucl. Instr. Methods B* 28 (1987) 185.
- [168] J.A. Schultz, P.T. Murray, R. Kumar, H.K. Hu and J.W. Rabalais, in: *Desorption Induced by Electronic Transitions: DIET I*, Eds. N.H. Tolk, J.C. Tully and T.E. Madey, Springer Series in Chemical Physics 24 (1983) 191.
- [169] V.E. Henrich, G. Dresselhaus and H.J. Zeiger, *Phys. Rev. Letters* 36 (1976) 1335.
- [170] P. Sigmund, *Phys. Rev.* 184 (1969) 383.
- [171] M.T. Robinson and I.M. Torrens, *Phys. Rev.* 93 (1974) 5008.
- [172] M.M. Jakas and D.E. Harrison, Jr., *Nucl. Instr. Methods B* 14 (1986) 535.
- [173] J. Roth and J. Bohdanský, *Nucl. Instr. Methods B* 23 (1987) 549.
- [174] R. Yamada, *J. Vacuum Sci. Technol. A* 5 (1987) 2222.
- [175] R.K. Gould, *J. Chem. Phys.* 63 (1975) 1825.
- [176] M. Balooch and D.R. Olander, *J. Chem. Phys.* 63 (1975) 4772.
- [177] D.E. Rosner and H.D. Allendorf, in: *Proc. Intern. Conf. on Heterogeneous Kinetics at Elevated Temperatures*, Univ. of Pennsylvania, 1969, p. 231.
- [178] T. Ast, Md. A. Mabud and R.G. Cooks, *Intern. J. Mass. Spectrom. Ion Proc.* 82 (1988) 131.
- [179] J.W. Coburn and H.F. Winters, *J. Appl. Phys.* 50 (1979) 3189.
- [180] Y. Tu, T.J. Chuang and H.F. Winters, *Phys. Rev. B* 23 (1981) 823.

- [181] D.J. Ostra and A.E. DeVries, Nucl. Instr. Methods B 18 (1987) 618.
- [182] H.F. Winters and J.W. Coburn, J. Vacuum Sci. Technol. B 3 (1985) 1377.
- [183] R.A. Haring, A. Haring, F.W. Saris and A.E. de Vries, Appl. Phys. Letters 41 (1982) 174.
- [184] A.W. Kolfchoten, R.A. Haring, A. Haring and A.E. de Vries, J. Appl. Phys. 55 (1984) 3813.
- [185] M.S. Ameen and T.M. Mayer, J. Appl. Phys. 63 (1988) 1152.
- [186] B.H. Mahan, in: *Interactions Between Ions and Molecules*, Ed. P. Ausloos (Plenum, New York, 1975) p. 75.
- [187] J.C. Tully, J. Chem. Phys. 73 (1980) 6333, 1975.
- [188] G. Ertl, CRC Crit. Rev. Solid State Mater. Sci. 10 (1982) 349.
- [189] C. Weissmantel, in: *Thin Films From Free Atoms and Particles*, Ed. K.J. Klabunde (Academic Press, Orlando, FL, 1985) ch. 4.
- [190] T. Takagi, Thin Solid Films 92 (1982) 1.
- [191] J.H. Freeman, in: *Ion Implantation*, Eds. G. Dearnaley, J.H. Freeman, R.S. Nelson and J. Stephen (North-Holland, Amsterdam).
- [192] S.R. Kasi, Y. Lifshitz, J.W. Rabalais and G. Lempert, Angew. Chem. 100 (1988) 1245.
- [193] J.H. Freeman, in: *Proc. Intern. Conf. on Applications of Ion Beams to Semiconductor Technology*, Grenoble, 1976, p. 75.
- [194] K. Yagi, K. Miyake and T. Tokuyama, Inst. Phys. Conf. Ser. 38 (1977) 136.
- [195] N. Herbots, B.R. Appleton, T.S. Noggle, R.A. Zuhr and S.J. Pennycook, Nucl. Instr. Methods B 13 (1986) 250.
- [196] J.H. Freeman, W. Temple and G.A. Gard, Vacuum 34 (1984) 305.
- [197] G.E. Thomas, L.J. Beckers, J.J. Vrakking and B.R. DeKoning, J. Crystal Growth 56 (1982) 557.
- [198] F. Seitz and J.S. Koehler, in: *Solid State Physics*, Vol. 2, Eds. F. Seitz and D. Turnbull (Academic Press, New York, 1956).
- [199] J. Amano, Thin Solid Films 92 (1982) 115.
- [200] S. Shimizu, O. Tsukakoshi, S. Komiya and Y. Makita, Japan. J. Appl. Phys. 24 (1985) 1130.
- [201] S.R. Kasi, H. Kang and J.W. Rabalais, Phys. Rev. Letters 59 (1988) 75;
J.W. Rabalais and S.R. Kasi, Science 239 (1988) 623.
- [202] E.F. Chaikovskii, V.M. Puzikov and A.V. Semenov, Soviet. Phys. Crystallogr. 26 (1981) 122.
- [203] T. Miyazawa, S. Misawa, S. Yoshida and S. Gonda, J. Appl. Phys. 55 (1984) 188.
- [204] A. Anttila, J. Koskinen, R. Lappalainen, J.P. Hirvonen, D. Stone and C. Paszkiet, Appl. Phys. Letters 50 (1987) 132.
- [205] Y. Lifshitz, S.R. Kasi and J.W. Rabalais, Phys. Rev. Letters, in press.
- [206] B.A. Probyn, J. Phys. D 1 (1968) 457.
- [207] T. Tsukizoe, T. Nakai and N. Ohmae, J. Appl. Phys. 42 (1977) 4770.
- [208] A.E.T. Kuiper, G.E. Thomas and W.J. Schouten, J. Crystal Growth 51 (1981) 17.
- [209] S. Shanfield and R. Wolfson, J. Vacuum Sci. Technol. A 1 (1983) 323.
- [210] R.A. Roy, J.J. Cuomo and D.S. Yee, J. Vacuum Sci. Technol. A 6 (1988) 1621.
- [211] M. Hou and M.T. Robinson, Appl. Phys. 18 (1979) 381.
- [212] J.P. Biersack and W. Eckstein, J. Appl. Phys. A 34 (1984) 73.
- [213] K.H. Muller, Phys. Rev. B 35 (1987) 7906.
- [214] K.H. Muller, Surface Sci. 184 (1987) L375.

Ion Beam Induced Decomposition of Transition-Metal Fluoroanions

C. S. Sass and J. W. Rabalais*

Department of Chemistry, University of Houston, Houston, Texas 77004 (Received: June 12, 1987;
In Final Form: October 21, 1987)

XPS and UPS studies of 4-keV Ar⁺ bombarded K₂TiF₆, K₂NbF₇, and K₂TaF₇ reveal the reduction of the central transition-metal atom to lower oxidation states in all cases. The tantalum and niobium in K₂TaF₇ and K₂NbF₇ are reduced to oxidation states of IV, II, and 0, while the titanium in K₂TiF₆ is reduced to oxidation states of III and II. The various oxidation states are identified through binding energy shifts of the XPS core level spectra. Atomic concentration measurements are used to estimate the surface compositions. These results are discussed in terms of the thermal spike model, and the behavior of the specific compounds is shown to correlate with the relative stability of the possible reaction products.

Introduction

Ion bombardment of a surface deposits large quantities of energy into localized regions near the surface. This energy can induce a variety of processes such as preferential sputtering, dissociation, atomization, and recombination resulting in an altered surface layer.¹⁻³ The momentum transfer collision cascade theory⁴⁻⁶ of sputtering is well developed and provides a good model of ion damage in single-component targets. The mechanism of ion damage in multicomponent targets is not well understood, however.

In this laboratory, salts of complex oxyanions have been used as model systems for the study of ion damage to multicomponent systems. Oxyanions, such as CO₃²⁻, NO₃²⁻, and SO₄²⁻, whose central atom (C, N, S) forms volatile compounds with oxygen were found^{7,8} to become deficient in this central metal atom upon bombardment. In contrast, ion bombardment of oxyanions with metal central atoms, such as Mo₆⁴⁻, where M = Cr, Mo, W, V, Nb, and Ta, which form involatile compounds with oxygen, resulted in preferential loss of oxygen and reduction of the central metal atom to lower oxidation states.⁹⁻¹¹ In some cases, reduction of the central metal atom to oxidation state 0 was observed but not in others. These results were explained according to the thermal spike model of Kelly.¹² This model states that when an ion strikes a surface, a localized high-temperature region is produced, resulting in atomization and fragmentation of the species within this region. As the system relaxes, recombination occurs. Of the numerous decomposition reactions possible in such a process, the model predicts that those with the highest negative free enthalpy of reaction occur with the highest probability. This model successfully predicts the decomposition behavior of the oxyanions studied.

In order to further test the generality of the proposed mechanism, these studies were extended to the ion-induced decomposition of the fluoroanion compounds K₂TaF₇, K₂NbF₇, and K₂TiF₆. In this paper, we present UPS and core XPS spectra of these unbombarded and Ar⁺-bombarded fluoroanion compounds. Both the atomic concentrations (AC) and binding energy (BE) are monitored for all elements such that the composition of the

damaged layer can be quantified. The results are compared to the studies of the corresponding oxyanion compounds and are discussed in terms of the stability of the possible reaction products.

Experimental Section

The XPS measurements in this study were carried out on a Perkin-Elmer PHI Model 550 ESCA/SAM system with Mg Kα X-rays at 1253.6 eV as the excitation source. The base pressure of the instrument is 2 × 10⁻¹⁰ Torr. UPS measurements were performed on the same system with He II radiation at 40.2 eV as the excitation source. Auger measurements were attempted, but it was found that the electron beam readily decomposed the samples.

K₂TiF₆, K₂TaF₇, and K₂NbF₇ (Alfa Products), in the form of fine powders, were pressed into 1 cm × 0.2–0.5 mm disks that were positioned on the sample probe of the instrument. Ion bombardment was performed with 4-keV Ar⁺ ions at a flux of 3 μA/cm². Ion currents were measured on a stainless steel plate with an area equivalent to that of the samples. XPS measurements were made at regular intervals during bombardment until no further changes in the peak shapes or relative atomic concentrations were observed. This saturation condition typically occurred at ion doses of (1.5–1.8) × 10¹⁷ ions/cm². All binding energies were referenced to C 1s at 284.5 eV, which was present as an impurity in all unbombarded samples, or to peaks of the bombarded sample (in which no C remained) that were unchanged by bombardment. UPS measurements were made on the fresh samples and the bombarded samples after the steady-state condition was obtained.

Results

Prior to bombardment of the fluoroanion compounds with 4-keV Ar⁺, XPS survey spectra were taken of the fresh samples. These spectra indicated that each fresh sample was contaminated with a small amount of carbon and oxygen. After bombardment, no trace of either contaminant remained.

The core-level XPS lines of the fluoroanions were monitored before and at various times during ion bombardment. The core lines of the transition metals all showed large chemical shifts upon bombardment. These metal core lines are characterized by spin-orbit (SO) doublets. When more than one oxidation state was present on the surface, the overlapping SO doublets of the various oxidation states yielded a rather complex peak shape. The peaks were curve fit by using (i) the relative intensities of the SO components, (ii) the SO splitting, and (iii) the known binding energies of the various oxidation states.^{11,13} A more detailed description of the curve-fitting procedure has been given previously.¹¹

(1) Christie, A. B.; Sutherland, I.; Lee, J.; Walls, J. M. *Vacuum* 1981, 31, 513.

(2) Coyle, G. J.; Tsang, T.; Alder, I.; Ben Zui, N.; Yim, I. *J. Electron Spectrosc.* 1981, 24, 221.

(3) Coyle, G. J.; Tsang, T.; Alder, I.; Yim, I. *Surf. Sci.* 1981, 112, 197.

(4) Sigmund, P. *Phys. Rev.* 1969, 184, 383; *J. Mater. Sci.* 1973, 8, 1545.

(5) Anderson, N.; Sigmund, P. *K. Dan Vidensk. Selsk. Mat.-Fys. Medd.* 1974, 3, 39.

(6) Winters, H. F. *Adv. Chem. Ser.* 1976, 158, 1.

(7) Contarini, S.; Rabalais, J. W. *J. Electron Spectrosc. Relat. Phenom.* 1985, 35, 191.

(8) Aduru, S.; Contarini, S.; Rabalais, J. W. *J. Phys. Chem.* 1986, 90, 1683.

(9) Contarini, S.; Aduru, S.; Rabalais, J. W. *J. Phys. Chem.* 1986, 90, 3202.

(10) Ho, S. F.; Contarini, S.; Rabalais, J. W. *Chem. Phys. Lett.* 1987, 133, 171.

(11) Ho, S. F.; Contarini, S.; Rabalais, J. W. *J. Phys. Chem.* 1987, 91, 4779.

(12) Good-Zamin, C. J.; Shehata, M. J.; Squires, D. B.; Kelly, R. *Radiat. Eff.* 1978, 35, 139.

(13) Hofmann, S.; Sanz, J. M. *J. Trace Microprobe Tech.* 1982-83, 1, 213.
Cimino, A.; Angelis, B. A. *J. Catal.* 1975, 36, 11.
Himpsel, F. J.; Morar, J. F.; McFeely, F. R.; Pollak, R. A.; Hollinger, G. *Phys. Rev. B: Condens. Matter* 1984, 30, 7236.
Fontaine, R.; Caillate, R.; Feve, L.; Guillet, M. J. *J. Electron Spectrosc. Relat. Phenom.* 1977, 10, 349.
Rao, C. N. R.; Sarma, N.; Vasudevan, S.; Hegde, M. S.; *Proc. R. Soc. London*, 4 1979, 367, 239.
Sasaki, T.; Williams, R. S.; Wong, J. S.; Shirley, D. A. *J. Chem. Phys.* 1978, 69, 4374.

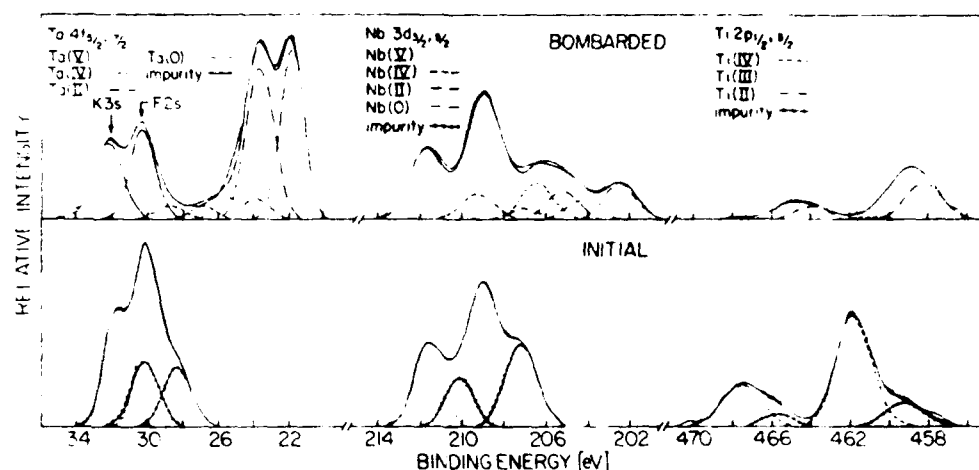


Figure 1. XPS spectra of the transition-metal core lines of K_2TaF_7 , K_2NbF_7 , and K_2TiF_6 before and after Ar^+ bombardment to the steady-state condition. The impurity observed on the initial surfaces is due to hydrolysis products such as K_2TaOF_4 , $KNbOF_4$, and K_2TiOF_4 .

TABLE I: Binding Energies (in eV) and Atomic Concentrations for K_2TaF_7 , K_2NbF_7 , and K_2TiF_6 before and after 4-keV Ar^+ Bombardment to a Steady-State Condition

	initial		bombarded	
	BE	AC	BE	AC
K_2TaF_7				
K $2p_{3/2}$	292	0.21	292	0.18
F $1s$	687	0.68	687	0.62
Ta $4f_{7/2}$ (V)	30.0	0.07		
Ta $4f_{7/2}$ (IV)		0	26.7	0.02
Ta $4f_{7/2}$ (II)		0	23.7	0.02
Ta $4f_{7/2}$ (0)		0	21.7	0.16
impurity	28.4	0.04		
K_2NbF_7				
K $2p_{3/2}$	293	0.22	293	0.18
F $1s$	686	0.69	686	0.64
Nb $4f_{7/2}$ (V)	208.9	0.06	208.8	0.09
Nb $4f_{7/2}$ (IV)			206.4	0.03
Nb $4f_{7/2}$ (II)			204.3	0.01
Nb $4f_{7/2}$ (0)			202.4	0.03
impurity	207.2	0.04		
K_2TiF_6				
K $2p_{3/2}$	292	0.23	292	0.19
F $1s$	686	0.68	686	0.63
Ti $3p_{3/2}$ (IV)	461.8	0.07	461.2	0.01
Ti $3p_{3/2}$ (III)			459.4	0.07
Ti $3p_{3/2}$ (II)			458.1	0.09
impurity	459.4	0.02		

A. K_2TaF_7 . The core-level binding energies and atomic concentrations of K_2TaF_7 before and after ion bombardment are listed in Table I. Examples of the corresponding XPS spectra of the Ta $4f$ levels are shown in Figure 1. The initial K_2TaF_7 surface was found to contain approximately 5 atom % each of carbon and oxygen impurities. The Ta $4f$ peaks of K_2TaF_7 at 30.0 and 31.85 eV overlapped with the K $3s$ and F $2s$ peaks at 32.1 and 30.1 eV, respectively, making deconvolution of the individual peaks difficult. Therefore, in the curve fitting of the initial surface, the K $3s$ and F $2s$ peaks were omitted. This makes the reported atomic concentrations and binding energies of the initial surface an upper limit. Curve fitting of the Ta $4f$ region revealed a SO doublet due to Ta(V) in K_2TaF_7 and a second SO doublet at 1.5 eV lower energy. K_2TaF_7 can hydrolyze to form species such as K_2TaOF_4 and $K_2TaO_2F_2$. These species, while still Ta(V), will have lower binding energies due to the lower electronegativity of oxygen than fluorine. The surfaces of these samples were likely hydrolyzed during their preparation and handling. These lower energy components are therefore assigned to hydrolysis products. It should be noted that no oxygen-containing species was detectable after Ar^+ bombardment to the steady state. These surface oxygen-containing species were totally removed after an ion dose of approximately 5×10^{18} ions/cm². The relative atomic concentrations

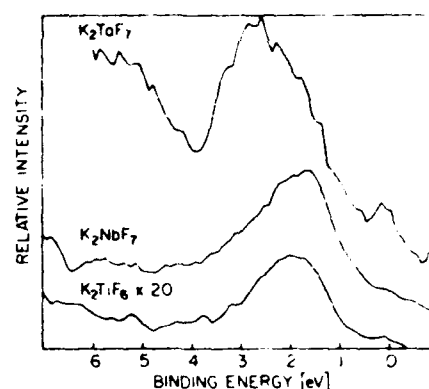


Figure 2. Difference UPS spectra of K_2TaF_7 , K_2NbF_7 , and K_2TiF_6 obtained by subtracting the initial UPS spectrum from the UPS spectrum obtained after Ar^+ bombardment to the steady-state condition.

and binding energies of the bombarded samples are the steady-state values. These values are obtained and persist long after the oxygen-containing impurities have been sputtered away. Therefore the steady-state values reflect the decomposition of the K_2TaF_7 and are not influenced by the hydrolyzed surfaces.

Upon Ar^+ bombardment, the Ta $4f$ region shifts to two major peaks at 21.7 and 23.6 eV with a low-intensity tail to higher binding energy. By use of the curve-fitting method previously described, this band shape can be shown to consist of three overlapping SO doublets corresponding to formal oxidation states of 0, II, and IV. The Ta(0) peaks are particularly prominent, comprising greater than 80% of the total Ta $4f$ intensity, indicating that the Ta is primarily reduced to the metallic state.

The UPS spectrum exhibits similar changes upon ion bombardment. Figure 2 is the difference spectrum obtained when the UPS spectrum of the fresh sample is subtracted from the UPS spectrum of the irradiated sample. The new peak at 3 eV is due to ionization of the Ta $5d$ band, which is now occupied in the reduced metal. This binding energy agrees very well with the Ta $5d$ band in sputtered films.¹⁴

Both fluorine and potassium are preferentially lost upon bombardment. The Ta/F and Ta/K ratios increased from 0.16 and 0.52 to 0.32 and 1.11, respectively.

B. K_2NbF_7 . The initial surface contained K_2NbF_7 along with rather substantial amounts of hydrolysis products such as $KNbOF_4$ or $KNbO_2F_2$. Upon Ar^+ ion bombardment the Nb $3d$ region broadens into a structure characteristic of several overlapping SO doublets. Curve fitting shows this structure to consist of four overlapping doublets corresponding to oxidation states of 0, II, IV, and V as is shown in Figure 1. The binding energies and

(14) Penchina, C. M. *Phys. Rev. B: Solid State* 1976, 14, 4407.

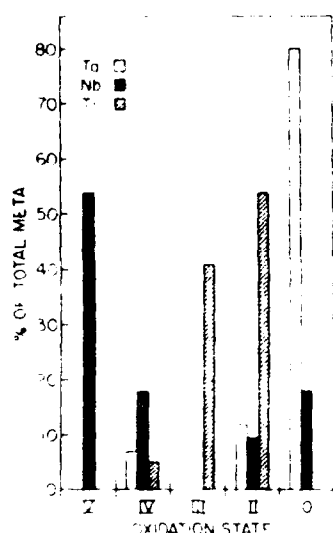


Figure 3. Plot of the distribution of the various oxidation states of the transition metals following 4-keV Ar^+ bombardment to saturation.

relative atomic concentrations are listed in Table I. The UPS spectrum showed a growth of the Nb 4d band indicating reduction of the central atom as shown in Figure 2.

C. K_2TiF_6 . The initial surface contained primarily K_2TiF_6 with small amounts of hydrolysis products such as K_2TiOF_4 and $\text{K}_2\text{TiO}_2\text{F}_2$.¹⁶ After ion bombardment, SO doublets due to oxidation states IV, III, and II were observed in the Ti 3p region. No reduction to the metallic state was observed. Representative spectra are shown in Figure 1, and binding energies and atomic concentrations are listed in Table I. The UPS spectrum was similar to that of the Ta and Nb fluoroanion compounds, showing a growth of the Ti 3d band upon bombardment; however, it was of much lower intensity. The 3d orbitals of Ti(II) and -(III) are partially occupied, giving rise to the valence band structure shown in Figure 2.

Discussion

The results indicate that all of the fluoroanions decompose under ion bombardment and that the composition of the decomposed layer reaches a steady state after which additional ion bombardment causes no further changes in the system detectable by XPS or UPS. While the specific decomposition product distributions vary widely between compounds, there are several changes that are common to all of the samples: (i) the relative concentration of the central transition metal increases while the concentrations of the potassium and fluorine decrease and (ii) lower oxidation states of the central metal atom are produced. This behavior is similar to the decomposition behavior of transition-metal oxyanions.^{10,11} The relative abundances of the various oxidation states of the metal in the bombarded sample are shown in Figure 3.

The most outstanding feature observed in the decomposition of the fluoroanion compounds is the fact that the central metal atom is reduced to the metallic state in K_2TaF_7 and K_2NbF_7 but not in K_2TiF_6 . This behavior also correlates well with decomposition of the oxyanion compounds.¹¹ Oxyanions of first-row transition metals were not reduced to oxidation state 0 upon ion bombardment, while those of the second- and third-row transition metals were reduced to 0. This close correlation of the decomposition of the fluoroanion and oxyanion compounds strongly suggests a similar mechanism for these decompositions.

Decomposition of the oxyanion compounds has been successfully described by the thermal-spike model. Ion beams can transfer

both translational and electronic energy into localized regions near a crystalline surface. Seitz and Koehler¹⁷ give an expression for a particle of energy E , striking a surface of thermal conductivity K , heat capacity C , and density ρ . The temperature T at a distance r from the site after a time t is given by

$$T = E(C\rho)^{1/2} / [8(\pi K t)^{3/2} \exp\{-C\rho r^2/4Kt\}] \quad (1)$$

For a 4-keV Ar^+ ion striking a salt, typical of those studied herein, a region of radius 20 Å can be elevated to a temperature of greater than 3000 K. This condition persists for 10^{-10} s, which is orders of magnitude longer than the vibrational periods of the surface species. The high energy density in the thermal-spike region causes ionization, dissociation, and atomization of the surface species. Translational energy acquired by the constituents through collision cascades and attractive or repulsive electrostatic potentials results in ejection of some particles and random collisions between others. As the system relaxes, recombination reactions between atoms and molecular fragments occur. The resulting decomposition products remaining on the surface are nonvolatile species with high negative free energies of formation. Products with high vapor pressures or high negative free energies of formation are typically lost to vacuum. This is not to imply that a quasi-equilibrium situation is attained during sputtering but that thermodynamics only governs the probability of a compound forming upon relaxation.

Kelly¹² has shown that the decomposition of metal oxides upon ion bombardment can be explained in terms of the thermal-spike model. Ho et al.¹³ have extended this treatment to three-component oxyanion compounds. They observed that those decomposition reactions with the largest negative free energy of reaction tended to have the highest probability of occurring. The similarity of this oxyanion work to the decomposition of the fluoroanion compounds indicates that a similar mechanism is involved. Unfortunately, since the required thermodynamic data are not available for the fluoroanion compounds, a rigorous treatment is not possible. However, the stability of the possible products can be examined.

Compounds of the first-row transition metals with oxidation states of II and III are well-known and are stable in the solid state.¹⁸ However, lower oxidation states in second- and third-row transition metals tend to be unstable and do not play a major role in their chemistry. As the thermal spike relaxes, stable nonvolatile products with large free energies of formation are formed and remain on the surface. Thermodynamics governs the probability that a species will be formed upon relaxation. Thermodynamically favorable reaction channels resulting in transition-metal compounds with oxidation states of II and III are more likely for first-row transition metals such as Ti than for second- and third-row metals such as Nb or Ta. Therefore, K_2TiF_6 should have thermodynamically favorable decomposition channels which do not result in the reduction of the Ti all the way to the metal. K_2NbF_7 and K_2TaF_7 , on the contrary, are less likely to have favorable decomposition channels resulting in oxidation states II or III; therefore, reduction to the metal is favored, especially for K_2TaF_7 . Therefore, while there are insufficient data to prove that the decomposition of the fluoroanion compounds is governed by the thermal-spike model, the data are certainly consistent with this model.

While the observed reduction of the fluoroanions is consistent with the thermal-spike model, some mention should be made of alternate models of ion-induced decomposition. Kelly¹⁹ has pointed out that thermal sputtering can be equally well described as a surface binding energy effect, i.e., that those atoms with a lower surface binding energy are preferentially lost over those with a higher binding energy. For metal oxides, the metal atom has a much higher surface binding energy than the oxygen due to its

(17) Seitz, J.; Koehler, J. E. *Progress in Solid State Physics*, 2; Academic: New York, 1957; p 30.

(18) Cotton, F. A.; Wilkinson, G. *Advanced Inorganic Chemistry*, 4th ed.; Wiley-Interscience: New York, 1980.

(19) Kelly, R. *Nucl. Instrum. Methods* 1987, B35, 358; Kelly, R. *J. Vac. Sci. Technol.* 1982, 20, 778.

(15) Lastockina, A. A.; Shika, I. A.; Malinko, I. A. *Izv. Akad. Nauk SSSR, Neorg. Mater.* 1969, 5, 157.

(16) Skyadnev, Yu. N.; Mikhailov, M. A. *J. Less Common Met.* 1971, 25, 336.

greater charge. This should be even more exaggerated for metal halides or metal fluoroanions. Therefore, ion bombardment of fluoroanions should induce preferential loss of F and a subsequent reduction of metal atom, which is observed. Both models predict the general behavior of the decomposition of the fluoroanions. However, due to the unreliability of surface binding energies for complex species, the thermal-spike model can be more easily applied in these complex systems.

Conclusions

All of the transition-metal fluoroanion compounds studied preferentially lost potassium and fluorine upon Ar^+ bombardment,

while the central metal atom was reduced to lower oxidation states. Reduction to the metal was observed for K_2TaF_7 and K_2NbF_7 , but not for K_2TiF_6 . These results are consistent with the thermal-spike model of energy dissipation. The resulting surface contains those products with high negative free energies of formation.

Acknowledgment. This material is based on work supported by the Air Force Research Office under Contract No. F19628-86-K-0013 and by the R. A. Welch Foundation under Grant E656.

Registry No. K_2TiF_6 , 16919-27-0; K_2TaF_7 , 16924-00-8; K_2NbF_7 , 16924-03-1; Ar^+ , 14791-69-6.

SURFACE SCIENCE LETTERS

**CHEMISORPTION OF CARBONYL SULFIDE (OCS) ON Ni
BETWEEN 77 AND 293 K**

Craig S. SASS and J. Wayne RABALAIS

Department of Chemistry, University of Houston, Houston, TX 77006, USA

Received 8 September 1987, accepted for publication 23 October 1987

The chemisorption of OCS on polycrystalline Ni foil, in the 77–293 K temperature range, was investigated by XPS, UPS and AES electron spectroscopies. At all temperatures studied, chemisorption was found to be dissociative yielding adsorbed S and gas phase CO. The reaction is found to be strongly exothermic with a low activation energy.

Little work has been done on the chemisorption behavior of carbonyl sulfide (OCS) on transition metal surfaces such as nickel. Such systems are of interest due to the variety of processes that can occur, ranging from molecular chemisorption to dissociative chemisorption with one or more of the products being desorbed from the surface. In the only previous work on this system, Saleh et al. [1] studied the adsorption of OCS on evaporated Ni films. By monitoring the change in pressure of OCS over the Ni film and the composition of the residual gas after adsorption, it was concluded that OCS dissociates upon adsorption at temperatures above 293 K, yielding adsorbed S and gas phase CO. This is similar to the dissociative chemisorption of CO₂ on Ni, which yields chemisorbed O atoms and molecular CO [2]. In contrast, at temperatures below 293 K, Saleh et al. reported the adsorption to be primarily molecular. Their work did not attempt to characterize the surface species after chemisorption, which is important for a complete understanding of the adsorption process. This Letter reports the characterization of the surface species following OCS chemisorption on Ni foil by XPS, UPS and Auger spectroscopies in the temperature range of 77–293 K.

The XPS and UPS measurements were carried out on a Perkin Elmer PHI Model 550 ESCA/SAM system using 1253.6 eV Mg K α X-rays and 40.2 eV He II radiation, respectively, as the excitation sources. Auger measurements were carried out on the same system using a 3 keV, 1 μ A electron beam as the excitation source. A polycrystalline Ni foil (Alfa Inorganics) which was mechanically polished before insertion into the vacuum chamber was used for the sample. This sample was cleaned in vacuum by simultaneously heating to

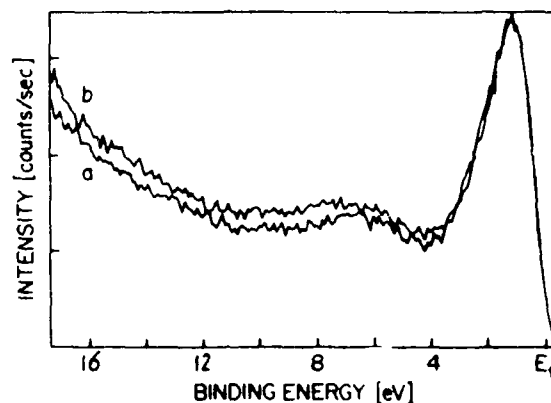


Fig. 1. He II UPS spectrum of a clean (a) Ni surface and after exposure to 5000 L OCS (b) at 293 K.

550°C and sputtering with 5 keV Ar⁺ for periods up to eight hours. In the "clean" surface condition, the C KLL, O KLL and S LMM Auger peak-to-peak amplitudes were all less than 0.1% of the Ni LMM peak-to-peak amplitude. The sample was cooled by flowing cold N₂ gas or liquid N₂ through a tube in thermal contact with the sample. The temperature of the sample was monitored by means of a thermocouple spot-welded to the sample holder. In a typical experiment, the sample was cooled to the desired temperature, a known dose of OCS was admitted into the vacuum chamber, and UPS, XPS and Auger spectra were measured on the resulting surface. Auger spectra were measured after the XPS and UPS measurements to insure that any electron beam effects did not alter the photoelectron results. The sample was cleaned after each exposure.

XPS, UPS and Auger measurements were made on the clean Ni surface. All spectra agreed with literature spectra [3,4]. Chemisorption experiments were run at exposures of OCS ranging from 0.1 to 5000 L.

The UPS spectra obtained from the clean surface and following 5000 L exposure of OCS to the polycrystalline Ni sample at 293 K are shown in fig. 1. The clean Ni surface exhibits an intense d-band plus a small plasmon loss feature centered at 6 eV below the Fermi level. After chemisorption of OCS, the only change in this spectrum is a slight increase in the inelastic electron loss intensity. To our knowledge, no one has reported the UPS spectrum of OCS absorbed on a metal surface. The gas phase UPS and XPS spectra of OCS have intense valence bands at ionization potentials (IP) of 10.1 and 15.5 eV corresponding to ionization of the 3 π and 2 π molecular orbitals, respectively [5,6]. It would be expected that absorbed molecular OCS on Ni would have similar bands, although possibly with shifted energies. The gas phase IP's

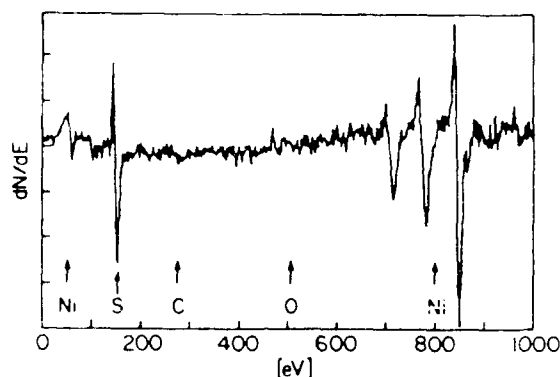


Fig. 2. Auger spectrum of a Ni surface after exposure to 5000 L OCS at 293 K.

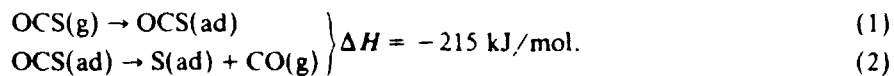
of these bands correspond to binding energies of 4.8 and 10.2 eV below the Fermi level of Ni. No peaks are observed in these regions, indicating that no molecular OCS is present on the Ni surface.

The absence of molecular OCS indicates that this species undergoes dissociation upon adsorption. The feasible decomposition products include C, O, S and molecular CO. No molecular CO remains on the surface as indicated by the absence of bands at 8.1 and 10.9 eV due to the 4σ and a combination of the 5σ and 1π molecular orbitals, respectively [7,8]. No atomic species are observable in the UPS spectrum either. The C 2p, O 2p, and S 3p ionizations are typically near 3.6, 6, and 5 eV, respectively [4,9,10]. These are not observed because of the low surface coverage, the overlap with the Ni plasmon peak, and the low photoionization cross section with He II radiation (particularly so for C 2p and S 3p orbitals). It has been shown [4] that monolayer coverage of C on Ni is not detected by grazing incidence UPS. The lack of observation of any valence atomic orbitals in the UPS spectrum is, in itself, not sufficient evidence that these species are not present. The atomic species present on the surface can be readily observed in the Auger spectrum shown in fig. 2. An intense peak at 152 eV due to the S LMM transition is observed while no transitions due to C or O are detectable. Similar results are obtained by XPS, i.e. an intense S 2p peak but no O 1s or C 1s peaks are observed.

Similar chemisorption experiments were performed at sample temperatures of 200 and 77 K. In each case, exposure of the Ni surface for up to 5000 L of OCS resulted in identical spectra to those at 293 K, indicating that an identical process is occurring.

The spectra show that OCS decomposes upon chemisorption at all temperatures between 77 and 293 K. The absence of C and O on the surface after chemisorption suggests that C and O are desorbing as molecular CO. The most likely reaction involves chemisorption of the OCS by formation of a metal-S

bond. Electron transfer from the metal weakens the S-C bond, resulting in efficient bond rupture and desorption of molecular CO. The overall process is then:



The bond energy of chemisorbed S on alumina supported Ni has been measured to be 465 kJ/mol between 600 and 800 K [11]. Assuming that the bond energy is similar for polycrystalline Ni at room temperature, the heat of formation of chemisorbed sulfur from standard states is approximately -242 kJ/mol. This value is similar to that estimated by Roberts [12] from the heat of formation of NiS. Using this value and the standard heats of formation of OCS(g) and CO(g), the total reaction is calculated to be exothermic by 215 kJ/mol at 293 K. The similar results obtained at 200 and 77 K indicate that the same process is occurring at these lower temperatures. The fact that the decomposition reaction occurs at such low temperatures indicates that the activation barrier for the process is very low. The formation of the metal-sulfur bond must sufficiently weaken the S-C bond to allow bond rupture at temperatures as low as 77 K. This process is aided by a strong thermodynamic driving force.

These results are in contrast to the work of Saleh et al. who found that chemisorption of OCS on evaporated Ni films was molecular at temperatures below 293 K. One possible explanation for this may be the different surface structures of polycrystalline Ni foil and evaporated Ni films. Both the polycrystalline foils and evaporated films have a distribution of different crystallographic faces at the surface. However, the types of faces and their distributions may be different for the different methods of fabrication. The reactivity of OCS on Ni may be a function of the surface structure and therefore may be more reactive on the Ni foils than on the evaporated films. The determination of the role of surface structure on the decomposition of OCS on Ni will require a systematic investigation of the chemisorption on a number of Ni single crystal faces.

OCS was found to decompose upon chemisorption on polycrystalline Ni at temperatures between 77 and 293 K. The decomposition reaction involves cleavage of the C-S bond followed by desorption of molecular CO. The fact that the reaction occurs at such low temperatures implies a low activation barrier for the process.

References

- [1] J.M. Saleh and F.A.K. Nasser, *J. Phys. Chem.* 89 (1985) 3392.
- [2] G.A. Martin, M. Primet and J.A. Dalmon, *J. Catalysis* 53 (1978) 321.

- [3] C.D. Wagner, W.M. Riggs, L.E. Davis, J.F. Moulder and G.E. Muilenberg, Handbook of X-ray Photoelectron Spectroscopy (Perkin-Elmer, Eden Prairie, MN, 1979);
L.E. Davis, N.C. MacDonald, P.W. Palmberg, G.E. Riach and R.E. Weber, Handbook of Auger Electron Spectroscopy (Perkin-Elmer, Eden Prairie, MN, 1978).
- [4] H. Kang, T.R. Schuler and J.W. Rabalais, Chem. Phys. Letters 128 (1986) 348.
- [5] A.W. Potts and T.A. Williams, J. Electron Spectrosc. Related Phenomena 3 (1974) 3.
- [6] C.J. Allen, U. Gelius, D.A. Allison, G. Johansson, H. Siegbahn and K. Siegbahn, J. Electron Spectrosc. Related Phenomena 1 (1972) 131.
- [7] D.E. Eastman and J.K. Cashion, Phys. Rev. Letters 27 (1971) 1520.
- [8] C.R. Brundle, J. Vacuum Sci. Technol. 11 (1974) 212.
- [9] H.D. Hagstrum and G.E. Becker, Proc. Roy. Soc. A331 (1972) 395.
- [10] R.C. Cinti and T.T.A. Nguyen, Surface Sci. 68 (1977) 566.
- [11] J.G. McCarty and H. Wise, J. Chem. Phys. 72 (1980) 6332.
- [12] M.W. Roberts, Nature 188 (1960) 1020.

Dissociative scattering of 1.5–4.5 keV N_2^+ and N^+ on gold and graphite surfaces

C. S. Sass and J. W. Rabalais

Department of Chemistry, University of Houston, Houston, Texas 77004

(Received 18 April 1988; accepted 31 May 1988)

Scattering of molecular nitrogen ions in the 1.5–4.5 keV range from gold and graphite surfaces results in a small fraction of surviving molecules and molecular ions in addition to atoms and atomic ions resulting from dissociation. The kinetic energy (E_k) distributions of scattered N_2^+ and N^+ ions have been measured directly by means of an electrostatic sector analyzer (ESA) and the velocity distributions of the scattered N_2 and N neutrals plus ions have been measured by time-of-flight (TOF) techniques. Scattered ion fractions were determined from the TOF measurements. The relative E_k distributions of the scattered atomic ions indicate that dissociation from excited repulsive electronic states which are populated during the collision dominate the mechanism, rather than purely vibrational or rotational excitation from the $X^2\Sigma_g^+$ ground state of N_2^+ . The excited dissociative $C^2\Sigma_u^+$ and $D^2\Pi_u$ states of N_2^+ are accessible by Franck-Condon transitions from the $X^2\Sigma_g^+$ state. The data are consistent with a mechanism in which these two dissociative states contribute their repulsive energy to the large relative E_k distributions of the scattered N^+ ions. The electronic excitation occurs via electron promotion during the scattering collision through the Fano-Lichten mechanism.

I. INTRODUCTION

The interaction of keV diatomic ions with surfaces has received a great deal of interest in recent years. When diatomic ions are scattered from surfaces, the scattered flux consists of surviving molecular species in addition to atomic species resulting from dissociation. Most of the work has been concentrated on H_2^+ scattering.^{1–5} At scattering energies up to several keV, small molecular ion fractions ($\leq 5\%$) survive the collisions, even though the elastic losses to the surface are much larger than the bond energy of the molecular ion.

Extension to heavier diatomic ions has been confined primarily to N_2^+ .^{6–12} Balashova *et al.*^{8,9} have found that some N_2^+ survives even at collision energies up to 30 keV and also noted a strong directional dependence to the scattered N_2^+ flux. Heiland and Taglauer¹⁰ have observed that molecular ion survival is strongly dependent on the surface conditions for N_2^+ scattering from Ni at a primary ion energy of 400 eV and scattering angle of 20° . The molecular ion yield was found to increase by a factor of 2 for scattering from a nitrided Ni(110) surface as compared to the clean or sulfur covered surface. They attributed this to more effective vibrational quenching of the scattered N_2^+ by surface N than by Ni or S.

Betenski and Parilis^{11,15} have developed a model to simulate the survival of molecular ions which treats the constituent atoms in the molecular ion as separate entities. They found that when the molecular axis of the ion is oriented along the direction of incidence of the primary beam, the constituent atoms in the molecule scatter with relative kinetic energies (E_k) of the atoms less than the bond energy of the molecular ion. This results in associative or molecular scattering. Molecular dynamics simulations by Jakas and Harrison¹⁶ have found that scattering of the constituent atoms cannot be treated separately, but that target atom recoil and

internuclear interactions play an important role in the survival of the molecular ion. Both of these approaches treat the dissociation as a classical process and neglect the role of electronic excitation in the dissociation mechanism.

In later work, Heiland *et al.* have studied both the scattered neutrals and ions resulting from N_2^+ bombardment by TOF spectrometry.^{10,12} They found that the scattered flux from 400 eV N_2^+ bombardment of Ni(111) results in primarily neutral N_2 scattering with smaller amounts of neutral atomic N. They attribute these results to resonant charge transfer from the surface to the N_2^+ on the incoming and outgoing trajectories. Transfer to a bound state of N_2 results in neutral associative scattering while transfer to an antibonding state results in dissociative scattering. This work proved that electronic excitation plays an important role in the collisional induced dissociation mechanisms of molecular ions, resulting in neutral molecular and atomic scattering, in contrast to the proposed mechanism of Parilis.^{13–15} It is not clear, however, if excited states play a role in the mechanisms leading to scattered molecular and atomic ions.

We have studied the scattering processes of molecular N_2^+ ions from gold and graphite surfaces in order to determine the role of excited electronic states in the collisional dissociation process. By measuring the energies of the scattered ions directly through an electrostatic analyzer (ESA), the velocities of the scattered neutrals and ions by time-of-flight (TOF) methods, and the scattered molecular and atomic ion fractions, it is possible to assess the role of electronic excitation into excited states in the dissociation mechanism.

II. EXPERIMENTAL

The experiments were performed on a TOF ion scattering spectrometer described previously¹⁷ with the following modification. The flight tube at 22° scattering angle was re-

placed by a 127° electrostatic analyzer (ESA) equipped with a grid window allowing a line-of-sight 1.5 m flight path directly through the ESA. This arrangement allowed the energy spectra of the scattered ions to be measured with the ESA or the TOF spectrum of the scattered neutrals and ions to be measured through the flight tube. Operational details have been described previously.^{17,18} Briefly, molecular N_2^+ ions were formed in a colutron ion source, accelerated to 1.25–4.50 keV, and transported through a beam line equipped with a Wien filter for mass selection, an off-axis aperture for elimination of fast neutrals, and pulse plates for producing a pulsed ion beam of width ~ 100 ns. The resulting mass and energy selected ion beam was directed into a UHV chamber for scattering from the sample surface. The scattered flux was then energy or velocity analyzed.

The energy spectra of scattered ions were measured by means of the ESA using an unpulsed primary ion beam of $\sim 0.1 \mu\text{A}/\text{cm}^2$. The identities of the individual peaks in the resulting energy spectra were confirmed by pulsing the primary ion beam and measuring TOF spectra through the ESA, with the ESA set at a specific energy to pass the peak of interest. From the known path length through the ESA, the velocity corresponding to each peak in the energy spectrum can be determined. Since both the energies and velocities are measured from such TOF-ESA spectra, the masses of the scattered ions can be unambiguously determined.

TOF spectra of scattered neutrals plus ions ($N + I$) were obtained by pulsing the ion beam (average current 0.2–1.0 nA/cm²) and measuring the flight times of the scattered species through a flight path of 150 cm using conventional timing and pulse counting techniques which have been described previously.¹⁸ Neutral (N) only spectra were obtained by deflecting the scattered ions with a deflector voltage plate placed beside the flight path. Spectra of ($N + I$) and (N) were collected in alternating 20 s cycles into different groups of a multichannel pulse height analyzer by switching the deflector voltage on and off. Ion fractions were determined as $\{(N + I) - (N)/(N + I)\}$.

The polycrystalline gold (Alfa) and graphite (Union Carbide) samples were mechanically polished before insertion into the scattering chamber. The samples were cleaned in vacuum by Ar^+ sputtering and annealing to 500 °C. The surface cleanliness was checked by Ar^+ TOF direct recoil spectrometry before and after each scattering experiment. Impurity levels of H, C, N and O were all below 10^{-2} monolayer after cleaning. After 20 min of N_2^+ scattering, both surfaces contained approximately 5% of a monolayer of nitrogen due to reactions with the beam. Further experiments indicated that this level of nitrogen had no measurable effect on the ESA or TOF spectra of the scattered N_2^+ .

The ESA was calibrated by scattering Ar^+ at various energies from clean gold. For such ions in the keV range, the binary collision model provides a good description¹⁹ of ion/surface collision dynamics. For a projectile of mass M_0 and energy E_0 scattering from a target atom of mass M_1 , the scattering energy for a quasisingle scattering collision of the primary ion is given by

$$E_s = E_0 [\cos \theta \pm (A^2 - \sin^2 \theta)^{1/2}]^2 / (1 + A)^2, \quad (1)$$

where $A = M_1/M_0$ and θ is the laboratory scattering angle. The ESA was calibrated by assigning the maximum of the scattering peak to the energy E_s given by Eq. (1) for several different values of E_0 .

III. RESULTS

A. Energy spectra

Figure 1 shows an example of energy spectra obtained from 2000 eV N_2^+ scattering from gold and graphite at 22°. Each spectrum exhibits a low intensity peak at high energy and a high intensity peak at low energy. The assignments of the individual peaks can be made by application of the binary collision model. The scattering energy for elastic quasisingle scattering of a nitrogen molecular ion can be approximated by direct application of Eq. (1) for a projectile with $M_0 = 28$. Quasimultiple scattering can be described by repeated application of Eq. (1). Scattering of the atomic ions resulting from dissociation can be approximated as follows: Upon dissociation, the E_s of the incident molecular ion will, on the average, be distributed to the resulting fragments in proportion to the mass of the fragment. Therefore, for N_2^+ dissociation, the scattered atomic ions can be treated, in a first approximation, as incident atomic ions, each with incident kinetic energy of $E_0/2$. Using these procedures, application of Eq. (1) gives the scattering energies for quasisingle (SS) and quasidouble scattering (DS) of the atomic and molecular ions as indicated in Fig. 1. As observed, the high energy peaks occur at approximately the energy expected for DS of N_2^+ from gold or graphite, while the low energy peak occurs

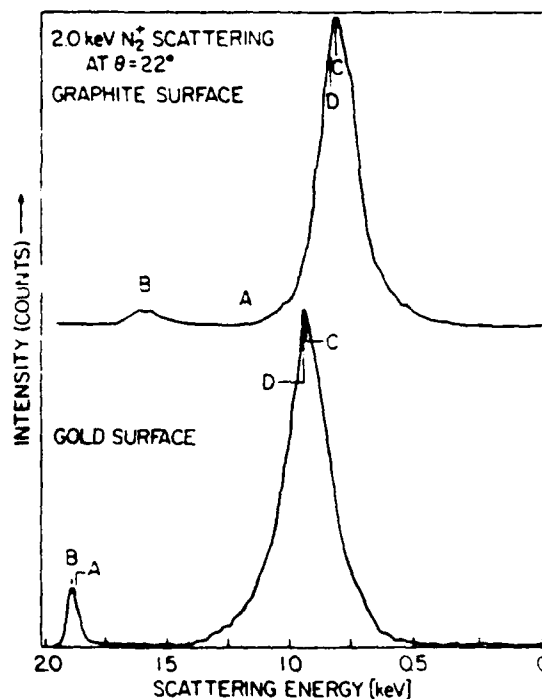


FIG. 1. Positive ion ESA spectra for 2.0 keV N_2^+ scattering from graphite and gold surfaces. The letters represent energies calculated from Eq. (1) for the following cases: (A) 2.0 keV N_2^+ single scattering, (B) 2.0 keV N_2^+ double scattering, (C) 1.0 keV N^+ single scattering, (D) 1.0 keV N^+ double scattering.

at the expected energy for SS of N^+ (with 1/2 of the primary ion energy). Therefore the low energy peak can be assigned to scattered atomic ions resulting from molecular dissociation while the high energy peak can be assigned to surviving molecular N_2^+ . These assignments were confirmed by TOF-ESA measurements. Similar results were obtained at the other primary ion energies and scattering angles employed. The scattering energies obtained experimentally and those calculated from Eq. (1) are shown in Fig. 2. In all cases, the scattered molecular ion peak is near the DS position with no intensity at the SS position. This is not to say that these ions are only the result of distinct DS events. There are a variety of multiple scattering sequences that give rise to scattering energies near that calculated for DS. Note the proximity of the calculated quadruple scattering (QS) energy to the experimental energies for scattering from gold in Fig. 2. These results indicate that the surviving molecular ion is the result of multiple scattering (MS) events rather than SS events. This is reasonable since it is more probable that the molecular ion will survive multiple soft collisions rather than a single hard collision. This result is similar to that obtained for CO^+ scattering from magnesium surfaces.²⁰

Inspection of Fig. 1 also shows that the molecular ion peak is a factor of three broader for N_2^+ scattering from graphite than from gold. This result is expected since N_2^+ transfers much more energy to a light target atom such as carbon than to a heavy target atom such as gold. N_2^+ can transfer a maximum of 37% of its E_k in a collision with a Au atom while it can transfer 72% of its E_k in a collision with a C atom. Therefore, variations in the multiple scattering trajectories (such as double, triple, or quadruple collisions) of N_2^+ will result in a much larger spread in the scattering energies from graphite than from gold surfaces. Since the surviving molecular ions are mainly the result of multiple scattering, a significantly broader molecular ion peak is obtained for scattering from graphite.

While the width of the N_2^+ peak is much greater for scattering from graphite than from gold, the energy spread of the N^+ peak is relatively insensitive to the target. Figure 3 shows the full-width at half maximum (FWHM) of the scattered molecular and atomic ions as a function of primary ion E_k . The N^+ FWHM is approximately the same for scatter-

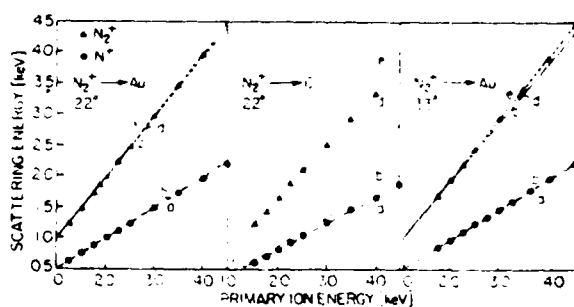


FIG. 2. Primary ion energy dependence of the scattering energies for N_2^+ and N^+ scattering from gold at 22° and 33° and graphite at 22°. Δ and \bullet represent the experimental scattering energies for N_2^+ and N^+ , respectively. The straight lines are scattering energies calculated from Eq. (1) for (a) N^+ SS at $E_k/2$, (b) N^+ DS at $E_k/2$, (c) N_2^+ SS at E_k , (d) N_2^+ DS at E_k , and (e) N_2^+ QS at E_k .

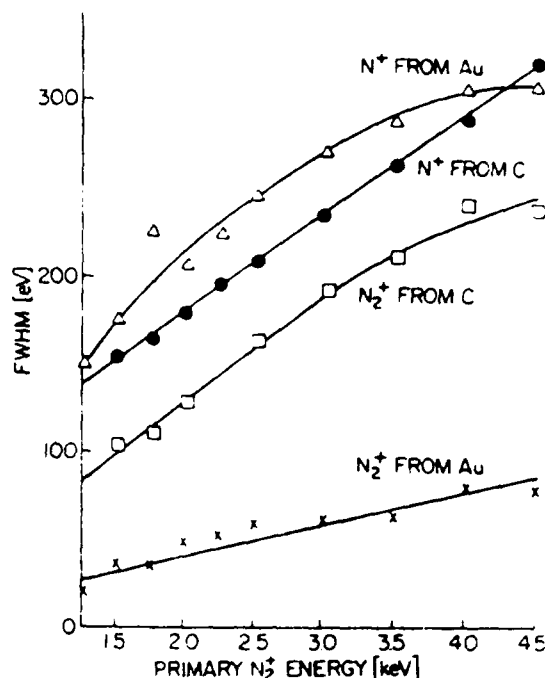


FIG. 3. Full-width at half-maximum (FWHM) of the scattering peaks of N_2^+ and N^+ as a function of primary N_2^+ energy for scattering from gold and graphite at 22°.

ing from Au or C. The energy spread of these peaks is much greater than expected from elastic losses to the surface. For comparison, experiments were performed in which mass-selected N^+ ions with an energy of 2 keV were scattered from the gold surface, resulting in a FWHM of the scattered peak of ~ 80 eV. The 2 keV primary N^+ corresponds to scattered N^+ resulting from dissociation of N_2^+ ions with a primary energy of 4 keV or 2 keV/atom. As observed in Fig. 3, the FWHM of N^+ resulting from 4 keV N_2^+ dissociation is ~ 302 eV. The broader energy distribution of scattered N^+ resulting from N_2^+ dissociation than from primary N^+ scattering indicates that some relative E_k is released to the individual atomic ions by the dissociation process itself. This conclusion is supported by the fact that a large proportion of the scattered atomic ions are of an energy greater than the incident energy/atom. Inspection of Fig. 1 shows that the energy distribution of the scattered atomic ions extends to greater than 1.25 keV, while the incident energy/atom is only 1 keV, indicating that some E_k is imparted to the fragments during the dissociation process. The energy spread of the scattered atomic ion peak is then due primarily to the dissociation process itself. The similar widths of the N^+ peaks resulting from scattering from gold or graphite suggest that similar processes are involved on both target surfaces.

The ratio of surviving molecular ions to atomic ions is shown in Fig. 4. The surviving molecular ion fraction decreases from $\sim 7\%$ at 1.5 keV to $< 1\%$ at 4.5 keV for scattering from both graphite and gold. The similarity of the surviving molecular ion yield from gold and graphite is surprising in that the energy transfer of the projectile to the surface is

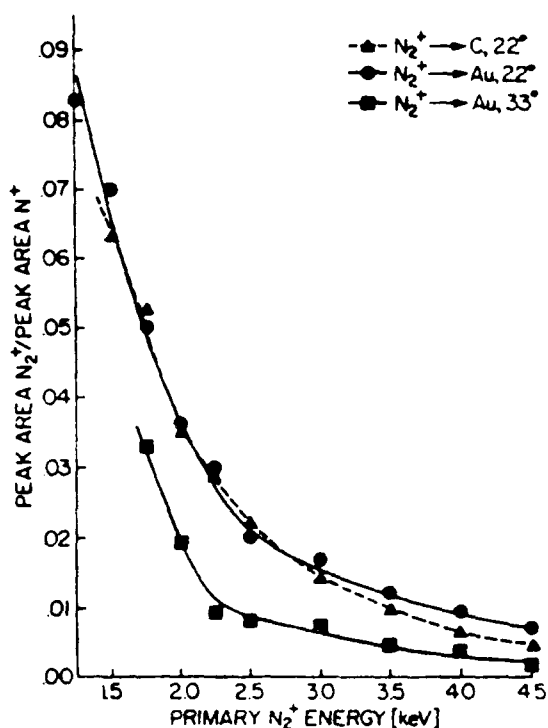


FIG. 4. Ratio of surviving N_2^+ to dissociated N^+ (N_2^+/N^+) as a function of primary N_2^+ energy on gold and graphite surfaces.

much greater from N_2^+ to C atoms than from N_2^+ to Au atoms. Therefore, it would be expected that the molecular ion yield would be lower for scattering from carbon if the dissociation is a purely classical process. The molecular ion yield decreases as expected with increasing scattering angle. Increasing the scattering angle results in harder collisions (smaller impact parameters), therefore lowering the probability of molecular ion survival as has been observed before.⁹

As stated previously, the large energy spread of the scattered atomic ions is due to the release of energy in the dissociation process. Heiland^{9,10,12} has observed a similar broadening of the neutral N scattering peak, resulting from N_2^+ scattering from Ni and attributed it to relative energy released following electron transfer from the surface into an antibonding molecular orbital. When a diatomic ion is excited to an internal energy above the dissociation limit of the ion, the ion dissociates and the excess internal energy is converted to E_k of the resulting fragments. It has been shown by Purser and others^{21,24} that a small release of internal energy to relative E_k , following dissociation in the center of mass system of a fast ion, is amplified in the E_k spread of the resulting fragments in the laboratory system. For dissociation of a homonuclear diatomic ion, the energy released in the center of mass system E_c , is related to the laboratory scattering energy E , by²⁵

$$E_c = \Delta E^2 / 4E^0, \quad (2)$$

where $\Delta E = E^0 \pm E_c$, i.e., the half-width of the peak at E_c values. Here E^0 is the E_c corresponding to the peak maxi-

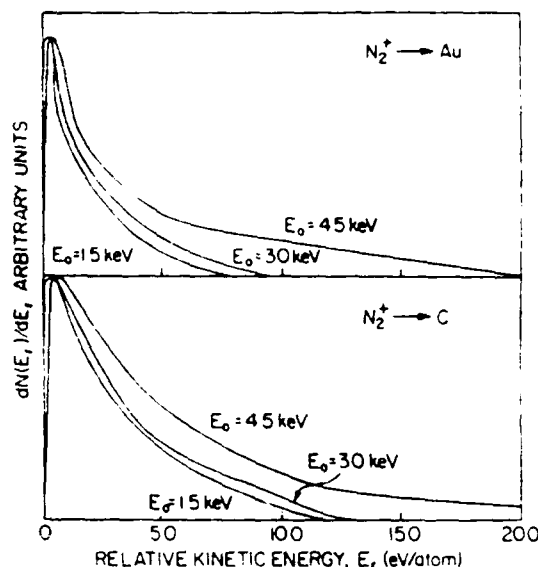


FIG. 5. Relative kinetic energy distributions of the nitrogen atomic N^+ ions resulting from 1.5, 3.0, and 4.5 keV N_2^+ scattering from gold and graphite at $\theta = 22^\circ$.

mum. The laboratory to center of mass transformation was carried out according to the procedure of Gibson and Los.²⁶ Specifically, the energy scale was converted by application of Eq. 2 and the intensity was scaled by

$$N(E_c) = N(E_r)(E_r/E_c), \quad (3)$$

where $N(E_c)$ is intensity in the center of mass system, $N(E_r)$ is intensity in the laboratory system, and (E_r/E_c) is the Jacobian of the transformation. The center of mass energy spectrum, $N(E_c)$ vs E_c , was generated in this manner. The change in scattering intensity $[N(E_c)]$ as a function of E_c was calculated by differentiating the E_r spectrum to produce the E_c distributions of the scattered atomic ions, i.e., $dN(E_c)/dE_c$ vs E_c . The relative energy E_c distributions in the center of mass system, calculated in this manner for N_2^+ scattering from gold and graphite at various energies, are given in Fig. 5. As can be seen, the relative energy spectra

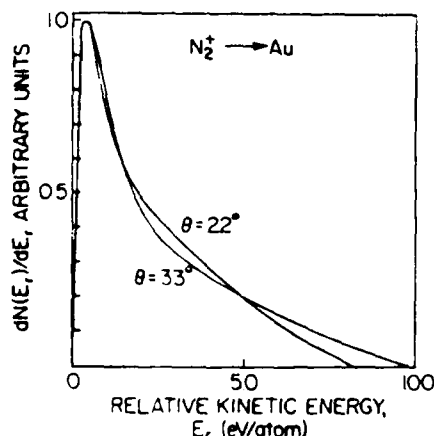


FIG. 6. Relative kinetic energy distributions of nitrogen atomic N^+ ions resulting from 2.5 keV N_2^+ scattering from gold at $\theta = 22^\circ$ and 33° .

all peak at low energy < 1 eV and extend out to higher energies ranging from ~ 10 eV for 1.5 keV scattering to greater than 20 eV for 4.5 keV scattering. Comparison of the graphite and gold results also shows that the relative energy distribution for scattering from graphite is slightly broader with the tail of the distribution extending to higher energies, indicating a slightly higher degree of excitation for N_2^+ scattering from C atoms. Changing the scattering angle from 22° to 33° for N_2^+ scattering from gold causes little change in the center of mass energy distribution as shown in Fig. 6.

B. TOF spectra.

Heiland *et al.* have shown¹² that neutralization plays an important role in the composition of the scattered flux. In order to examine the degree of neutralization, the TOF spectra of both the ions and neutrals were measured. A typical TOF spectrum is shown in Fig. 7 for 2 keV N_2^+ scattering from gold at 22° . The TOF of N_2 and N are nearly identical and are not resolved. No distinction between a sharp N_2 peak superimposed on a broad N peak is observed, in contrast to the work of Heiland.¹² This is probably due to the low N_2 survival probability at the higher scattering energies and angles used in our experiments. The low intensity peak at short flight times is due to directly recoiled nitrogen which has been deposited on the surface from the impinging beam. Measurement of the ion fraction in the scattered flux was performed by comparison to the neutral only spectra obtained by postscattering deflection of the scattered ions. The neutral only spectra were indistinguishable from the ion plus neutral spectra for all scattering energies and angles employed, indicating that the ion fraction was less than 1% of the total scattered flux.

IV. DISCUSSION

Previous theoretical models of the dissociation of fast diatomic ions upon reflection from surfaces have treated the dissociation process as purely classical.^{13,16} The Parillis model¹⁵ assumes correlated collisions of the individual atoms with the surface. This treatment allows the derivation

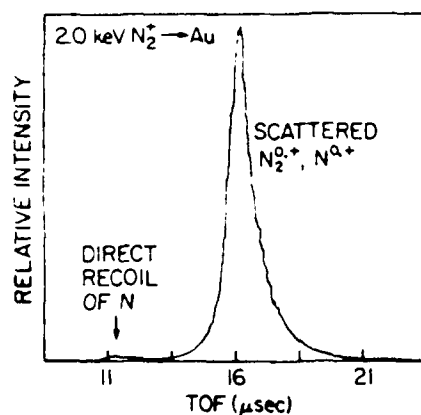


FIG. 7. TOF neutral plus ion spectrum obtained for 2.0 keV N_2^+ scattering from gold at 22° . The neutral only spectrum was indistinguishable from the neutral plus ion spectrum due to the small ion fraction. The small peak near 11 μ s represents directly recoiled nitrogen atoms from the surface.

of expressions which are directly comparable to the experimental data. The model attributes the broadening of the N^+ peak to self-scattering of the atoms in the molecular ion and predicts that the relative energy widths of the N_2^+ to N^+ peaks should be $1:\sqrt{2}$. This agrees satisfactorily with the results of scattering from the graphite surface where the ratio is approximately 1:1.3, but agreement is poor for scattering from gold where the ratio is 1:3.7. The model also predicts that the ratio of scattered molecular species to scattered atomic species (R_m/R_a) resulting from dissociation should follow the expression

$$R_m/R_a = (\epsilon/d^2 E_0) R(\theta), \quad (4)$$

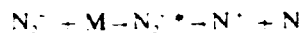
where ϵ is the bond energy of the molecular ion, d is the bond length of the ion, and E_0 is the primary ion energy. $R(\theta)$ is the scattering intensity one would observe if the corresponding atomic ion was scattered from the same surface with a primary ion energy of $E_0/2$ and scattering angle θ . Therefore, $R(\theta)$ should be proportional to the scattering cross section (σ) of N^+ . The ratio of surviving molecular ions to dissociated atomic ions then becomes $R_m/R_a \propto \sigma/E_0$. We have calculated the scattering cross sections with a scattering program²¹ that uses the Moliere approximation²² to the interaction potential for nitrogen atomic ions scattering from gold and graphite surfaces at scattering angles of 22° and 33° . Plots of the ratio of molecular to atomic ion scattering intensity R_m/R_a vs σ/E_0 are linear as the model predicts. However, this may be an artifact since we are only applying it to scattered ions, while the Parillis model treats the total scattered flux. The measured ion fraction of the scattered flux is less than 1%. Therefore, in order to assume that our data fits the Parillis model, we must assume that the relative ion fractions of N and N_2 are constant over the E_0 range studied. This is unlikely as the neutralization probabilities of the atomic and molecular ions are probably different and energy dependent. Therefore, a rigorous test of the Parillis model cannot be made without information on the composition of the constituents in the scattered neutral flux.

The relative energy distributions of the scattered N^+ following dissociation extend to 10–20 eV/atom with average values in the 2–3.5 eV/atom range. This indicates that on average the N_2^+ molecular ion is excited 4–7 eV above the dissociation limit. This level of excitation cannot be explained by simple mechanical (rotational or vibrational) dissociation mechanisms. For this level of excitation, excited electronic states must play an important role in the dissociation process.

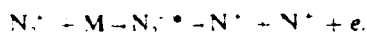
The charge exchange and excitation processes in molecular ion-surface collisions can be treated in the same manner as atomic ion-surface collisions. Ions impinging on a surface can undergo charge exchange into the ground or excited states along the incoming or outgoing trajectory²⁷ by resonant or Auger processes. Therefore, the incoming N_2^+ ion can undergo resonant or Auger neutralization on the incoming trajectory. As described by Heiland,^{6,7,12} charge transfer into a dissociative state of N_2 can cause dissociation and neutral N scattering while charge transfer into bound states can result in associative neutral scattering. The scattered molecular ions and atomic ions observed in this work must

therefore arise from those ions which survive the incoming and outgoing trajectories in their initial charge state or those neutralized molecules which are reionized in the close encounter. The latter process has a low probability at the low energies employed.¹⁷

In addition to charge exchange on the incoming and outgoing trajectories, the incoming ion can also experience additional neutralization and electronic excitation during the close encounter with a surface atom.^{28,29} These processes can be described by the Fano-Lichten mechanism.^{30,31} In the violent collision of the incident ion with a surface atom, significant overlap of the atomic orbitals (AOs) of the surface atoms and the AOs or molecular orbitals (MOs) of the projectiles can occur. Electron promotion can then occur within the MOs of the projectile/target complex formed during the collision. Applying this mechanism to molecular ion surface collisions, those molecular ions which survive the incoming trajectory in their original charge state collide with a surface atom. During this close encounter, significant overlap of the target AOs and N_2^+ MOs can occur resulting in electron promotion, ionization, and neutralization. Excitation of the molecular ion to dissociative states results in scattering of atomic ions and neutrals according to the processes



or



Previous studies of N_2^+ scattering from noble gas atoms gives a good indication of the specific processes involved in N_2^+ dissociation on surfaces. Fourrier *et al.* have observed predissociation of the vibrationally excited $C^2\Sigma_u^+$ state in $N_2^+ \rightarrow He$ collisions resulting in energy released in the 0.03–1.44 eV range.²⁴ Also, examination of the N_2^+ energy level diagram³² in Fig. 8 shows that impact induced excitation of ground state $X^2\Sigma_g^+$ N_2^+ to the $D^2\Pi_g$ state in the Frank-Condon region results in energies 0–9 eV in excess of the dissociation limit. These two transitions, in particular, fit in well with the observed relative E_k distributions. As the primary ion E_k is increased, excitation to higher MOs of N_2^+ become possible resulting in an increase in the higher energy portion of the relative E_k distribution. Other possible processes resulting in scattered N^+ are ionization of neutralized N_2 in the close encounter to a dissociative state of N_2^+ or resonant or Auger transfer from neutral N to the surface on the outgoing trajectory. The former process can be described in identical terms as N_2^+ excitation in the close encounter. Therefore, we propose that the primary dissociation mechanism of the molecular nitrogen ion upon collisions with gold and graphite surfaces to yield scattered atomic ions is excitation of the molecular ion to dissociative states in the close encounter.

Within the context of the proposed mechanism, the trends observed in these experiments can be described. As the primary ion energy increases, there is greater orbital overlap, resulting in greater excitation to dissociative states, lowering the N_2^+ yield, and shifting the relative E_k distributions to higher energies. These results are analogous to the

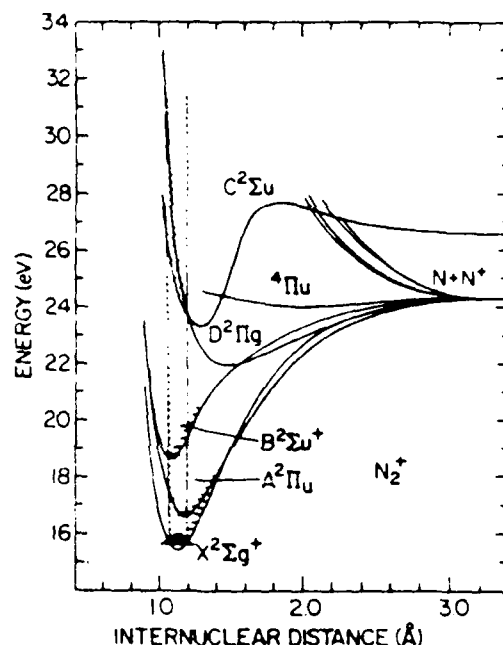


FIG. 8 Energy level diagram for N_2^+ adapted from Ref. 30. The ordinate represents the potential energy of an electron bound to N_2^+ . The zero of energy is the zero-point energy of ground state $X^2\Sigma_g^+$ neutral N_2 . The Frank-Condon region illustrates a transition leading to dissociation into $N(^4S^+)$ + $N(^4P)$.

ion fraction studies of scattered noble gas ions.¹⁷ The ion fractions of the scattered noble gas ions increase with increasing energy due to the greater degree of orbital overlap and resulting electronic excitation. The shift of the relative E_k distribution to higher energies for scattering from graphite as opposed to gold is in agreement with the arguments of Barat and Lichten³⁰ in that electronic excitation cross sections are highest between collision partners of similar atomic number. Therefore, nitrogen molecular ions would experience a higher degree of excitation upon collision with C atoms than with Au atoms, resulting in a shifting of the relative E_k distribution to higher energies.

V. CONCLUSIONS

N_2^+ scattering from graphite and gold surfaces in the energy range 1.5–4.5 keV results primarily in dissociation with only a small fraction of surviving molecular ions. This surviving molecular ion fraction varies from 0.08 to 0.002, increasing with decreasing primary ion energy and scattering angle. The relative E_k distributions of the scattered N^+ indicates that the dissociation mechanism involves electronic excitation of the N_2^+ to dissociative excited states. For dissociation yielding atomic ions, the data are consistent with a mechanism in which electronic excitation occurs in the close encounter as described by the Fano-Lichten mechanism.

ACKNOWLEDGMENT

This material is based on work supported by the Air Force Research Office under Contract No. F19628-86-K-0013.

- ¹W. Eckstein, in *Inelastic Particle Surface Collisions*, edited by E. Taglauer and W. Heiland (Springer, Berlin, 1981).
- ²W. Eckstein, H. Verbeek, and S. Datz, *Appl. Phys. Lett.* **27**, 527 (1975).
- ³P. Massmann, H. Hopman, and J. Los, *Nucl. Instrum. Meth.* **165**, 531 (1979).
- ⁴H. Verbeek, W. Eckstein, and R. S. Bhattacharya, *Surf. Sci.* **95**, 380 (1980).
- ⁵P. J. Schneider, W. Eckstein, and H. Verbeek, *Nucl. Instrum. Meth.* **194**, 387 (1982).
- ⁶W. Heiland, U. Bentat, and E. Taglauer, *Phys. Rev. B* **19**, 1677 (1975).
- ⁷W. Heiland and E. Taglauer, *Nucl. Instrum. Meth.* **194**, 667 (1982).
- ⁸L. L. Balashova, Sh. N. Garin, A. I. Dodonov, E. S. Mashkova, and V. A. Molchanov, *Surf. Sci.* **119**, L378 (1982).
- ⁹L. L. Balashova, A. Dodonov, Sh. N. Garin, E. S. Mashkova, and V. A. Molchanov, *J. Phys. B* **16**, 2609 (1983).
- ¹⁰B. Willerding, W. Heiland, and K. Snowdon, *Phys. Rev. Lett.* **53**, 2031 (1984).
- ¹¹A. I. Dodonov, Sh. N. Garin, E. S. Mashkova, and V. A. Molchanov, *Surf. Sci.* **140**, L244 (1984).
- ¹²B. Willerding, K. J. Snowdon, U. Imke, and W. Heiland, *Nucl. Instrum. Meth. B* **13**, 614 (1986).
- ¹³I. S. Bitenski, and E. S. Parillis, *Proc. of the Symp. on Sputtering*, Vienna, edited by P. Varga, G. Betz, and F. Viehbrock, 1980, p. 688.
- ¹⁴I. S. Bitenski, and E. S. Parillis, *Sov. Phys. Tech. Phys.* **26**, 1042 (1981).
- ¹⁵I. S. Bitenski, and E. S. Parillis, *Nucl. Instrum. Meth. B* **2**, 364 (1984).
- ¹⁶M. M. Jakas and D. E. Harrison, *Surf. Sci.* **145**, 500 (1985).
- ¹⁷J. W. Rabalais, J. N. Chen, R. Kumar, and M. Narayana, *J. Chem. Phys.* **83**, 6489 (1985).
- ¹⁸J. W. Rabalais, J. A. Schultz, R. Kumar, and P. T. Murray, *J. Chem. Phys.* **78**, 5250 (1983).
- ¹⁹D. P. Smith, *J. Appl. Phys.* **38**, 340 (1967).
- ²⁰Y. J. Jo, J. A. Schultz, T. R. Schuler, and J. W. Rabalais, *J. Chem. Phys.* **89**, 2113 (1985).
- ²¹R. Kumar, M. H. Mintz, and J. W. Rabalais, *Surf. Sci.* **147**, 15 (1984).
- ²²I. M. Torrens, *Interatomic Potentials* (Academic, New York, 1972).
- ²³K. H. Purser, R. H. Rose, N. B. Brooks, R. P. Bastide, and A. B. Wittkower, *Phys. Lett.* **4**, 176 (1963).
- ²⁴P. Fournier, C. A. Van de Runstraat, T. R. Govers, F. J. Heer, J. Schopman, and J. Los, *Chem. Phys. Lett.* **9**, 426 (1971).
- ²⁵T. F. Moran, F. C. Petty, and A. F. Hedric, *J. Chem. Phys.* **51**, 2012 (1969).
- ²⁶D. K. Gibson and J. Los, *Physica* **35**, 258 (1967).
- ²⁷H. D. Hagstrum, *Electron Spectroscopy of Solids*, edited by L. Tiersmans, J. Vennik, and W. Dekeyser (Plenum, New York, 1978).
- ²⁸A. L. Boers, *Nucl. Instrum. Meth. B* **4**, 98 (1984).
- ²⁹L. K. Verhey, B. Poelsema, and A. L. Boers, *Nucl. Instrum. Meth.* **132**, 365 (1976).
- ³⁰U. Fano and W. Lichten, *Phys. Rev. Lett.* **14**, 627 (1965).
- ³¹M. Barat and W. Lichten, *Phys. Rev. A* **6**, 211 (1972).
- ³²F. R. Gilmore, *J. Quant. Spectrosc. Radiat. Transfer* **5**, 369 (1967).